

A Study for Improvement of Combustion and Exhaust Emissions of a Diesel Engine

Jo Hyun

Contents

Chapter 1. Background	1
1.1 Current global situation and policies for diesel engines	1
1.2 Combustion analysis and visualization for improvement of diesel combustion	3
1.3 Aftertreatment system for reducing the harmful emission of diesel engine.....	9
1.3.1 Diesel oxidation catalyst (DOC) and diesel particle filter (DPF)	9
1.3.2 Selective catalytic reduction (SCR)	10
1.4 Objective of this study.....	13
1.5 Thesis framework	14
Chapter 2. The Analyzing the Structure of the Diesel Spray Flame by Time-resolved PIV with Chemiluminescence of OH*	23
2.1 Introduction	23
2.2 Experimental setup	24
2.2.1 Experimental apparatus	24
2.2.2 Imaging technique	27
2.3 Results and discussions	29
2.3.1 Relationship between the high-temperature region and velocity distribution in diesel spray flame	29
2.3.2 Effect of injection pressure on velocity distribution and velocity fluctuation intensity in diesel spray flame	36
2.3 Summary	40
Chapter 3. Characteristics of the Diesel Spray Flame in Various Condition with Different Jet-Jet Angle	44
3.1 Introduction	44
3.2 Experimental setup	45
3.2.1 Experimental apparatus	45
3.2.2 Imaging technique for OH* chemiluminescence and direct imaging	48
3.2.3 Experimental setup for PIV	50
3.3 Results and discussions	55
3.3.1 Effect of jet-jet angle	55
3.3.2 Effect of injection conditions in different jet-jet angle	58
3.3.3 Effect of oxygen concentration in different jet-jet angle	64

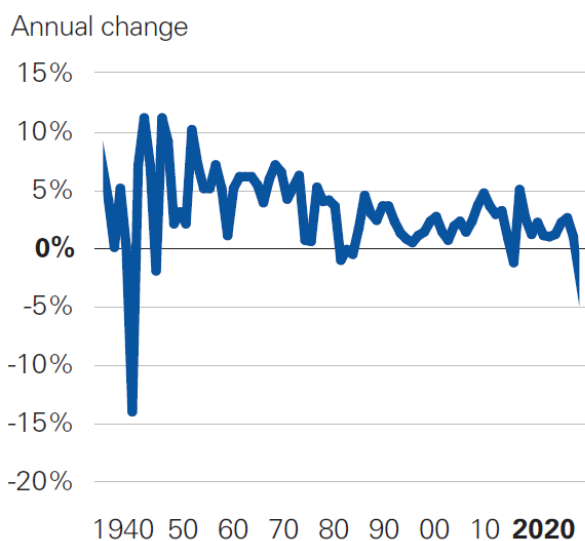
3.3.4 Analysis of the velocity between sprays according to the jet-jet angle through the PIV method	66
3.4 Summary	82
Chapter 4. Analysis of the Relationship between Near-wall Velocity Distribution and Wall Heat Flux by a Diesel Spray Flame Impingement	86
4.1. Introduction	86
4.2 Experimental setup	87
4.2.1 Experimental apparatus	87
4.2.2 Imaging condition	89
4.3 Results and discussion	91
4.3.1 Analysis of the velocity distribution and heat flux on the combustion chamber wall in non-combustion situation	91
4.3.2 Analysis of the velocity distribution and heat flux on the combustion chamber wall in combustion situation	97
4.4 Summary	100
Chapter 5. Optimizing Urea-Water-Solution Injection Strategy for High Conversion Ratio in After-treatment System	102
5.1 Introduction	102
5.2 Experimental setup	103
5.2.1 Experimental apparatus	103
5.2.2 Experimental procedure and analysis	105
5.3 Results and discussion	108
5.3.1 Analysis of NH ₃ adsorption in SCR in different engine condition	108
5.3.2 NH ₃ adsorption and desorption rate in SCR at different engine condition	114
5.4 Summary	117
Chapter 6. Conclusion	120
6.1 Conclusion	120
6.2 Recommendations for the researches	123
List of publication	125

Chapter 1. Introduction

Chapter 1.1 Current global situation and position of the diesel engines

After industrialization, a great technological development was made and an energy consumption began to rapidly increase. In this trend, the internal combustion engines have been used in a various field such as transportation and power generation. However, it has been recognized that it causes a problem such as depletion of a fossil fuel, the climate change by greenhouse gases, and an air pollution by harmful substances in globally. In order to respond this situation, an international effort such as the United Nations Framework Convention on Climate Change (UNFCCC), the Kyoto Protocol, and the Paris Agreement are continuously being made. Since the Paris Conference of Parties (COP21) in 2015, there has been an active global movement towards decarbonization. Through this, about 70% of global carbon emissions are being processed through the net-zero targets and pledges. In addition to these global movements, due to the impact of COVID-19, the global energy consumption has shown a trend that has continued to rise until now and then momentarily decreased as Figure 1.1 [1]. In particular, compared to the other resources, oil showed a decrease of about 3 times or more in the existing demand forecast as Figure 1.2. However, this is only the temporary specificity of COVID-19, and efforts to improve the thermal efficiency of internal combustion engines and reduce the emission must be continued in the future.

Primary energy consumption



CO₂ emissions from energy use

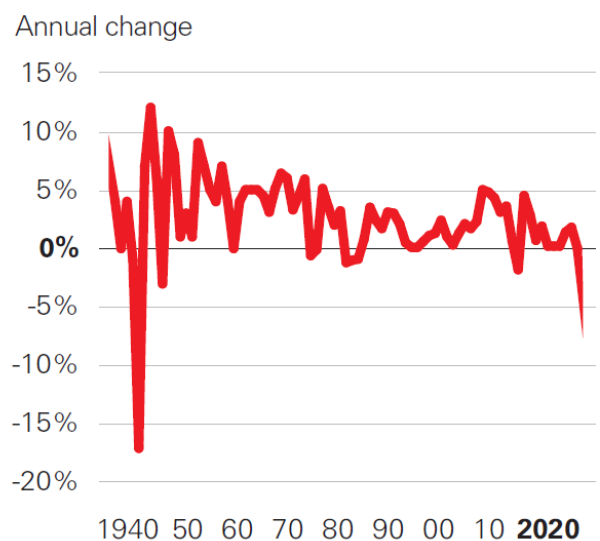


Figure 1.1. Global energy demand and carbon emissions [1]

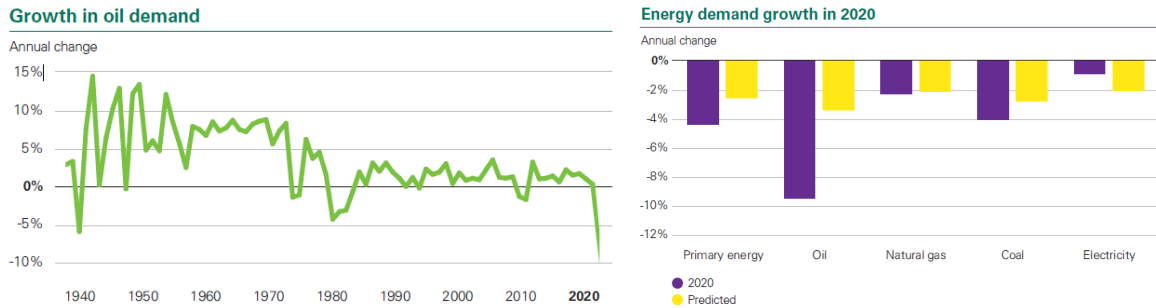


Figure 1.2. Global growth in oil demand and energy demand growth in 2020 [1]

In accordance with the recent trend toward an electrification of automobiles, the battery electric vehicle is increasing. However, the market share of the pure internal combustion engine vehicle and the hybrid vehicle equipped with an internal combustion engine is still higher than the pure electric vehicle. In addition, the life cycle assessment (LCA) method, which evaluates not only the carbon dioxide generated from the driving conditions of the automobile, but also the entire automobile production and disposal process, is being applied. When the LCA method is applied, the total CO₂ emission is judged to be similar to that of the internal combustion engine vehicle and the electric vehicle because of all processes from production to disposal are evaluated as Figure 1.3 [2]. For this reason, the studies are being conducted to improve the sustainability of the internal combustion engine as an eco-friendly power device. The most necessary for the purpose is to increase the efficiency of engine and reduce the emission of harmful exhaust gases.

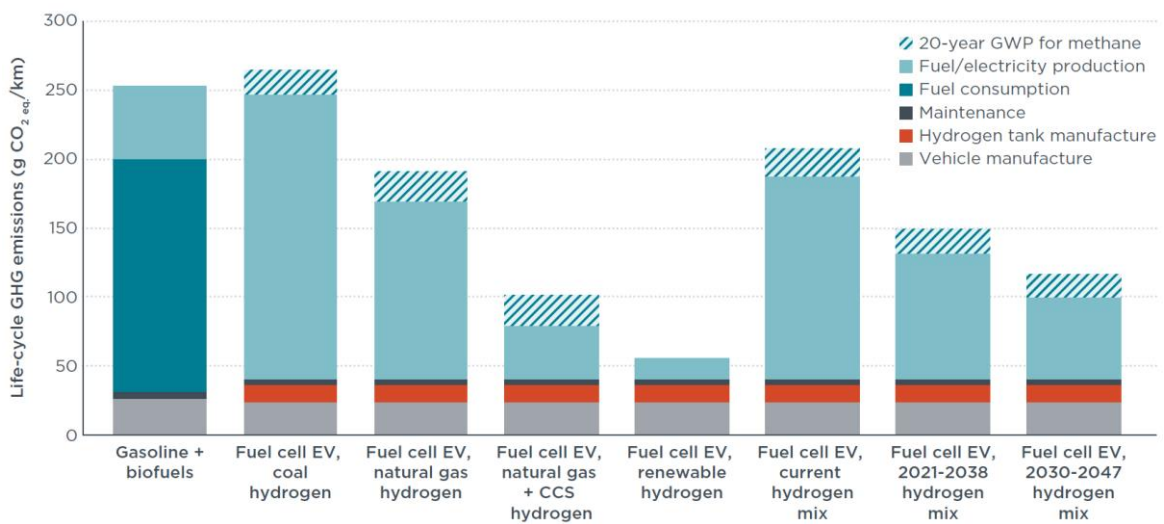


Figure 1.3. Life-cycle GHG emissions of global typical medium-size FCEVs powered by coal-, natural gas, CCS natural gas-, or renewable electricity-based hydrogen, by the current mix of these pathways and by the expected lifetime average mix for cars registered in Europe, the U.S., China, and India in 2021 and in 2030, compared to global typical gasoline cars registered in 2021 [2]

Diesel engine plays an important role in the transportation sector, such as the light-duty (LD) and heavy-duty (HD) vehicle. However, in order to solve the environmental problems which before mentioned, the regulations on emission are becoming stricter. European emission regulation is a representative emission regulation of the diesel engine. In the case of the Euro 7, which was recently announced, only very small amounts of the emission are allowed due to very strict regulation. Although many researches have been conducted to reduce the emission from the combustion process of a diesel engines. However, since the emission and a thermal efficiency of a diesel engine have a trade-off relationship, so the research on ways to increase the thermal efficiency of a diesel engine should be conducted. In order to increase a thermal efficiency through combustion control of a diesel engine, it is necessary to reduce the exhaust loss and cooling loss. To reduce the exhaust loss, it is necessary to improve the degree of constant volume (DCV) by shortening the combustion duration and to increase the compression ratio [3-5]. In order to shortening the combustion duration, it is necessary to shortening the injection duration, and for this purpose, a strategy of increasing the injection pressure and increasing the number of multi-holes injector is being implemented. To reduce the cooling loss, it is necessary to prevent a heat escaping from the combustion chamber to engine block. For this, it is necessary to increase the thermal insulation of the combustion chamber wall surface or reduce the area where the diesel spray impinge to the combustion chamber wall and the velocity near the combustion chamber wall [6-12].

Chapter 1.2 Combustion analysis and visualization for improvement of diesel combustion

In order to increase the thermal efficiency of a diesel engine, a method for improving the DCV to reduce the exhaust loss or reducing the cooling loss generated from the combustion process is being discussed. In order to improve the DCV, the combustion duration must be shortened. For this, it is necessary to know the mechanisms of a diesel spray flame that occur during the mixing-controlled combustion. Therefore, in order to shorten the combustion duration, it is considered effective to increase the local heat release rate in the stoichiometric region where the fuel and air are mixed in a diesel spray flame and cause the main chemical reaction. In order to increase the local heat release rate in the stoichiometric region, it is important to increase the turbulence so that air and fuel can be mixed well. Therefore, it is necessary to clarify the heat release mechanism through the turbulence intensity and the temperature distribution inside the diesel spray flame.

As mentioned earlier, the structure of a diesel spray flame is helpful to understand the diesel combustion process. Therefore, a study on the effect of the ambient combustion chamber condition on a diesel spray flame was necessary. Experimental and numerical studies of the droplet distribution inside a diesel spray flame were conducted using lasers to understand the structure of diesel spray flame [13]. In addition, the effect of

ambient gas density and fuel vaporization on diesel spray penetration and dispersion was investigated [14]. As the ambient gas density increases, the diesel spray dispersion increases, allowing more air to be injected into the diesel spray. And the total mass of the area entrained by the conservation of momentum becomes large, which slow down the penetration velocity and causes a decrease in the penetration length of the diesel spray. The ignition delay of a diesel combustion was shortened as the ambient density increased [15]. The high heat capacity at the spray boundary due to the high ambient density mitigates the temperature drop in the ambient gas and promotes premixture. When the injection pressure increases and the swirl-flow inside the combustion chamber decreases, the spray tip penetration is increased and mixture formation is promoted in the area of the spray tip near the combustion chamber wall. Therefore, when the fuel injection pressure increases, the ignition delay is shortened because the mixture formation is promoted and a large amount of the combustible mixture is formed. A constant volume combustion chamber was used to study how the velocity distribution inside a diesel spray depends on the ambient gas density and injection pressure [16]. Regardless of the injection pressure, the spray width increased with increasing ambient gas density, and the position of the maximum velocity gradient shifted from the periphery to the center of spray as the ambient gas density increased. When the equivalence ratio was estimated from the velocity distribution inside the diesel spray, a sufficient air was not entrained into the spray in the condition of a low ambient density. However, at a high ambient density, a large amount of air is entrained into the spray and a sufficient mixture of the fuel and air for combustion is also formed upstream of the spray. The result of studying the velocity distribution and turbulence characteristic of a non-evaporative diesel spray using the particle image velocimetry (PIV) are presented [17]. The modeling of a wide range of diesel spray combustion conditions was conducted using the Eulerian-based probability density function (PDF) method and verified experimentally [18, 19]. The above method was also used to study an ignition behavior and flame structure according to the ambient pressure under the same conditions as a diesel engine. In addition, the ambient temperature sweep phenomenon under non-combustion and combustion situation of a diesel spray was modeled through the large eddy simulation (LES) [20].

As described above, it can be seen that the ambient condition has a great influence on the formation of a diesel spray flame structure. However, since the diesel engine uses an injector to directly inject a fuel into the combustion chamber, the diesel spray flame structure may vary due to a fuel injection condition in addition to an ambient condition inside the combustion chamber. For this purpose, a study has been conducted on how the diesel spray flame structure is affected when the fuel injection condition is changed. A study was conducted to analyze the combustion characteristics that occur when the fuel injection amount is the same and the injection pressure is high [21]. In the case of non-evaporative spray, as the injection pressure increased, the sauter-mean-diameter (SMD) decreased and the air entrainment velocity increased. When the injection pressure increased, the soot concentration in the flame decreased and also the combustion duration has been shortened. When the injection pressure is high, the behavior of non-evaporative diesel spray was compared with an experimental data and modeling results [22]. From this, it

can be seen that the spray tip penetration and cone angle are significantly affected by the ambient gas density.

Through a various result from the research, it was found that the injection conditions and ambient conditions affect the formation of a diesel spray flame structure. Based on these results, it can be seen that the mixture fraction of the fuel and air varies depending on the turbulent flow characteristic of the diesel spray depending on the fuel injection condition or the ambient condition of the combustion chamber, which affects the combustion process. Therefore, a study was conducted on how the turbulent flow characteristics inside the diesel spray appear under various conditions. The diesel spray mixes well with an air in high turbulence intensity region and, as the injection pressure increases, the occurrence frequency of large eddy increases. This increases the strength of turbulence and the spray tip penetration, which improves the mixing of the fuel and air. The planar laser-induced fluorescence (PLIF) was used to analyze the instantaneous fuel concentration distribution of a non-evaporative diesel spray under high-temperature conditions [23]. Although the injection pressure had no significant effect on the fuel concentration, a smaller nozzle orifice resulted in a lower mixing concentration. When the injection pressure is high and the nozzle orifice diameter is small, a mixing formation in the spray is promoted immediately after the start of injection, and the mixture is rapidly diluted after the injection is ended. To understand the relationship between a local fuel-air mixing process and a subsequent heat release of diesel spray, a react spray study was conducted with a one-dimensional Eulerian spray model validated under inert conditions [24, 25]. This model is suitable for free gas jets or single-hole injector sprays where there is no interaction with the wall or no surrounding gas flow. The modeling was verified through the CFD calculation of gas jet and experiment with diesel spray. As an effect on flame development, it was shown that heat release inside the spray increases the local temperature and decreases the density. Also, by increasing the spray radius width, the local density of the react spray decreased compared to that of the non-react spray. A study was conducted on the mechanism of the liquid fuel spray and a turbulent flow in combustion situation through the LES [26, 27]. The velocity distribution inside the non-combustion diesel spray of the high injection pressure was analyzed by applying the PIV method [28]. The local droplet concentration was significantly lower in the center of the vortex motion, and the tendency of droplets to accumulate in the region with a low vorticity was observed.

In order to improve the thermal efficiency, a study has been conducted on the structure and the velocity distribution of the diesel spray flame. In addition, study was also conducted to suppress the soot formation by analyzing the soot formation process through the structure of the diesel spray flame. For this purpose, research using a various method to visualize the soot formation in the diesel spray flame was conducted. The diesel combustion process was investigated using a various laser diagnostic, empirical measurement, and chemical kinetic code [29-31]. From the laser induced incandescence (LII) image, it can be seen that the soot concentration decreases as the injection pressure increases. Also, it appears that the shape of the vapor region of diesel spray in the non-combustion condition is very similar to the shape of soot distribution in the combustion condition. This suggests that the soot formed in the region where the fuel is vaporized and the soot distribution expands and this phenomenon was imaged as shown in Figure 1.4.

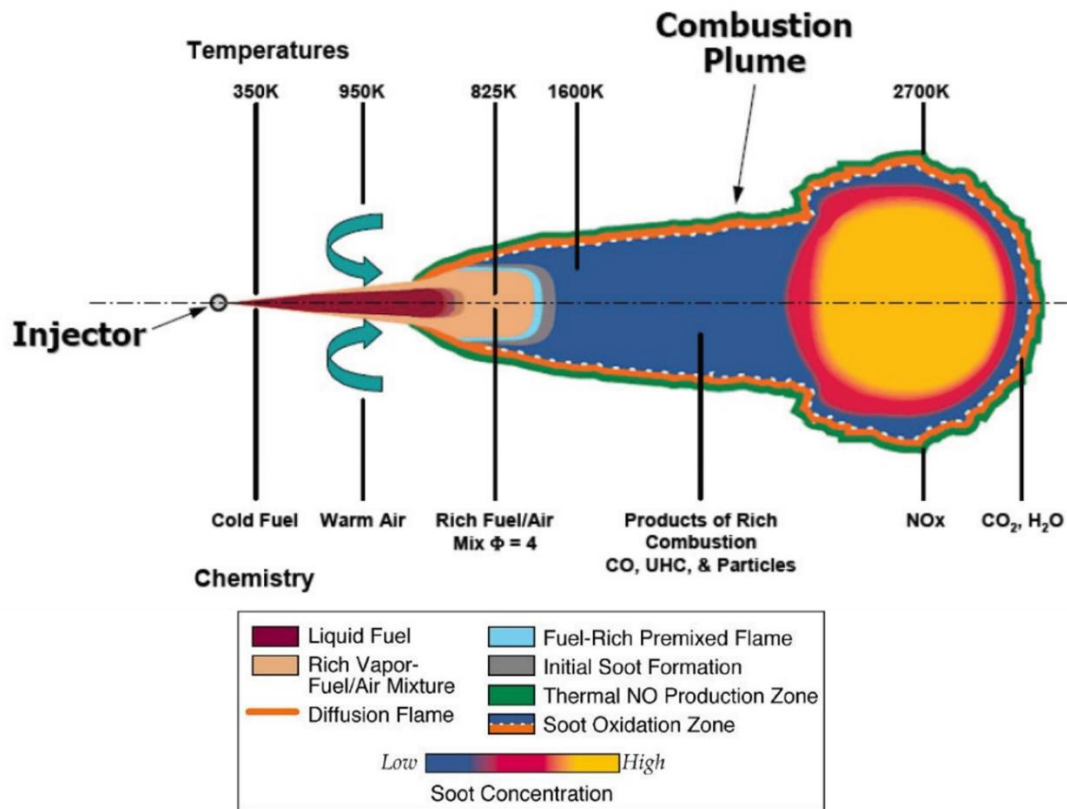


Figure 1.4 A schematic of the conceptual model with additional features (fuel-rich premixed flame, soot formation, soot oxidation and NO_x formation zones) [29-31]

Also, in the initial soot formation stage after ignition started, the soot precursor was mainly located in the central region of diesel spray flame, and it can be seen that soot particles surround the soot precursor and expand downstream as Figure 1.5 [32]. When the soot precursor was analyzed through the intensity of the LIF, it was maximized immediately after combustion in the rich vapor of the fuel and air mixture region. And, when the soot particle was analyzed through the intensity of the LII, it gradually increased and reached a maximum after the injection was finished. The OH radical and the soot from the diesel spray flame were visualized through the LIF and laser induced scattering (LIS) [33]. The OH radicals appear before the soot formed in the diesel spray flame region. In the downstream of the diesel spray flame in quasi-steady period, the soot mainly exists in the central region, and the OH radicals exist in the peripheral region. A study was conducted to visualize the maximum axial distance of liquid fuel, which called the liquid length, during the diesel spray injection using the Mie scattering method [34].

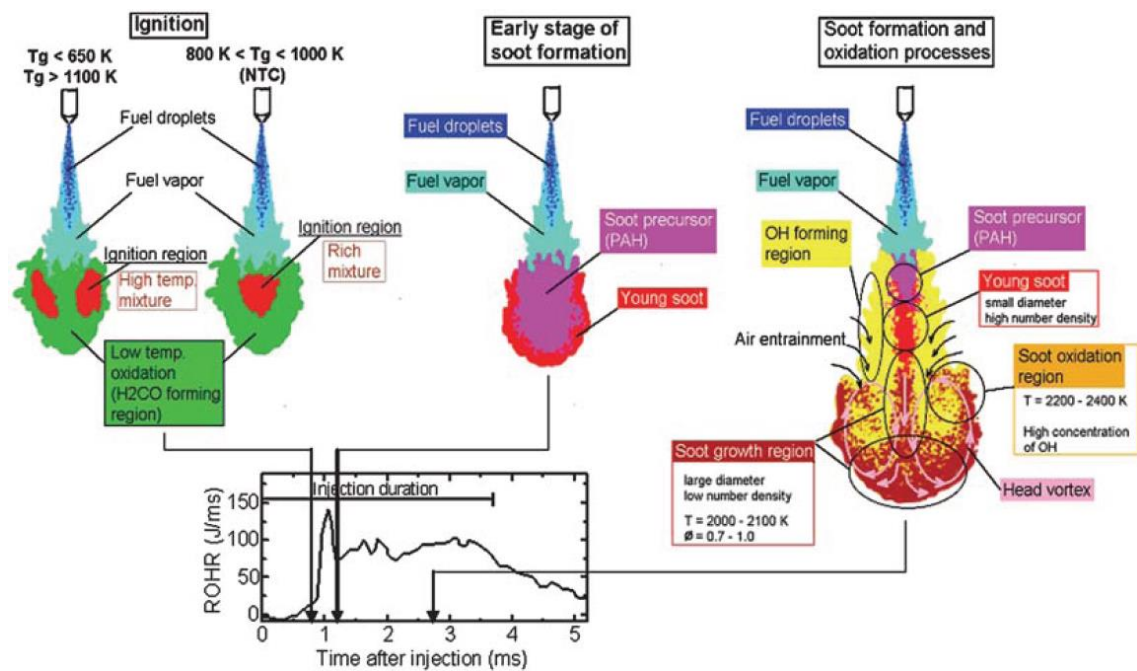


Figure 1.5 Conceptual model of ignition, soot formation, and oxidation process in a diesel spray flame

[32]

The lift-off length and liquid length, which are used as the basis for analyzing the characteristics of the soot formation in diesel spray flame, showed that it varied depending on the specification of the injector, the injection condition, and the ambient condition in combustion chamber. Therefore, studies have been conducted to investigate the structure of diesel spray flames by analyzing the lift-off length and liquid length under various condition. The liquid length showed a linear dependence on the orifice diameter, and the liquid length decreased with the increasing ambient gas density and temperature. For the diesel spray generated by the high-pressure solenoid injection system, a database was presented by experimenting under a various condition such as ambient temperature, density, and the injection pressure using a chamber which has a high-temperature, high-pressure in constant volume [35]. When a diesel spray flame appears and stabilizes at the downstream of the diesel spray, the distance between the injector tip and a firstly measuring position of the high-temperature region is called the lift-off length [36]. How the lift-off length appears according to the temperature and density of ambient gas, the injection pressure, and the orifice diameter of injector was analyzed. Through these results, the how the lift-off length affected by the fuel and air mixing, the soot formation, and the fuel vaporization and combustion on diesel sprat flame was studied. As the ambient temperature and density increase and the orifice diameter decreases, the lift-off length decreases, and as the injection pressure increases, the lift-off length increases. As the lift-off length increases, the ratio of stoichiometric air entrained into the spray increases, which can lead a decreasing of soot formation due to increase the amount of entrained air. In addition, a study on the lift-off length according to change in the oxygen concentration of ambient gas was also conducted [37]. The lift-off length is inversely proportional

to the oxygen concentration of ambient gas. As the ambient oxygen concentration decreased, the lift-off length showed an increase compared to the liquid length. As the oxygen concentration decreases, the lift-off length increases and the oxygen entrainment rate per unit length of the fuel jet decreases. It was determined that the diesel spray increased the time required to complete the combustion process. And, as the fuel with a shorter ignition delay was used, the lift-off length became shorter [38]. A study was conducted on the effect of ignition delay on lift-off length and soot formation under various fuel condition [39-42]. When using a low cetane number fuel, the lift-off length increased. Also, it was suggested that the fuel effect was the difference in the amount of mixing with hot air required for auto ignition. Through this, it can be judged that the soot formation is suppressed, but a further stud for improvement of the engine performance and reduction of the NO_x emission are needed. The effect of interaction between the diesel spray and wall on the lift-off length was studied [43]. Due to the phenomenon of entrainment after the diesel spray impinges to the wall, the lift-off length is shortened and the soot formation is increased. To improve this, it is necessary to design a combustion chamber with a larger bowl diameter and a split injection strategy of fuel. By controlling the fuel injection rate in reverse-delta shape, a more uniform combustion area distribution and thermal efficiency of the diesel engine were improved, and studies on the liquid length, lift-off length and soot formation were conducted [44, 45].

Although the studies mentioned above have clarified the structural characteristics of a diesel spray flame, most have been experimented in a free spray of single-hole injectors. However, the injector used in an actual diesel engine is a multi-hole injector, and the influence of the adjacent sprays is additionally existed [46]. Therefore, it is necessary to study the structure of diesel spray flame based on the effects that may appear during fuel injection in a multi-hole injector situation. When the jet-jet angle was 45 degrees, the lift-off length was shortened from the start of combustion until the end of injection. As the jet-jet angle decreased, the hot burned gas generated from the adjacent spray was entrained into the lift-off region, showing that the lift-off length has shortened. According to the single-hole injector and the multi-hole injector, a study was conducted to analyze how the air flow around the diesel spray up to the lift-off length appears through the particle tracking velocimetry (PTV) method [47]. As the injection pressure increased, the entrained velocity around the lift-off region increased, and the entrained velocity in the multi-hole injector was larger than that in the single-hole injector over the entire lift-off region. In addition, the lift-off length increased as the injection pressure increased, and the amount of air entrained into the diesel spray increased due to the increase in the entrained area and velocity. In the combustion situation on the actual diesel engine, the lift-off length of multi-hole injector can be seen to greatly affect the backward flow of the hot burned gas surrounding the diesel spray flame [48]. In the case of a single free spray, the backward velocity was negligibly small, but in the presence of a spray adjacent to the combustion chamber wall, the magnitude of the backward velocity becomes non-negligible. The lift-off length of the spray with the adjacent wall was shorter than that of a single free spray due to the backward flow of the hot burned gas. This difference is larger because a larger nozzle diameter increases the fuel injection rate and leads to a higher backward

velocity. In addition to this difference, a backward flow increased because of a larger nozzle diameter increased the fuel injection rate.

Considering the above studies, an injector with a large jet-jet angle should be used to suppress the soot formation. However, in order to increase the aforementioned DCV, the combustion duration must be shortened, and for this purpose, the same amount of fuel must be injected in a short time. Since there is a technical limit to setting a very high injection pressure, an increase in the number of injector holes cannot be avoided. Therefore, it is necessary to improve the relationship between soot and thermal efficiency by clarifying the phenomenon in which the soot formation is formed in multi-hole injectors.

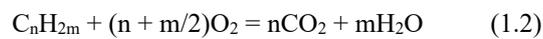
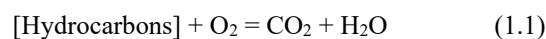
Chapter 1.3 After-treatment system for reducing the harmful emission of diesel engine

For the sustainable use of internal combustion engines, as mentioned above, studies have been conducted to improve the thermal efficiency of diesel engines. Another problem to be improved in internal combustion engines is also related to harmful emissions. Internal combustion engines have been at a disadvantage in the recent environmental challenges facing them. In particular, NO_x and particle matter (PM) are the most emphasized harmful emissions from diesel engines. For this reason, restrict regulations are enforced around the world for harmful emissions from internal combustion engines [49-53]. In order to satisfy these regulations, many studies have been conducted to reduce harmful emissions in the combustion process of internal combustion engine. As a result, the amount of harmful emissions during the combustion process has been significantly reduced, but an after-treatment system is required to achieve zero-emission. In the next sub-chapters, the description of these after-treatment system and their current location will be explained.

Chapter 1.3.1 Diesel oxidation catalyst (DOC) and diesel particle filter (DPF)

A diesel engine can achieve a high thermal efficiency through a higher compression ratio than a gasoline engine, but NO_x is generated due to the high combustion temperature in the stoichiometric area. Also, due to the combustion method in which fuel is injected, a large amount of soot is generated in rich stoichiometric area. The PM is after-treatment processed using a diesel particle filter (DPF). The DPF is effective in capturing the PM physically containing the soot and black smoke. Basically, the DPF is a device that captures the PM, so the exhaust gas back pressure can be negatively affects in engine operation. For this reason, a regular regeneration of the filter is required, but the maintenance is difficult. So, the heat regeneration method of the filter is used. For the heat regeneration of DPF, the filter must reach a sufficient temperature, and this temperature called the balance point temperature (BPT). When the DPF reaches at the BPT, it can promote the oxidation of carbon through two mechanisms. The first is the oxidation of the

carbon by O₂ through catalyst and thermal mechanisms. The second is the mechanism of oxidation of carbon by NO₂. In order to reduce soot, the exhaust gas after combustion was completed was used as an EGR system. This method is to keep the combustion temperature low by entraining a part of the exhaust gas containing CO₂ and H₂O, which has a large heat capacity, into the intake air to lower the O₂ concentration in the intake air. Through this, the soot and NO_x can be reduced, but it has the disadvantage of increasing CO and HC emissions because of an incomplete combustion due to a low O₂ concentration. So, the diesel oxidation catalyst (DOC) is required to reduce the CO and HC generated in this way to CO₂ and H₂O through the following reaction. The reaction mechanism in the DOC is as follows.



Through the above reaction mechanism (Eq. 1.1~3), the CO and HC are converted to CO₂ and H₂O by the DOC. In this process, the NO is oxidized to NO₂ (Eq. 1.4), and the ratio of NO to NO₂ in NO_x is an important factor in the conversion performance of selective catalytic reduction (SCR) [54]. Therefore, the DOC plays an important role in oxidizing NO to NO₂ as well as the oxidation reaction of HC and CO. A performance of the DOC is affected by the conditions in which the catalyst is placed, particularly temperature and exhaust conditions. Due to the characteristics of the catalyst, it can show high performance within a specific range of conditions. However, out of this range, performance may drop sharply and the catalyst may become inactive. Therefore, it is very important to make the activation temperature of the DOC catalyst the same as the temperature at which the DPF is thermally regenerated. In order to improve the potential of DOC as a post-treatment device, it is required to reduce the composition of precious metals while increasing the reduction performance of HC and CO, and to maximize the reduction performance of SCR by balancing the ratio of NO and NO₂ in NO_x.

Chapter 1.3.2 Selective catalytic reduction (SCR)

The SCR is an after-treatment device that converts the NO_x to N₂ and H₂O which play a role in reducing the NO_x generated during combustion in a diesel engine. The SCR catalyst is supported by a porous ceramic material such as TiO₂, and the active catalyst component is usually a non-metal (such as vanadium, molybdenum and tungsten) or a zeolite-based noble metal.

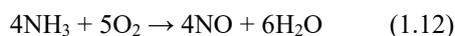
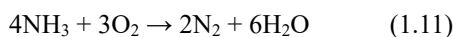
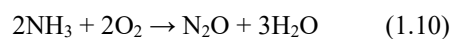
In addition, a research on a method for effective NO_x reduction of urea through activated carbon material such as activated carbon and activated carbon fiber has been conducted [55]. The non-metal catalysts such as vanadium and tungsten have a low heat resistance, but show good performance at the temperature in operating range of the general automotive and industrial boiler applications. In addition, even when a high

sulfur fuel with high sulfur content is used, it shows a good durability and continues to improve a durability against a high temperature [56-60]. The zeolite-based catalysts have a higher thermal durability than non-metallic catalysts. The zeolite-based SCR also has a low risk of corrosion because of the possibility of SO₂ oxidation is low [61]. And, compared to the vanadium-based SCR, it was activated from a lower temperature to alleviate the negative effect on the fast SCR reaction, and it showed a positive effect through the storage capacity and activation of the ammonia oxidation reaction for ammonia and nitrate [62-65]. So, the research has been conducted on how to combine these two types of catalysts [66, 67].

In SCR, the NH₃ is used as a reactant to convert the NO_x to N₂ and H₂O. However, a pure anhydrous ammonia is toxic and dangerous to use, and it requires a pressurized storage tanks and piping with thick-shell due to a high vapor pressure. The urea water is easier and safer to store and transport than a pure anhydrous ammonia. So, it is applied to SCR after thermal hydrolysis of the urea water into NH₃. Recently, the urea-SCR technology has been applied and various studies have been conducted to satisfy the environmental regulation of automobile and non-road machinery using diesel engine [68, 69]. Inside the SCR system, the NO_x is reduced through several chemical reactions as follows.



The most dominant reaction is (1.6), and the pathway of reaction (1.9), which reacts with both NO and NO₂, occurs the fastest. Modeling for these reaction mechanisms were established and the appropriateness of the modeling was verified by comparing them with the reaction mechanisms occurring in the actual catalyst [70-72]. In general, the concentration of NO₂ is low in the exhaust gas component immediately after combustion, but the NO₂ generated through DOC and DPF as described above helps to improve the reduction performance of SCR [73]. A control method to improve the SCR performance was studied by analyzing the ratio of NO and NO₂ in NO_x through the NO and NO₂ sensors installed at the front and rear of each post-treatment device [74, 75]. If the NH₃ is entrained excessively in the SCR system, the NH₃ slip may occur or the N₂O and NO may be generated through the following reaction.



Therefore, it is necessary to precisely control the introduction of NH₃ into the SCR. If the ratio of NH₃ is insufficient compared to NO_x, the reduction rate of NO_x will be quite low, and if the ratio of NH₃ is too high, there will be a lot of NH₃ slip. According to the main reaction equation (1.6), the stoichiometric NH₃/NO_x ratio (also called the ANR) is 1. Therefore, in general, the ANR is controlled to be between 0.9 and 1.0 for the best reduction performance of SCR, but there are cases where the ANR exceeds 1.0 for the maximum NO_x reduction performance. For this, an ammonia oxidation catalyst (AOC) is mounted at the rear end of the SCR to control NH₃ slip. Also, NH₃ reacted with NO₂ produces NH₄NO₃ as shown in the following reaction equation.



This causes a problem of lowering the reduction performance of SCR by containing in a solid or liquid form at a low temperature of less than 200°C. Therefore, it is necessary to consider the reaction with NH₃ after the temperature in the SCR reaches an appropriate level. In addition, the NH₃ is strongly adsorbed to SCR. In order to accurately simulate the SCR system, many studies have been conducted on the adsorption and desorption mechanism of NH₃ [76-79]. Modeling of the SCR reaction was performed considering the adsorption and desorption mechanism of NH₃. As the surface temperature of SCR increases, the amount of NH₃ adsorbed decreases and the adsorption saturation of NH₃ is quickly reached. As the flow rate of the exhaust gas increases, the NH₃ adsorption saturation state is quickly reached, and when the entrained NH₃ is stopped, the NH₃ desorption also occurs rapidly. A study to suppress the NH₃ slip was conducted through the analysis of the catalyst surface occupancy rate of NH₃ inside the SCR [79]. As time elapsed, the catalyst surface occupancy rate gradually increased in the direction from the inlet to the outlet of catalyst, and from the point when the supply of NH₃ was stopped, the catalyst surface occupancy rate decreased from the inlet. And, as the amount of urea injection increased, the catalyst surface occupancy rate increased. As a result, in order to maximize the reduction performance of SCR, it is important to consider the temperature of the SCR, the flow rate of exhaust gas, and an appropriate injection amount of urea [80, 81].

Chapter 1.4 Objective of this study

The main purpose of this study is to visualize the diesel spray flame under different fuel injection condition and ambient combustion chamber condition, and to explore an efficient after-treatment method for exhaust gases to improve a thermal efficiency of diesel engines and reduce the exhaust gases. Through the objective of this study, a sustainable development possibility and the vision for internal combustion engines can be presented.

In previous studies, there have been a various analyzes of diesel spray flame structure. However, most of these experiments and analyzes were not in a real engine condition. Therefore, it is necessary to study the diesel spray flame structure under the actual engine situation. In the case of a diesel spray injection, it can divide in two main parts as follows. The first part is a diesel spray in the area where combustion does not participate or combustion starts, and the second part is the area where the combustion starts and a flame is formed due to the fuel and air mixture. Therefore, it is necessary to analyze the structural characteristic of each diesel spray flame according to the fuel injection condition or ambient condition, and to clarify the effect of adjacent diesel spray in the multi-hole injector. To find out these characteristic and relationship, a research is the following specifics:

- Investigation of velocity distribution inside the diesel spray flame and relationship with high temperature region under actual engine situation
- Investigation of the lift-off length and liquid length according to the jet-jet angle when injection conditions or ambient conditions are different
- Investigate the backward flow between sprays and entrained into the spray according to the jet-jet angle
- Investigation of the relationship between velocity distribution and heat flux near the combustion chamber wall

Also, as mentioned in the previous section, the SCR is an after-treatment device that converts NO_x through the NH_3 hydrolyzed from urea water. In steady condition, the maximum effect of NO_x reduction can be easily achieved by injecting a certain amount of urea water. However, in the case of vehicles with transient operating condition such as diesel passenger cars or heavy-duty vehicle, ammonia slip, which does not participate in the NO_x reduction reaction, occurs when an excessive urea water is injected. To prevent this, NH_3 can be trapped through another after-treatment device called AOC, however, it makes diesel engines less economically competitive. Therefore, a urea injection strategy is required for a high reduction efficiency of SCR under various operating conditions of a diesel engine. For this, the following contents were studied.

- Investigation of ammonia adsorption and desorption characteristics inside SCR according to engine speed and exhaust gas temperature

Chapter 1.5 Thesis framework

This thesis consists of three chapters.

In Chapter 2, the relationship between the velocity distribution and flame structure of a diesel spray was studied through the PIV method during combustion situation. The velocity distribution inside the diesel spray flame was measured by the PIV method in rapid compression expansion machine (RCEM) with a single hole injector, and the local velocity fluctuation intensity was analyzed. In addition, by imaging the high-temperature region with OH* chemiluminescence, this research tried to clarify the relationship between the high-temperature region and the position with high local velocity fluctuation intensity.

In Chapter 3, it analyzed how the lift-off length and the liquid length different according to the injection condition and ambient condition when the jet-jet angle was different. And, the flow characteristic between the jets according to the jet-jet angle was studied through the PIV method. An asymmetric 6-hole injector with jet-jet angles of 30 and 45 degrees was mounted on a visible RCEM to conduct an experiment. The lift-off length and the liquid length according to the injection condition or ambient condition were measured by applying the OH* chemiluminescence and Mie scattering imaging method, respectively. And using the PIV method, when the jet-jet angle is different, how the flow characteristic appeared between jets, divided into a non-combustion and combustion conditions.

In Chapter 4, to clarify the relationship between the near-wall flow and the heat flux through the wall, the velocity distribution of the diesel spray flame and the heat flux on the combustion chamber wall were measured in RCEM, which has a two-dimensional combustion chamber. The velocity distribution of the diesel spray flame near the wall was measured by the particle image velocimetry (PIV), and the heat flux through the wall where the diesel spray flame impinges was measured using a newly developed multi-point heat flux sensor.

In Chapter 5, it conducted a research on establishing an appropriate urea injection strategy by analyzing the mechanism of NH₃ adsorption and desorption inside the SCR according to the engine speed and exhaust gas temperature. The NO_x reduction performance of SCR according to the ratio of NO and NO₂ in NO_x generated through DOC and DPF as well as the SCR temperature and the exhaust flow rate according to various engine speed and exhaust gas temperature was investigated. And, analyzing the amount and rate of NH₃ adsorption and desorption inside the SCR, a suitable urea injection strategy that can maximize NO_x reduction efficiency while suppressing NH₃ slip was considered.

References

- [1]. BP, "Statistical Review of World Energy 2021.", [Online]. Available: <https://www.bp.com/content/dam/bp/business-sites/en/global/corporate/pdfs/energy-economics/statistical-review/bp-stats-review-2021-full-report.pdf>
- [2]. ICCT, "A new life-cycle assessment of the greenhouse gas emissions of combustion engine and electric passenger cars in major markets.", [Online]. Available: <https://theicct.org/publication/a-global-comparison-of-the-life-cycle-greenhouse-gas-emissions-of-combustion-engine-and-electric-passenger-cars/>
- [3]. Funayama, Y., Nakajima, H. and Shimokawa, K., "A Study on the Effects of a Higher Compression Ratio in the Combustion Chamber on Diesel Engine Performance," SAE Technical Paper 2016-01-0722, 2016, doi:10.4271/2016-01-0722.
- [4]. Kimura, S., Matsui, Y., and Itoh, T., "Effects of Combustion Chamber Insulation on the Heat Rejection and Thermal Efficiency of Diesel Engines," SAE Technical Paper 920543, 1992, <https://doi.org/10.4271/920543>.
- [5]. Shudo, T., Nabetani, S., Nakajima, Y., "Analysis of the degree of constant volume and cooling loss in a spark ignition engine fuelled with hydrogen", SAGE journal Volume: 2 issue: 1, page(s): 81-92 Issue published: February 1, 2001, <https://doi.org/10.1243/1468087011545361>
- [6]. Assanis, D. and Badillo, E., "Transient Heat Conduction in Low-Heat-Rejection Engine Combustion Chambers," SAE Technical Paper 870156, 1987, <https://doi.org/10.4271/870156>.
- [7]. Wong, V., Bauer, W., Kamo, R., Bryzik, W., "Assessment of Thin Thermal Barrier Coatings for I.C. Engines," SAE Technical Paper 950980, 1995, <https://doi.org/10.4271/950980>.
- [8]. Saad, D., Saad, P., Kamo, L., Mekari, M., "Thermal Barrier Coatings for High Output Turbocharged Diesel Engine," SAE Technical Paper 2007-01-1442, 2007, <https://doi.org/10.4271/2007-01-1442>.
- [9]. Fujimoto, H., Yamamoto, H., Fujimoto, M., and Yamashita, H., "A Study on Improvement of Indicated Thermal Efficiency of ICE Using High Compression Ratio and Reduction of Cooling Loss," SAE Technical Paper 2011-01-1872, 2011, <https://doi.org/10.4271/2011-01-1872>.
- [10]. Kono, M., Basaki, M., Ito, M., Hashizume, T., "Cooling Loss Reduction of Highly Dispersed Spray Combustion with Restricted In-Cylinder Swirl and Squish Flow in Diesel Engine," SAE Int. J. Engines 5(2):504-515, 2012, <https://doi.org/10.4271/2012-01-0689>.
- [11]. Wakisaka, Y., Inayoshi, M., Fukui, K., Kosaka, H., "Reduction of Heat Loss and Improvement of Thermal Efficiency by Application of "Temperature Swing" Insulation to Direct-Injection Diesel Engines," SAE Int. J. Engines 9(3):1449-1459, 2016, <https://doi.org/10.4271/2016-01-0661>.

- [12]. Kawaguchi, A., Iguma, H., Yamashita, H., Takada, N., "Thermo-Swing Wall Insulation Technology; - A Novel Heat Loss Reduction Approach on Engine Combustion Chamber -," SAE Technical Paper 2016-01-2333, 2016, <https://doi.org/10.4271/2016-01-2333>.
- [13]. Allocca, L., Belardini, P., Bertoli, C., Corcione, F., "Experimental and Numerical Analysis of a Diesel Spray," SAE Technical Paper 920576, 1992, <https://doi.org/10.4271/920576>.
- [14]. Naber, J. and Siebers, D., "Effects of Gas Density and Vaporization on Penetration and Dispersion of Diesel Sprays," SAE Technical Paper 960034, 1996, <https://doi.org/10.4271/960034>.
- [15]. Khalid, A., Yatsufusa, T., Miyamoto, T., Kawakami, J., Kidoguchi, Y., "Analysis of Relation between Mixture Formation during Ignition Delay Period and Burning Process in Diesel Combustion", SAE Technical Paper, 2009-32-0018, 2009
- [16]. Zama, Y., Ochiai, W., Sugawara, K., Furuhashi, T., Arai, M., "Study on Mixing Process of Diesel Spray under High Ambient Gas Density Condition," Atomization and Sprays, Volume 23, Issue 5, 2013, pp. 443-461, [10.1615/AtomizSpr.2013007347](https://doi.org/10.1615/AtomizSpr.2013007347)
- [17]. Kobashi, Y., Yokogawa, K., Miyabe, H., Hase, R., Kato, S., "Flow Fields and Turbulent Characteristics in Non-Evaporating Diesel Sprays", Volume 28, Issue 8, 2018, pp. 735-749 DOI: [10.1615/AtomizSpr.2018026468](https://doi.org/10.1615/AtomizSpr.2018026468)
- [18]. Pang, K., Jangi, M., Bai, X., Schramm, J., Walther, J., "Modelling of diesel spray flames under engine-like conditions using an accelerated Eulerian Stochastic Field method", Combustion and Flame, Volume 193, 2018, Pages 363-383, ISSN 0010-2180, <https://doi.org/10.1016/j.combustflame.2018.03.030>.
- [19]. Pang, K., Jangi, M., Bai, X., Schramm, J., Walther, J., Glarborg, P., "Effects of ambient pressure on ignition and flame characteristics in diesel spray combustion", Fuel, Volume 237, 2019, Pages 676-685, ISSN 0016-2361, <https://doi.org/10.1016/j.fuel.2018.10.020>.
- [20]. Desantes, J., García, J., Novella, R., Pérez, E., "Application of a flamelet-based CFD combustion model to the LES simulation of a diesel-like reacting spray", Computers & Fluids, Volume 200, 2020, 104419, ISSN 0045-7930, <https://doi.org/10.1016/j.compfluid.2019.104419>.
- [21]. Kamimoto, T., Yokota, H., Kobayashi, H., "Effect of High Pressure Injection on Soot Formation Processes in a Rapid Compression Machine to Simulate Diesel Flames," SAE Technical Paper 871610, 1987, <https://doi.org/10.4271/871610>.
- [22]. Allocca, L., Belardini, P., Bertoli, C., Corcione, F., "Experimental and Numerical Analysis of a Diesel Spray," SAE Technical Paper 920576, 1992, <https://doi.org/10.4271/920576>.
- [23]. Kojima, H., Kawanabe, H., Ishiyama, T., "A Study on Mixture Formation Process in a Diesel Spray Using PLIF Method", THIESEL 2010 Conference on Thermo- and Fluid Dynamic Processes in Diesel Engines
- [24]. Desantes, J., Pastor, J., García-Oliverj, J., Pastor, j., "A 1D model for the description of mixing-

- controlled reacting diesel sprays”, *Combustion and Flame*, Volume 156, Issue 1, 2009, Pages 234-249, ISSN 0010-2180, <https://doi.org/10.1016/j.combustflame.2008.10.008>.
- [25]. Milan, V., Zvonimir, P., Wilfried, E., Neven, D., “Modelling spray and combustion processes in diesel engine by using the coupled Eulerian–Eulerian and Eulerian–Lagrangian method”, *Energy Conversion and Management*, Volume 125, 2016, Pages 15-25, ISSN 0196-8904, <https://doi.org/10.1016/j.enconman.2016.03.072>.
- [26]. Mehdi, J., Rickard, S., Bengt, J., Xue-Song, Bai, “On large eddy simulation of diesel spray for internal combustion engines”, *International Journal of Heat and Fluid Flow*, Volume 53, 2015, Pages 68-80, ISSN 0142-727X, <https://doi.org/10.1016/j.ijheatfluidflow.2015.02.002>.
- [27]. Zhou, L., Luo, K., Qin, W., Jia, M., Shuai, S., “Large eddy simulation of spray and combustion characteristics with realistic chemistry and high-order numerical scheme under diesel engine-like conditions”, *Energy Conversion and Management*, Volume 93, 2015, Pages 377-387, ISSN 0196-8904, <https://doi.org/10.1016/j.enconman.2015.01.033>.
- [28]. Cao, Z., Nishino, K., Mizuno, S., Torii, K., “PIV Measurement of Internal Structure of Diesel Fuel Spray”, *Transactions of the Japan Society of Mechanical Engineers Series B*, 2001, Volume 67, Issue 653, Pages 241-248, Released on J-STAGE March 28, 2008, Online ISSN 1884-8346, Print ISSN 0387-5016, <https://doi.org/10.1299/kikaib.67.241>
- [29]. Dec, J., Espey, C., "Soot and Fuel Distributions in a D.I. Diesel Engine via 2-D Imaging," SAE Technical Paper 922307, 1992, <https://doi.org/10.4271/922307>.
- [30]. Dec, J., "A Conceptual Model of DI Diesel Combustion Based on Laser-Sheet Imaging*," SAE Technical Paper 970873, 1997, <https://doi.org/10.4271/970873>.
- [31]. Flynn, P., Durrett, R., Hunter, G., zur Loye, A. et al., "Diesel Combustion: An Integrated View Combining Laser Diagnostics, Chemical Kinetics, And Empirical Validation," SAE Technical Paper 1999-01-0509, 1999, <https://doi.org/10.4271/1999-01-0509>.
- [32]. Kosaka, H., Aizawa, T., Kamimoto, T., “Two-dimensional imaging of ignition and soot formation processes in a diesel flame”, *Int. J. Engine Res.* Vol. 6 No. 1, <https://doi.org/10.1243/146808705X7347>
- [33]. Kosaka, H., Nishigaki, T., Kamimoto, T., Sano, T., "Simultaneous 2-D Imaging of OH Radicals and Soot in a Diesel Flame by Laser Sheet Techniques," SAE Technical Paper 960834, 1996, <https://doi.org/10.4271/960834>.
- [34]. Siebers, D., "Liquid-Phase Fuel Penetration in Diesel Sprays," SAE Technical Paper 980809, 1998, <https://doi.org/10.4271/980809>.
- [35]. Verhoeven, D., Vanhemelryck, J., and Baritaud, T., "Macroscopic and Ignition Characteristics of High-Pressure Sprays of Single-Component Fuels," SAE Technical Paper 981069, 1998, <https://doi.org/10.4271/981069>.
- [36]. Siebers, D. and Higgins, B., "Flame Lift-Off on Direct-Injection Diesel Sprays Under Quiescent Conditions," SAE Technical Paper 2001-01-0530, 2001, <https://doi.org/10.4271/2001-01-0530>.

- [37]. Siebers, D., Higgins, B., Pickett, L., "Flame Lift-Off on Direct-Injection Diesel Fuel Jets: Oxygen Concentration Effects," SAE Technical Paper 2002-01-0890, 2002, <https://doi.org/10.4271/2002-01-0890>.
- [38]. Pickett, L., Siebers, D., and Idicheria, C., "Relationship Between Ignition Processes and the Lift-Off Length of Diesel Fuel Jets," SAE Technical Paper 2005-01-3843, 2005, <https://doi.org/10.4271/2005-01-3843>.
- [39]. Donkerbroek, A., Boot, M., Luijten, C., Dam, N., Meulen, J., "Flame lift-off length and soot production of oxygenated fuels in relation with ignition delay in a DI heavy-duty diesel engine", *Combustion and Flame*, Volume 158, Issue 3, 2011, Pages 525-538, ISSN 0010-2180, <https://doi.org/10.1016/j.combustflame.2010.10.003>.
- [40]. Persson, H., Andersson, Ö., Egnell, R., "Fuel effects on flame lift-off under diesel conditions", *Combustion and Flame*, Volume 158, Issue 1, 2011, Pages 91-97, ISSN 0010-2180, <https://doi.org/10.1016/j.combustflame.2010.07.020>.
- [41]. Payri, R., Viera, J., Pei, Y., Som, S., "Experimental and numerical study of lift-off length and ignition delay of a two-component diesel surrogate", *Fuel*, Volume 158, 2015, Pages 957-967, ISSN 0016-2361, <https://doi.org/10.1016/j.fuel.2014.11.072>.
- [42]. Li, D., He, Z., Xuan, T., Zhong, W., Cao, J., Wang, Q., Wang, P., "Simultaneous capture of liquid length of spray and flame lift-off length for second-generation biodiesel/diesel blended fuel in a constant volume combustion chamber", *Fuel*, Volume 189, 2017, Pages 260-269, ISSN 0016-2361, <https://doi.org/10.1016/j.fuel.2016.10.058>.
- [43]. Rusly, A., Le, M., Kook, S., Hawkes, E., "The shortening of lift-off length associated with jet-wall and jet-jet interaction in a small-bore optical diesel engine", *Fuel*, Volume 125, 2014, Pages 1-14, ISSN 0016-2361, <https://doi.org/10.1016/j.fuel.2014.02.004>.
- [44]. Abdullah, M., Shinobu, A., Tomoki, K., Aizawa, T., "Effects of inversed-delta injection rate shaping on diesel spray flame liquid length, lift-off length and soot onset", *Fuel*, Volume 258, 2019, 116170, ISSN 0016-2361, <https://doi.org/10.1016/j.fuel.2019.116170>.
- [45]. Abdullah, M., Shinobu, A., Tomoki, K., Aizawa, T., Shimada, T., Aizawa, T., "Investigation of inversed-delta injection rate shaping diesel spray flame structure and combustion characteristics towards thermal efficiency improvement", *Applied Thermal Engineering*, Volume 160, 2019, 113986, ISSN 1359-4311, <https://doi.org/10.1016/j.applthermaleng.2019.113986>.
- [46]. Chartier, C., Aronsson, U., Andersson, Ö., Egnell, R., Johansson, B., "Influence of jet-jet interactions on the lift-off length in an optical heavy-duty DI diesel engine", *Fuel*, Volume 112, 2013, Pages 311-318, ISSN 0016-2361, <https://doi.org/10.1016/j.fuel.2013.05.021>.
- [47]. Toda, N., Yamashita, H., Mashida, M., "PTV analysis of the entrained air into the diesel spray at high-pressure injection", *Proceedings Volume 9232, International Conference on Optical Particle Characterization (OPC 2014); 92320C (2014)*, <https://doi.org/10.1117/12.2063632>

- [48]. Fuyuto, T., Hattori, Y., Yamashita, H., and Mashida, M., "Backward Flow of Hot Burned Gas Surrounding High-Pressure Diesel Spray Flame from Multi-hole Nozzle," *SAE Int. J. Engines* 9(1):71-83, 2016, <https://doi.org/10.4271/2015-01-1837>.
- [49]. Squaiella, L., Martins, C., Lacava, P., "Strategies for emission control in diesel engine to meet Euro VI", *Fuel*, Volume 104, 2013, Pages 183-193, ISSN 0016-2361, <https://doi.org/10.1016/j.fuel.2012.07.027>.
- [50]. Ko, J., Jin, D., Jang, W., Myung, C., Kwon, S., Park, S., "Comparative investigation of NO_x emission characteristics from a Euro 6-compliant diesel passenger car over the NEDC and WLTC at various ambient temperatures", *Applied Energy*, Volume 187, 2017, Pages 652-662, ISSN 0306-2619, <https://doi.org/10.1016/j.apenergy.2016.11.105>.
- [51]. Myung, C., Jang, W., Kwon, S., Ko, J., Jin, D., Park, S., "Evaluation of the real-time de-NO_x performance characteristics of a LNT-equipped Euro-6 diesel passenger car with various vehicle emissions certification cycles", *Energy*, Volume 132, 2017, Pages 356-369, ISSN 0360-5442, <https://doi.org/10.1016/j.energy.2017.05.089>.
- [52]. Cha, J., Lee, J., Chon, M., "Evaluation of real driving emissions for Euro 6 light-duty diesel vehicles equipped with LNT and SCR on domestic sales in Korea", *Atmospheric Environment*, Volume 196, 2019, Pages 133-142, ISSN 1352-2310, <https://doi.org/10.1016/j.atmosenv.2018.09.029>.
- [53]. Costagliola, M., Costabile, M., Prati, M., "Impact of road grade on real driving emissions from two Euro 5 diesel vehicles, *Applied Energy*, Volume 231, 2018, Pages 586-593, ISSN 0306-2619, <https://doi.org/10.1016/j.apenergy.2018.09.108>.
- [54]. Salman, A., Enger, B., Auvray, X., Lødeng, R., Menon, M., Waller, D., Rønning, M., "Catalytic oxidation of NO to NO₂ for nitric acid production over a Pt/Al₂O₃ catalyst", *Applied Catalysis A: General*, Volume 564, 2018, Pages 142-146, ISSN 0926-860X, <https://doi.org/10.1016/j.apcata.2018.07.019>.
- [55]. Shirahama, N., Mochida, I., Korai, Y., Choi, K., Enjoji, T., Shimohara, T., Yasutake, A., "Reaction of NO with urea supported on activated carbons", *Applied Catalysis B: Environmental*, Volume 57, Issue 4, 2005, Pages 237-245, ISSN 0926-3373, <https://doi.org/10.1016/j.apcatb.2004.04.004>.
- [56]. Dumesic, J., Topsøe, N., Topsøe, H., Chen, Y., Slabiak, T., "Kinetics of Selective Catalytic Reduction of Nitric Oxide by Ammonia over Vanadia/Titania", *Journal of Catalysis*, Volume 163, Issue 2, 1996, Pages 409-417, ISSN 0021-9517, <https://doi.org/10.1006/jcat.1996.0342>.
- [57]. Girard, J., Montreuil, C., Kim, J., Cavataio, G., "Technical Advantages of Vanadium SCR Systems for Diesel NO_x Control in Emerging Markets," *SAE Int. J. Fuels Lubr.* 1(1):488-494, 2009, <https://doi.org/10.4271/2008-01-1029>.
- [58]. Nahanvandi, M., "Selective Catalytic Reduction (SCR) of NO by Ammonia over V₂O₅/TiO₂ Catalyst in a Catalytic Filter Medium and Honeycomb Reactor: A Kinetic Modeling Study", Vol. 32, No. 04, pp. 875 - 893, 2015 <https://doi.org/10.1590/0104-6632.20150324s00003584>

- [59]. Liu, Y., Liu, Z., Mnichowicz, N., Harinath, A., Li, H., Bahrami, B., “Chemical deactivation of commercial vanadium SCR catalysts in diesel emission control application”, *Chemical Engineering Journal*, Volume 287, 2016, Pages 680-690, ISSN 1385-8947, <https://doi.org/10.1016/j.cej.2015.11.043>.
- [60]. Xu, L., Niu, S., Wang, D., Lu, C., Zhang, Q., Zhang, K., Li, J., “Selective catalytic reduction of NO_x with NH₃ over titanium modified Fe_xMg_yO_z catalysts: Performance and characterization”, *Journal of Industrial and Engineering Chemistry*, Volume 63, 2018, Pages 391-404, ISSN 1226-086X, <https://doi.org/10.1016/j.jiec.2018.02.039>.
- [61]. Traa, Y., Burger, B., Weitkamp, J., “Zeolite-based materials for the selective catalytic reduction of NO_x with hydrocarbons”, *Microporous and Mesoporous Materials*, Volume 30, Issue 1, 1999, Pages 3-41, ISSN 1387-1811, [https://doi.org/10.1016/S1387-1811\(99\)00030-X](https://doi.org/10.1016/S1387-1811(99)00030-X).
- [62]. Grossale, A., Nova, I., Tronconi, E., “Ammonia blocking of the “Fast SCR” reactivity over a commercial Fe-zeolite catalyst for Diesel exhaust aftertreatment”, *Journal of Catalysis*, Volume 265, Issue 2, 2009, Pages 141-147, ISSN 0021-9517, <https://doi.org/10.1016/j.jcat.2009.04.014>.
- [63]. Colombo, M., Nova, I., Tronconi, E., “A comparative study of the NH₃-SCR reactions over a Cu-zeolite and a Fe-zeolite catalyst”, *Catalysis Today*, Volume 151, Issues 3–4, 2010, Pages 223-230, ISSN 0920-5861, <https://doi.org/10.1016/j.cattod.2010.01.010>.
- [64]. Xu, H., Li, Y., Xu, B., Cao, Y., Feng, X., Sun, M., Gong, M., Chen, Y., “Effectively promote catalytic performance by adjusting W/Fe molar ratio of FeW_x/Ce_{0.68}Zr_{0.32}O₂ monolithic catalyst for NH₃-SCR”, *Journal of Industrial and Engineering Chemistry*, Volume 36, 2016, Pages 334-345, ISSN 1226-086X, <https://doi.org/10.1016/j.jiec.2016.02.024>.
- [65]. Lee, K., Kosaka, H., Sato, S., Yokoi, T., Choi, B., Kim, D., “Effects of Cu loading and zeolite topology on the selective catalytic reduction with C₃H₆ over Cu/zeolite catalysts”, *Journal of Industrial and Engineering Chemistry*, Volume 72, 2019, Pages 73-86, ISSN 1226-086X, <https://doi.org/10.1016/j.jiec.2018.12.005>.
- [66]. Jung, Y., Shin, T., Pyo, Y., Cho, C., Jang, J., Kim, G., “NO_x and N₂O emissions over a Urea-SCR system containing both V₂O₅-WO₃/TiO₂ and Cu-zeolite catalysts in a diesel engine”, *Chemical Engineering Journal*, Volume 326, 2017, Pages 853-862, ISSN 1385-8947, <https://doi.org/10.1016/j.cej.2017.06.020>.
- [67]. Cho, C., Pyo, Y., Jang, J., Kim, G., Shin, Y., “NO_x reduction and N₂O emissions in a diesel engine exhaust using Fe-zeolite and vanadium based SCR catalysts”, *Applied Thermal Engineering*, Volume 110, 2017, Pages 18-24, ISSN 1359-4311, <https://doi.org/10.1016/j.applthermaleng.2016.08.118>.
- [68]. Gieshoff, J., Schäfer-Sindlinger, A., Spurk, P., van den Tillaart, J., "Improved SCR Systems for Heavy Duty Applications," *SAE Technical Paper 2000-01-0189*, 2000, <https://doi.org/10.4271/2000-01-0189>.
- [69]. Koebel, M., Elsener, M., Kleemann, M., “Urea-SCR: a promising technique to reduce NO_x emissions from automotive diesel engines”, *Catalysis Today*, Volume 59, Issues 3–4, 2000, Pages 335-345, ISSN

0920-5861, [https://doi.org/10.1016/S0920-5861\(00\)00299-6](https://doi.org/10.1016/S0920-5861(00)00299-6).

- [70]. Ciardelli, C., Nova, I., Tronconi, E., Chatterjee, D., Burkhardt, T., Weibel, M., "NH₃-SCR of NO_x for diesel exhausts aftertreatment: role of NO₂ in catalytic mechanism, unsteady kinetics and monolith converter modelling", *Chemical Engineering Science*, Volume 62, Issues 18–20, 2007, Pages 5001-5006, ISSN 0009-2509, <https://doi.org/10.1016/j.ces.2006.11.031>.
- [71]. Ciardelli, C., Nova, I., Tronconi, E., Chatterjee, C., Bandl-Konrad, B., Weibel, M., Krutzsch, B., "Reactivity of NO/NO₂-NH₃ SCR system for diesel exhaust aftertreatment: Identification of the reaction network as a function of temperature and NO₂ feed content", *Applied Catalysis B: Environmental*, Volume 70, Issues 1–4, 2007, Pages 80-90, ISSN 0926-3373, <https://doi.org/10.1016/j.apcatb.2005.10.041>.
- [72]. Colombo, M., Nova, I., Tronconi, E., "Detailed kinetic modeling of the NH₃-NO/NO₂ SCR reactions over a commercial Cu-zeolite catalyst for Diesel exhausts after treatment", *Catalysis Today*, Volume 197, Issue 1, 2012, Pages 243-255, ISSN 0920-5861, <https://doi.org/10.1016/j.cattod.2012.09.002>.
- [73]. Nova, I., Ciardelli, C., Tronconi, E., Chatterjee, D., Bandl-Konrad, B., "NH₃-NO/NO₂ chemistry over V-based catalysts and its role in the mechanism of the Fast SCR reaction", *Catalysis Today*, Volume 114, Issue 1, 2006, Pages 3-12, ISSN 0920-5861, <https://doi.org/10.1016/j.cattod.2006.02.012>.
- [74]. Chen, P., Wang, J., "Nonlinear and adaptive control of NO/NO₂ ratio for improving selective catalytic reduction system performance", *Journal of the Franklin Institute*, Volume 350, Issue 8, 2013, Pages 1992-2012, ISSN 0016-0032, <https://doi.org/10.1016/j.jfranklin.2013.05.020>.
- [75]. Bonfils, A., Creff, Y., Lepreux, O., Petit, N., "Closed-loop control of a SCR system using a NO_x sensor cross-sensitive to NH₃", *Journal of Process Control*, Volume 24, Issue 2, 2014, Pages 368-378, ISSN 0959-1524, <https://doi.org/10.1016/j.jprocont.2013.08.010>.
- [76]. Wang, T., Baek, S., Jung, M., Yeo, G., "A Study of NH₃ Adsorption/Desorption Characteristics in the Monolithic NH₃-SCR Reactor", *Transactions of KSAE*, Vol.14, No.3, pp. 125-132 (2006)
- [77]. Schuler, A., Votsmeier, M., Kiwic, P., Gieshoff, J., Hautpmann, W., Drochner, A., Vogel, H., "NH₃-SCR on Fe zeolite catalysts – From model setup to NH₃ dosing", *Chemical Engineering Journal*, Volume 154, Issues 1–3, 2009, Pages 333-340, ISSN 1385-8947, <https://doi.org/10.1016/j.cej.2009.02.037>.
- [78]. Feng, T., Lü, L., "The characteristics of ammonia storage and the development of model-based control for diesel engine urea-SCR system", *Journal of Industrial and Engineering Chemistry*, Volume 28, 2015, Pages 97-109, ISSN 1226-086X, <https://doi.org/10.1016/j.jiec.2015.02.004>.
- [79]. Wang, T., Baek, S., Jung, M., Yeo, G., "A Study of NH₃ Adsorption/Desorption Characteristics and Model Based Control in the Urea-SCR System", *Transactions of KSAE*, Vol. 24, No. 3, pp.302-309 (2016), <http://dx.doi.org/10.7467/KSAE.2016.24.3.302>
- [80]. Willems, F., Cloudt, R., van den Eijnden, E., van Genderen, M., "Is Closed-Loop SCR Control Required to Meet Future Emission Targets?," *SAE Technical Paper 2007-01-1574*, 2007,

<https://doi.org/10.4271/2007-01-1574>.

- [81]. Zhao, J., Chen, Z., Hu, Y., Chen, H., “Urea-SCR Process Control for Diesel Engine Using Feedforward-Feedback Nonlinear Method”, IFAC-PapersOnLine, Volume 48, Issue 8, 2015, Pages 367-372, ISSN 2405-8963, <https://doi.org/10.1016/j.ifacol.2015.08.209>.

Chapter 2. The Analyzing the Structure of the Diesel Spray Flame by Time Resolved PIV with OH* Chemiluminescence

2.1 Introduction

To achieve a high thermal efficiency through combustion control of a diesel engine, it is necessary to reduce the cooling loss and the exhaust loss by increasing the compression ratio (or expansion ratio) and the degree of constant volume [1-3]. In order to increase the degree of constant volume, it is important to shorten the combustion duration. According to numerical research by Kojima et al. [4], the heat release in a diesel spray flame during mixing-controlled combustion is considered to come mainly from the diffusion flame. Therefore, it is considered effective to increase the local heat release rate by enhancing the turbulence in the region around the stoichiometric ratio where the chemical reaction proceeds mainly in order to shorten the combustion duration.

Experimental and numerical studies on the fuel concentration and velocity distribution in diesel sprays have been conducted. Khalid et al. [5] investigated the effect of injection pressure and surrounding gas flow on mixture formation. When the injection pressure is high, the mixture formation improves during the ignition delay period. Cao et al. [6] conducted the particle image velocimetry (PIV) for the non-evaporating diesel spray and revealed that the local droplet concentration is significantly low in the core of vortical motion and that the droplets tend to accumulate in the regions of low vorticity of droplet field. Kobashi et al. [7] studied the velocity distribution and turbulent characteristics of the non-evaporating diesel spray using PIV and showed that the highest turbulence intensity corresponding to the mixing boundary [8] is located slightly away from the center of the spray axis. Kojima et al. [9] demonstrated the instantaneous distribution of fuel concentration in non-reacting diesel spray under a high temperature condition by planar laser induced fluorescence (PLIF) technique. It was found that when the injection pressure increased and the nozzle diameter decreased, the mixture formation enhanced immediately after injection starts, and the mixture became lean quickly after the end of injection. Bruneaux [10,11] showed the mixing process of high-pressure diesel jets by using laser induced exciplex fluorescence (LIEF). It was found that increasing the injection pressure enhanced the atomization at the nozzle outlet, resulting in a more distributed vapor phase, hence resulting in better mixing. Bottone et al. [12] studied the numerical analysis of diesel spray combustion with large eddy simulation (LES) and conditional moment closure (CMC) method. It was found that LES-CMC methodology can reproduce well the diesel spray combustion experiment results like auto-ignition time and flame lift-off length. However, most experimental studies have focused on non-evaporating or non-reacting sprays, and the relationship between velocity, fuel concentration, and temperature in diesel spray flames has not been fully clarified.

The aim of this study was to reveal the velocity distribution and the high-temperature region of the diesel spray flame in actual engine combustion situation. PIV was applied to a diesel spray flame in a rapid compression and expansion machine (RCEM) installed a single-hole injector to measure the velocity distribution and determined the intensity of local velocity fluctuation. In addition, the location of the high-temperature region was visualized by OH* chemiluminescence imaging, and the relationship between the location of the high intensity of OH* radical and the location of the high intensity of local velocity fluctuation was discussed.

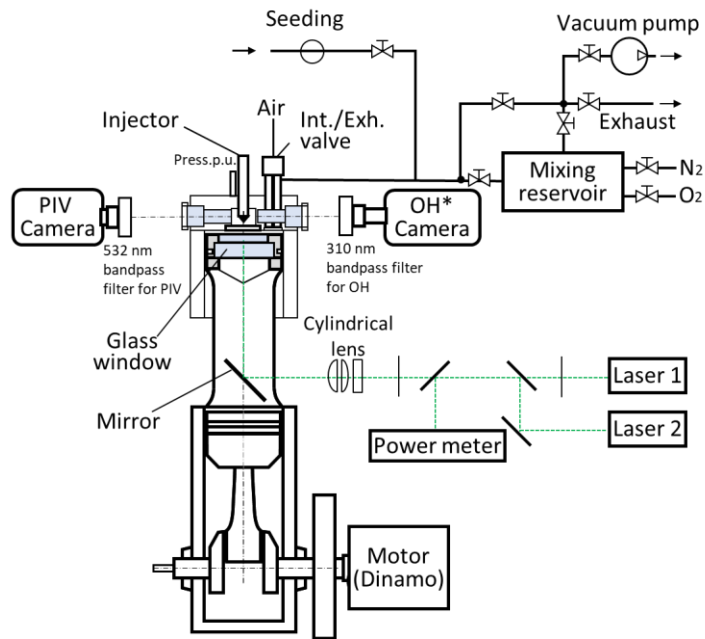


Figure 2.1 Schematic of the experimental setup

2.2 Experimental setup

2.2.1 Experimental Apparatus

The experimental equipment consists of an RCEM, which can be observed the inside of the combustion chamber; a fuel injection system; a control unit; and an intake and exhaust system, which are shown in Figure 2.1.

Table 2.1 Specification of the RCEM

Bore × Stroke	85 mm × 96 mm
Displacement	$0.550 \times 10^{-3} \text{ m}^3$
Compression ratio	14.6
Injection system	Common rail system

The specification of the RCEM is shown in Table 2.1. The bore and stroke are 85 mm and 96.9 mm, respectively, the compression ratio is 14.6, and the displacement is 0.55 L. The swirl ratio of this RCEM is zero. For this study, a cylinder head was designed to enable visualization in both directions of the combustion chamber specifically for simultaneous PIV and OH* chemiluminescence imaging. In addition, an extension piston was used to put the laser sheet for PIV into the combustion chamber, and a fixed mirror was used inside the extension piston so that the reflected laser sheet was incident from the piston to the cylinder head.

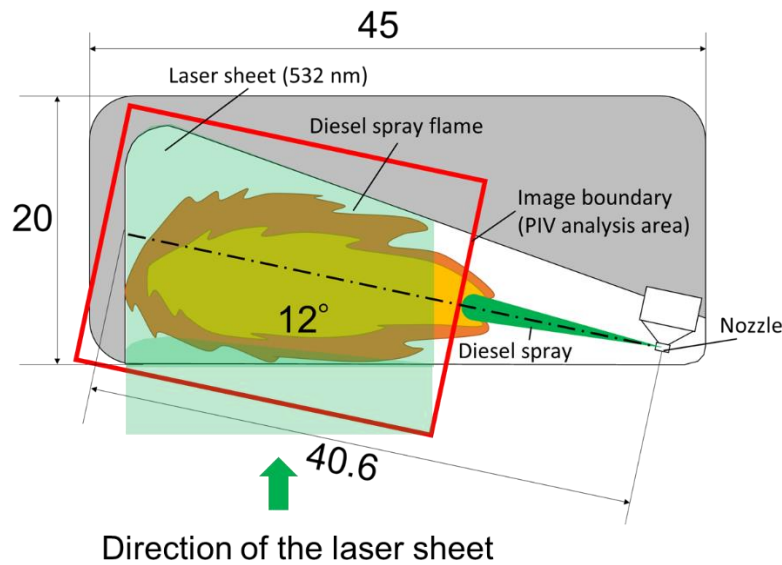


Figure 2.2 Visualized area for PIV and OH* chemiluminescence in RCEM

Figure 2.2 shows the shape of the combustion chamber and the visualized area. In order to irradiate the laser sheet into the spray axis and to take images for PIV and OH* chemiluminescence, the combustion chamber and the spray injection direction are designed in an upside-down shape.

The combustion chamber has a quasi-two-dimensional (2D) cavity-shaped, which realize a single spray part of piston cavity in an actual diesel engine, and a single-hole injector was installed. There are windows on both sides of the combustion chamber, allowing for the PIV image and the OH* chemiluminescence image to be captured simultaneously. The top of the piston is made of sapphire glass, allowing the laser to pass through from the bottom. For this, the upper part of the piston shape is flat. The height and width of the window are 20 mm and 45 mm, respectively. The distance from the injector tip to the combustion chamber wall is 40.6 mm. When the laser sheet passes through a high-density region of the fuel droplets, the scattered light intensity from the liquid appears too bright, making it difficult to analyze the flow velocity. Therefore, the laser sheet was irradiated into the green area which the liquid part doesn't include as shown in Figure 2.2.

The experimental conditions are shown in Table 2.2. The cranking speed was 900 rpm. A common-rail injection system with a piezoelectric injector was used, and the nozzle hole diameter was 0.133 mm. The injection amount was 10.2 mg, and the start of injection timing was -6.4° ATDC. The in-cylinder pressure and the temperature inside the cylinder at the start of injection were set to 8 MPa and 800 K, respectively. The injection pressure was set to 120 MPa, 90 MPa, and 60 MPa. A solvent made of $n\text{-C}_{11}\text{H}_{24}$, $n\text{-C}_{12}\text{H}_{26}$, and $\text{iso-C}_{12}\text{H}_{26}$ was used as fuel, because a diesel fuel had a too much soot formed which a soot cloud covers the scattering light making it impossible to analyze the velocity distribution. The cetane number of the solvent was 57, which is comparable to that of a diesel fuel. Although the soot cloud was also formed when using the solvent, the PIV analysis was possible in most areas. And also, the oxygen concentration was set to 15% to reduce the effect of luminous flame on the PIV and to simulate the exhaust gas recirculation (EGR) situation. The experimental process proceeded as follows. First, the mixing reservoir and the inside of the combustion chamber are made into a vacuum state, and the pressure and oxygen concentration suitable for the experimental conditions are established. Then, with the intake valve open, the RCEM is driven at the cranking speed that satisfies the experimental conditions using a motor. When the intake gas temperature reaches the target, the intake valve is closed and the fuel is injected to conduct a one-cycle combustion experiment. The tracer for the PIV analysis was introduced into the combustion chamber just before the intake valve is closed.

Table 2.2. Experiment conditions

Cranking speed	900 rpm
Nozzle-hole diameter	0.133 mm
Injection quantity	10.2 mg (13.7 mm ³)
Start of injection (SOI)	-6.4° ATDC
In-cylinder pressure @ SOI	8 MPa
In-cylinder temperature @ SOI	800 K
Injection pressure	120, 90, 60 MPa
Fuel	Solvent (Cetane number : 57), $n\text{-C}_{11}\text{H}_{24}$, $n\text{-C}_{12}\text{H}_{26}$, and $\text{iso-C}_{12}\text{H}_{26}$
Composition of the intake gas	O ₂ : 15 mol%, N ₂ : 85 mol%

The heat release rate was calculated using the following Equation (2.1);

$$\frac{dQ}{d\theta} = \frac{\gamma}{\gamma - 1} p \frac{dV}{d\theta} + \frac{1}{\gamma - 1} V \frac{dp}{d\theta} \quad (2.1)$$

The variables $dQ/d\theta$, γ , V , p , and θ are the heat release rate, the specific heat ratio, the in-cylinder volume, the in-cylinder pressure, and the crank angle, respectively. The constant γ was set to 1.33.

2.2.2 Imaging technique

The PIV and OH* chemiluminescence imaging techniques were applied. Imaging conditions are shown in Table 2.3. The PIV was used to determine the velocity distribution. PIV is a method of measuring the velocity through the moving distance and the time interval between the images by the tracer particles into the fluid and capturing the tracers scattered by the laser. Set the grid of the captured image, which is the interrogation window in table 2.3, and calculate the overall average movement distance of the tracers in each grid. Since the flow vector within each grid can be calculated from this result, the flow characteristics of the entire fluid can be analyzed through PIV. For the PIV, a second harmonic generation Nd:YAG laser with a wave length of 532 nm was used, and two laser devices were used to shoot the laser at very short time intervals. The images were obtained using a high-speed camera, and only the scattered laser light could be captured in images by using a bandpass filter of 530 ± 10 nm. The spatial resolution of the images is $53 \mu\text{m}/\text{pixel}$. As a tracer for the PIV measurement, a SiO₂ porous particle (Godd-ball) with an average diameter of $10 \mu\text{m}$ was used. The interrogation window and the overlap for the PIV analysis were 16×16 pixels and 50%, respectively, which was suitable for the velocity range in the high-temperature region. The OH* chemiluminescence images were taken using another high-speed camera. The OH* Radical is one of the most intermediate in combustion chemistry, so it is known for the stoichiometric region in diesel spray flame, which is the location of high-temperature combustion. So, the OH chemiluminescence image was also clearly known about the high-temperature region. A bandpass filter of 310 ± 10 nm was used with image intensifier to an image of OH* chemiluminescence.

Table 2.3. Imaging condition of PIV and OH* chemiluminescence

PIV	Spatial resolution	$53 \mu\text{m}/\text{pixel}$
	Frequency	20 kHz
	Interval 1 st , 2 nd	$6 \mu\text{s}$
	Laser wavelength	532 nm
	PIV tracer	Godd ball (SiO ₂): $10 \mu\text{m}$
	Analyzing algorithm	Multi-pass interrogation
	Interrogation window	16×16 pixels
	Overlap	50 %
OH	Spatial resolution	$57 \mu\text{m}/\text{pixel}$
	Frequency	20 kHz

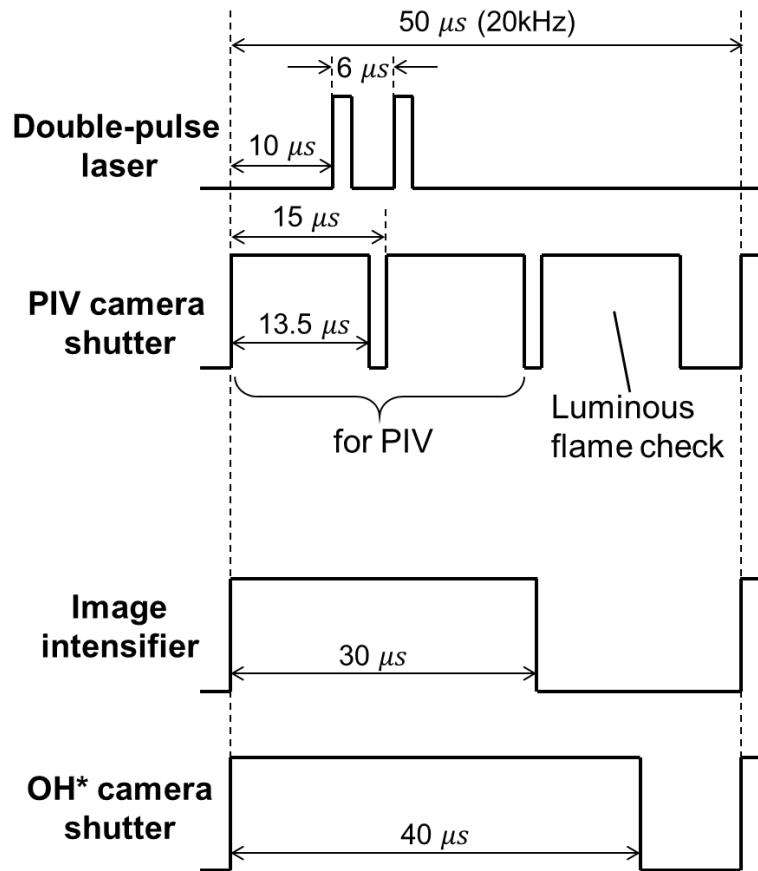


Figure 2.3 Signal sequence for PIV and OH* chemiluminescence for simultaneous imaging

Figure 2.3 shows the temporal sequence of the laser, imaging signal for the PIV camera, and imaging signals for OH* chemiluminescence. The images for PIV were taken in separate frames. In addition, the third frame captured only luminous flame. Attempts were made to determine how the luminous flame had disturbed the PIV area. For the OH* chemiluminescence imaging, the exposure was set to 40 μs , and the gate opening duration of the image intensifier was set to 30 μs . Figure 2.4 shows the PIV and OH* chemiluminescence images taken at the same moment by the signal sequence. In the PIV image, the velocity distribution between the diesel spray and the surrounding air was clearly distinguished like a yellow boundary line. The boundary line of diesel spray flame in PIV was judged through the points where the flow in the opposite direction to the diesel spray injection direction appeared. The OH* chemiluminescence image also clearly shows the high-temperature region like the red boundary line. The OH* radical boundary line representing the high-temperature region was judged as the point where the luminous intensity began to appear in the vertical section with respect to the diesel spray axis. By synthesizing these two images, the relationship between the velocity distribution of the diesel spray flame and the high-temperature region was analyzed using the region in which OH* radicals appear and the velocity distribution measured by PIV.

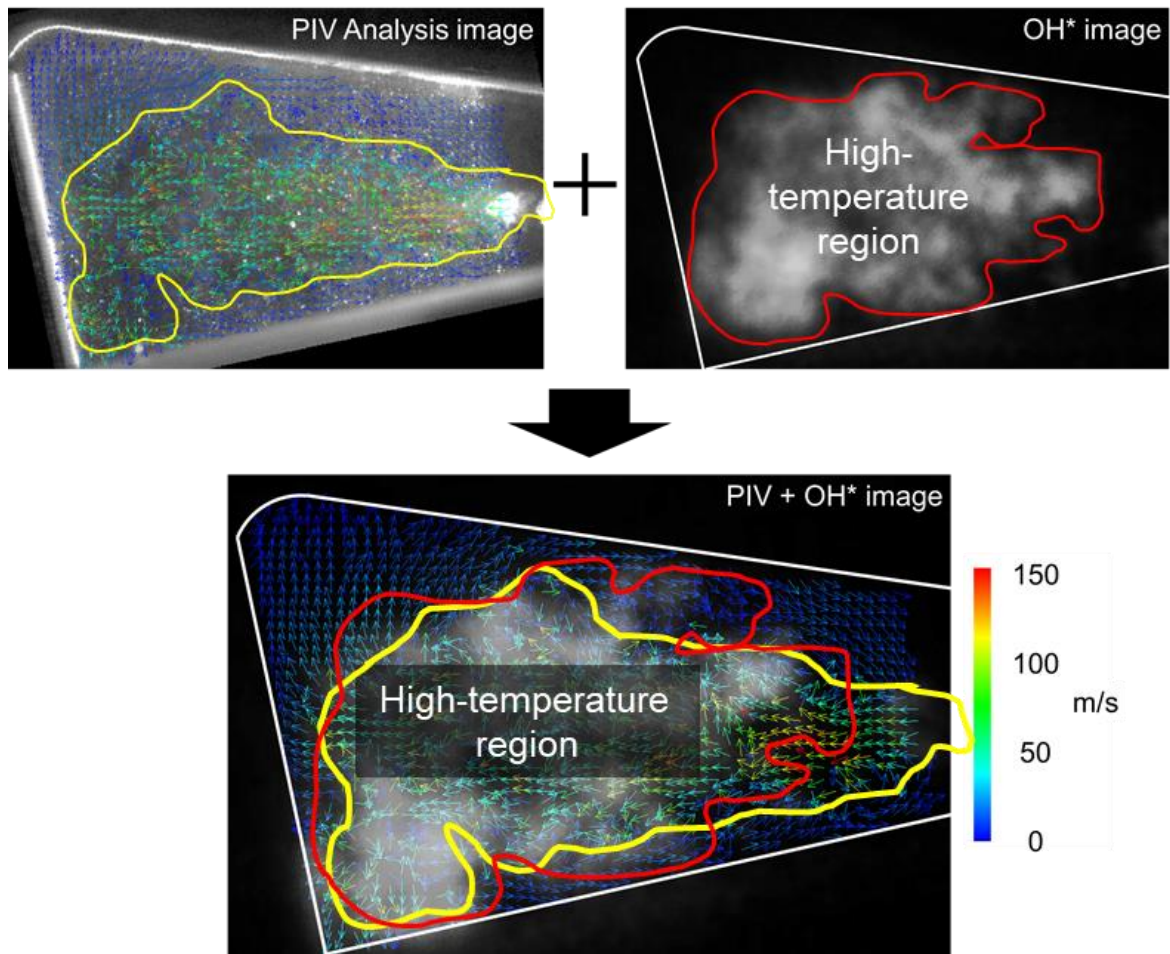


Figure 2.4 Synthesis of the PIV image and the OH* chemiluminescence image

2.3 Results and discussions

2.3.1 Relationship between high-temperature region and velocity distribution in diesel spray flame

First, the relationship between the high-temperature region and the velocity distribution was investigated to analyze the effect of flow characteristic on local heat release. The injection pressure was 120 MPa. Figure 2.5 indicates in-cylinder pressure p and heat release rate $dQ/d\theta$. Although the oxygen concentration was low, the ignition delay was brief and the heat release rate of a typical diesel combustion at high-pressure condition was shown. The mixing-controlled combustion phase started at approximately -2°CA , and $dQ/d\theta$ gradually decays after the end of combustion.

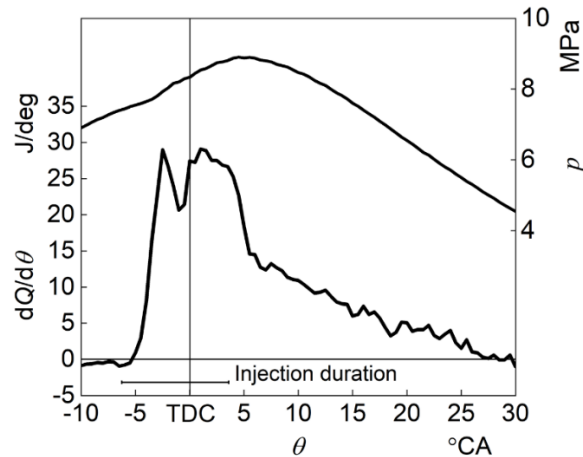


Figure 2.5 Heat release rate and in-cylinder pressure on experiment condition on 120 MPa

In order to confirm the high-temperature region in the PIV image, the PIV image was compared with the OH* chemiluminescence image captured at the same time. Figure 2.6 shows luminous flame images, a raw image for the PIV (first of the couple of images), the velocity distributions, and the OH* chemiluminescence image taken from -3.18°CA to 1.14°CA . Looking at the bottom OH* chemiluminescence images, the OH* chemiluminescence appears strongly at -2.64°CA , which corresponds to the peak timing of the heat release rate of the premixed combustion phase. During the mixing-controlled combustion phase, a high-intensity of OH* chemiluminescence region appears on the spray. A high-temperature region probably exists within this region. As the top luminous flame images demonstrate, the luminous flame began to appear at -1.56°CA and then intensified. Luminous flame hinders the PIV analysis; therefore, the strong luminous flame areas are shown as areas enclosed by red lines on the PIV raw images and in the results of the PIV analysis. Additionally, the high-intensity regions of OH* chemiluminescence are shown surrounded by orange lines on the PIV raw images and in the results of the PIV analysis. In the PIV raw images, a high-temperature region is darker than the surrounding gas regions. This means that in the high-temperature region, the fuel in the core starts to burn and the momentum to expand increases. This reduces the concentration of tracer particles for PIV and reduces the amount of light scattered by the laser. That's why the inside of a diesel spray flame appears relatively dark. Therefore, the high-temperature region can be estimated even from the relatively dark areas of the PIV raw image. The third-row images of Figure 2.6 show the results of velocity distribution. The direction of the velocity is represented by arrows, and the magnitude of the velocity is represented by the color. Up to the time when the luminous flame appeared, accurate PIV analysis was possible even in the dark region due to the high temperature. However, as expected, the accuracy of the analysis diminished in the region where the intensity of luminous flame was strong. As a result, the PIV analysis was possible in the middle of the observation area up to 1.14°CA but was difficult after that due to the strong luminous flame.

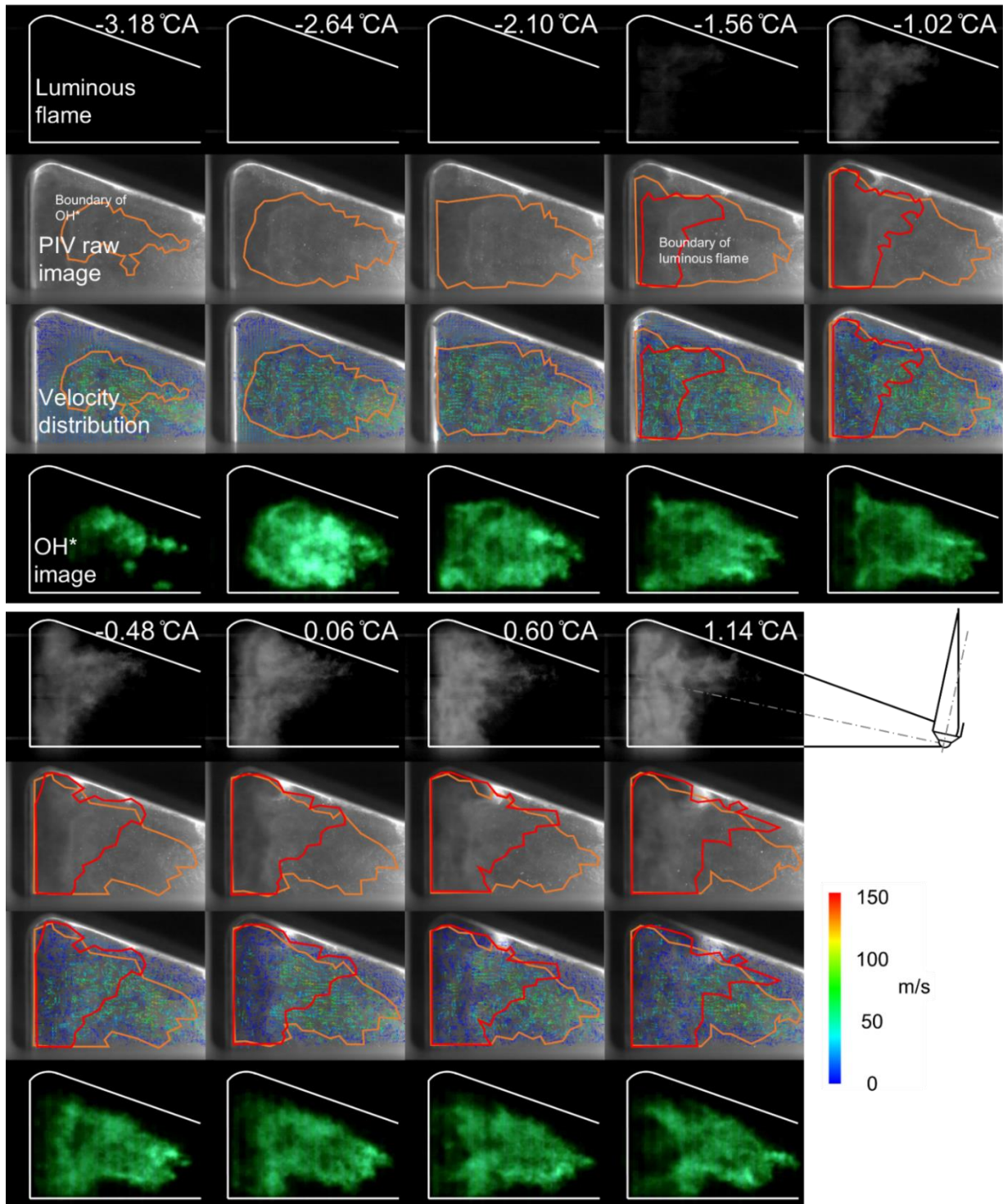


Figure 2.6 Image of luminous flame, PIV, raw image, velocity distribution, and OH* image from -3.18°CA to 1.14°CA of 120 MPa

The OH* chemiluminescence imaging and the PIV analysis were combined to determine how the high-temperature region and velocity distribution appeared in the mixing-controlled combustion period. Figure 2.7 shows the velocity distribution of each cross-section from -1.56°CA to 1.14°CA , which corresponds to the mixing-controlled combustion phase during the combustion process of one case with an injection pressure of 120 MPa. The white border in Figure 2.7 represents the shape of combustion chamber. The white clouds in the border show the OH* chemiluminescence, and the arrow represents the velocity vector of the analysis point. The magnitude of the velocity vector is indicated by color. In order to understand the velocity distribution result easily, the velocity distribution of the diesel spray flame is shown by each cross-section at equal intervals with a yellow line. The distance from the injector tip to the nearest analyzed cross-section is 20.5 mm, and the interval between each cross-section is 2 mm.

The green long dash dot line in the x -axis direction represents the spray axis, and the red line in the y -axis direction represents each cross-section that analyzed for the velocity distribution. Figure 2.7, depicts the shape of typical diesel spray seen in previous research [7], including such characteristics as the flow of the diesel spray and the surrounding air-entrained to the diesel spray. However, the velocity on the spray axis seems lower than expected. The velocity near the center of the spray may have been calculated as slower than the actual velocity because the interrogation window was determined to be suitable for the velocity range in the high temperature region. The results of the PIV analysis were compared with the pair of raw images, and any area with unreliable results is marked as an “unreliable area” in Figure 2.7. Meanwhile, the velocity distribution within some of the unreliable areas is not displayed, resulting in a discontinuous yellow line. The unreliable areas coincided well with a part of the spray center region and with the area where the luminous flame was detected as shown in Figure 2.6. Analysis of the relationship between the intensity of OH* chemiluminescence and the velocity vector in the cross-section, demonstrates that the airflow outside the high intensity region of OH* chemiluminescence is directed toward the inside of the spray. It was shown that the velocity in the high-temperature region, where the intensity of the OH* chemiluminescence is greatest, was about 20~40 m/s. Furthermore, inside the high-temperature region, the intensity of OH* chemiluminescence decreased, and the velocity increased.

As mentioned earlier, the OH* radical refers to the high-temperature region seen in stoichiometric. Therefore, through the cross section of the diesel spray flame in this study, it was found that the region where the velocity of the central axis of the diesel spray is the highest and the velocity changes greatly exists inside the high temperature region. Afterwards, it was necessary to analyze where the regions with the greatest change in velocity exist in the high-temperature regions.

150 100 50 0 m/s

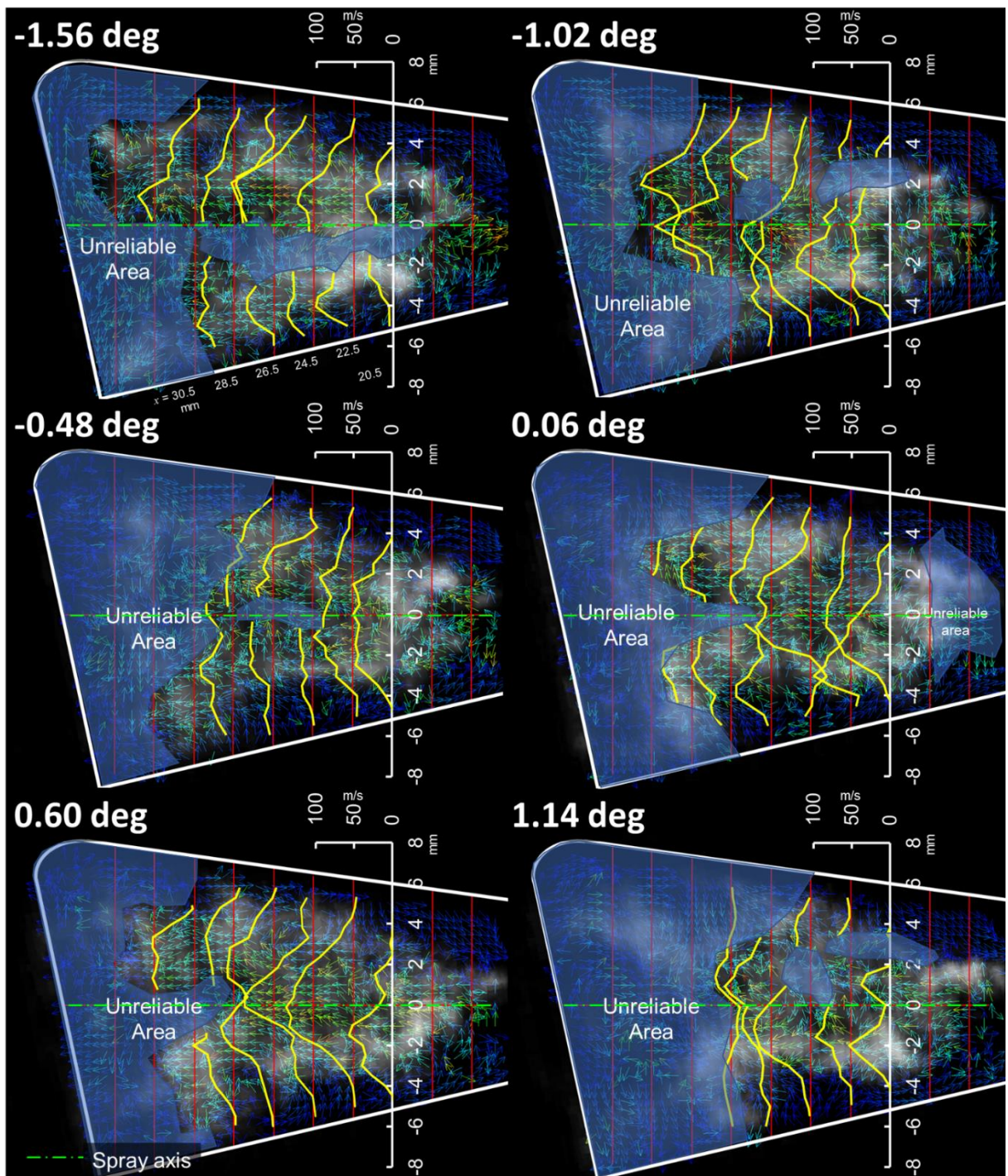


Figure 2.7 Velocity distribution of each cross-section -1.56CA to 1.14CA on a case of 120 MPa
 (Green long dash dot line: spray axis, Yellow line: velocity distribution)

Next, the relationship between the high-temperature region and the characteristics of mixing process was investigated. For this purpose, the local turbulence intensity was calculated based on the instantaneous velocity distribution and was then compared with the OH* chemiluminescence image. In order to estimate the local turbulence intensity, the fluctuation intensity, σ_r of local velocity distribution, was calculated within a certain circle area. The image on the left in Figure 2.8 shows a velocity distribution result around an example of an objective point ($x = 24.5$ mm, $y = 0$ mm). The blue, green, and orange circle on the Figure 2.8, corresponding to radii r of 0.5 mm, 1.0 mm, and 2.0 mm at objective point, respectively. The graph on the right in Figure 2.8 indicates the distribution of velocity component (u, v) within an area of each r . The u and v are the velocity vectors of the x - and y - axis directions of the diesel spray, respectively. Blue symbols are results within the circle of $r = 0.5$ mm. Green symbols are results in the region from $r = 0.5$ mm to 1 mm, and orange symbols in the region from $r = 1$ mm to 2 mm. The distribution of the absolute value of each component becomes larger as the radius increases. Based on these data, the local velocity fluctuation intensity is estimated as shown in the following Equation (2.2) through the distribution map of velocity vectors in the calculation radius.

$$\sigma_r = \sqrt{(\overline{u^2 + v^2}) - (\bar{u}^2 + \bar{v}^2)} \quad (2.2)$$

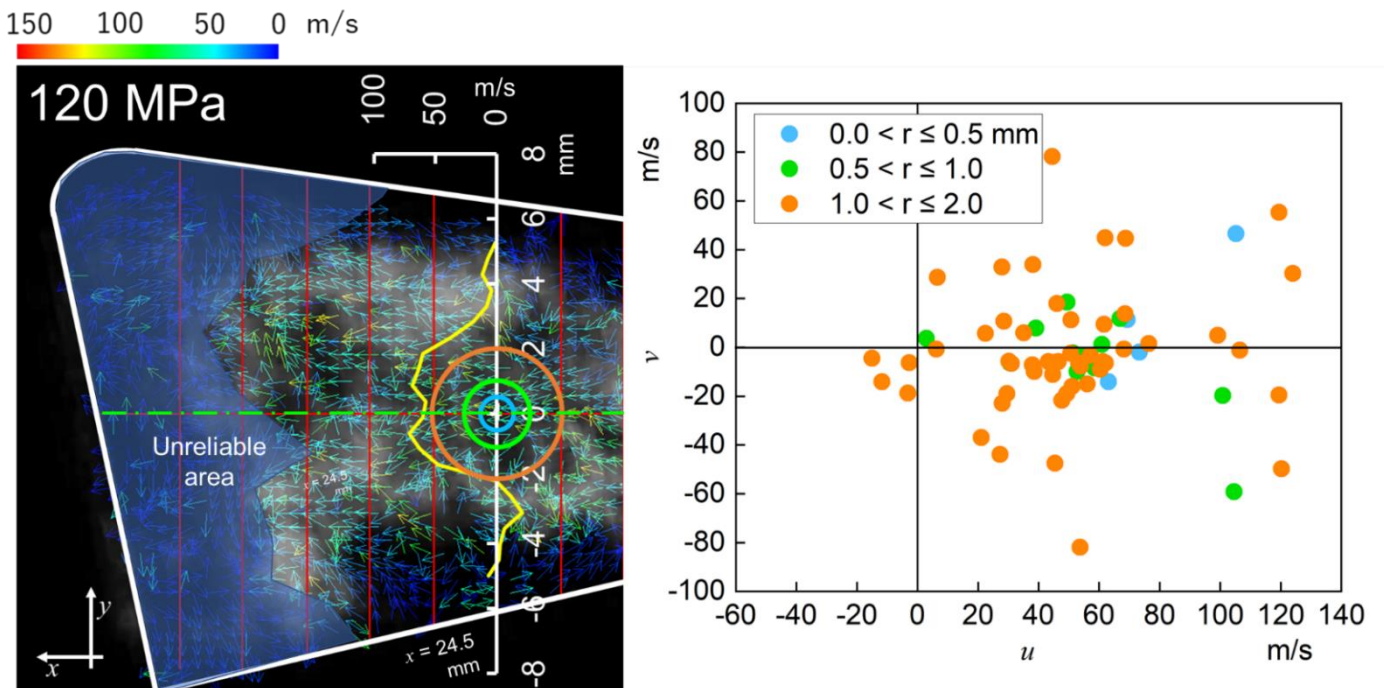


Figure 2.8 Estimation of local velocity fluctuation intensity
 (Left: velocity distribution of a cross-section ($x = 24.5$ mm) and an objective point,
 Right: distribution of velocity vectors within a region)

Using Equation (2.2), a change of the velocity fluctuation intensity compared to the radius around a point ($x = 24.5 \text{ mm}$, $y = 0 \text{ mm}$) is shown in Figure 2.9. The x -axis of the graph represents the range of the calculated radius, r , and the y -axis represents the calculation result of the local velocity fluctuation intensity, σ_r . As the radius increases, the local velocity fluctuation intensity also increases. However, the local velocity fluctuation intensity did not change significantly beyond a certain radius, i.e., above $r = 0.75 \text{ mm}$.

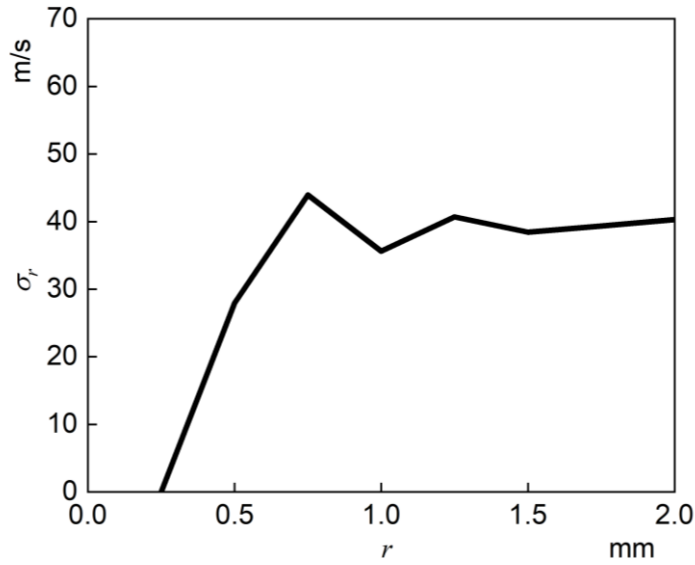


Figure 2.9 Velocity fluctuation intensity value on vector point $x = 24.5 \text{ mm}$, $y = 0 \text{ mm}$

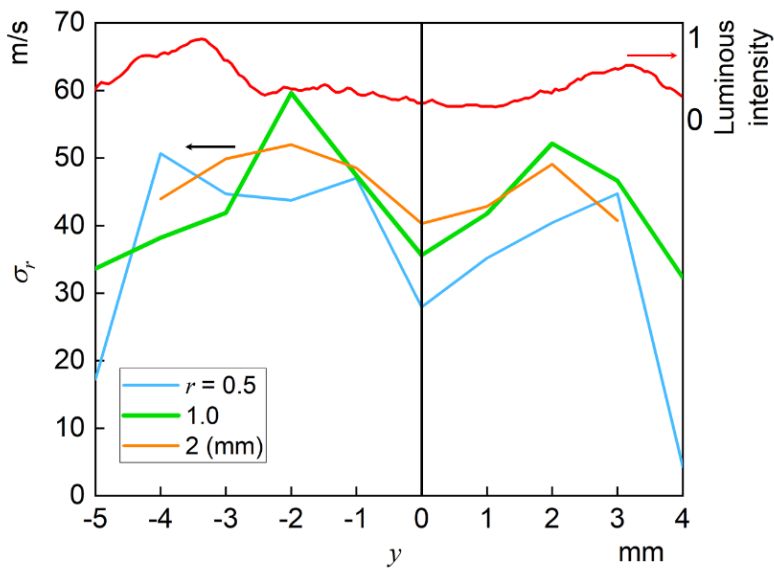


Figure 2.10 Velocity fluctuation intensity on cross-section $x = 24.5 \text{ mm}$

The distribution of velocity fluctuation intensity in a cross-section ($x = 24.5$ mm) result with the luminous intensity of OH* are shown in Figure 2.10. The x -axis shows the distance from the spray axis. The left and right sides of the vertical axis represent the local velocity fluctuation intensity and the OH* luminous intensity, respectively. For all conditions of radius, r , the tendency of velocity fluctuation intensity σ_r of the cross section did not change significantly. However, σ_r reaches its local maximum around $y = \pm 2$ mm, which is located slightly inside the high-temperature region. Comparing this result with the velocity distribution result, reveals that the local maximum of σ_r corresponds to the place where the velocity changes rapidly at the highest value of the velocity fluctuation intensity. The observed velocity fluctuation intensity was similar to the turbulence intensity in the diesel spray discussed in the previous study of Kobashi et al. [7]. Here, the local fluctuation intensity of velocity could represent the characteristics of the turbulence intensity. The maximum value of the luminous intensity which is the boundary of the high-temperature region is located about 3~4 mm from the center of the spray. A comparison between the velocity fluctuation intensity and the luminous intensity in the graph, reveals that the maximum value of the velocity fluctuation intensity was located slightly inside the boundary of the high-temperature region. In this experiment, the thickness of the strong OH* luminous intensity was about 2 mm. Thus, in order to investigate the relationship between the boundary of the high-temperature region and the local velocity fluctuation intensity, the calculation radius, r , was set to 1 mm. The result made it possible to analyze the velocity distribution and the turbulence intensity of the diesel spray flame along with the overlapped images of the PIV result and OH* chemiluminescence in the RCEM, to simulate actual engine conditions.

2.3.2 Effect of injection pressure on velocity distribution and velocity fluctuation intensity in diesel spray flame

In this section, the experiment results when the injection pressure was set at 60 MPa, 90 MPa, and 120 MPa are compared, in order to find out how the velocity distribution and the turbulence intensity of the high-temperature region appeared according to the injection pressure. Figure 2.11 shows the heat release rate when the injection pressure is at 60 MPa, 90 MPa, and 120 MPa. At 60 MPa and 90 MPa, the start of injection was equal to -6.4°CA , which is the same as when the injection pressure is 120 MPa. Therefore, to inject the same amount of fuel, the end of injection was 5.4°CA at 90 MPa and 8.2°CA at 60 MPa. The peak values of the heat release rate at 60 MPa and 90 MPa are both lower than its peak value at 120 MPa.

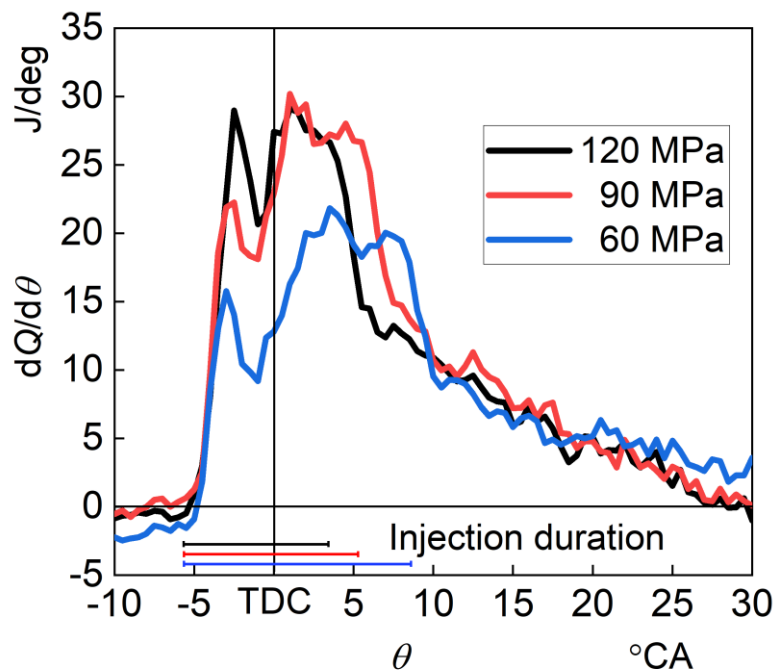


Figure 2.11 Comparing the heat release rate at 120 MPa, 90 MPa, and 60 MPa

To investigate the effect of injection pressure on velocity distribution and the high-temperature region, the PIV and OH* chemiluminescence images at different injection pressure was analyzed. Figure 2.12 shows the result of the velocity distribution at 60 MPa, 90 MPa, and 120 MPa. The image was captured during the mixing-controlled combustion phase at a moment of 0.06°CA. The reason why the moment of 0.06°CA selected was that the luminous flame spreads more widely in the combustion chamber after 0.06°CA, which makes it difficult to analyze the PIV result. The velocity at the center of the spray axis was the largest, and the velocity decreased away from the center of the spray axis. This phenomenon appears in the velocity distribution of a typical diesel spray flame, where the velocity of the spray decreases as the velocity field widens downstream of the diesel spray flame. The difference in the velocity distribution of the diesel spray flame according to the injection pressure was also appeared. When the injection pressure is lowered, the difference in velocity between cross-sections decreases as its distance from the injector tip increases. However, the region where the luminous intensity of OH* chemiluminescence is strong was not significantly affected by the injection pressure.

Next, to find out how the high-temperature region and the turbulence intensity appear when the injection pressure is different, the velocity fluctuation intensity was calculated from the result of the velocity distribution of each cross-section at the same moment and was compared with the intensity of the OH* chemiluminescence. Figure 2.13 shows the velocity distribution image and the velocity fluctuation intensity at different injection pressure.

150 100 50 0 m/s

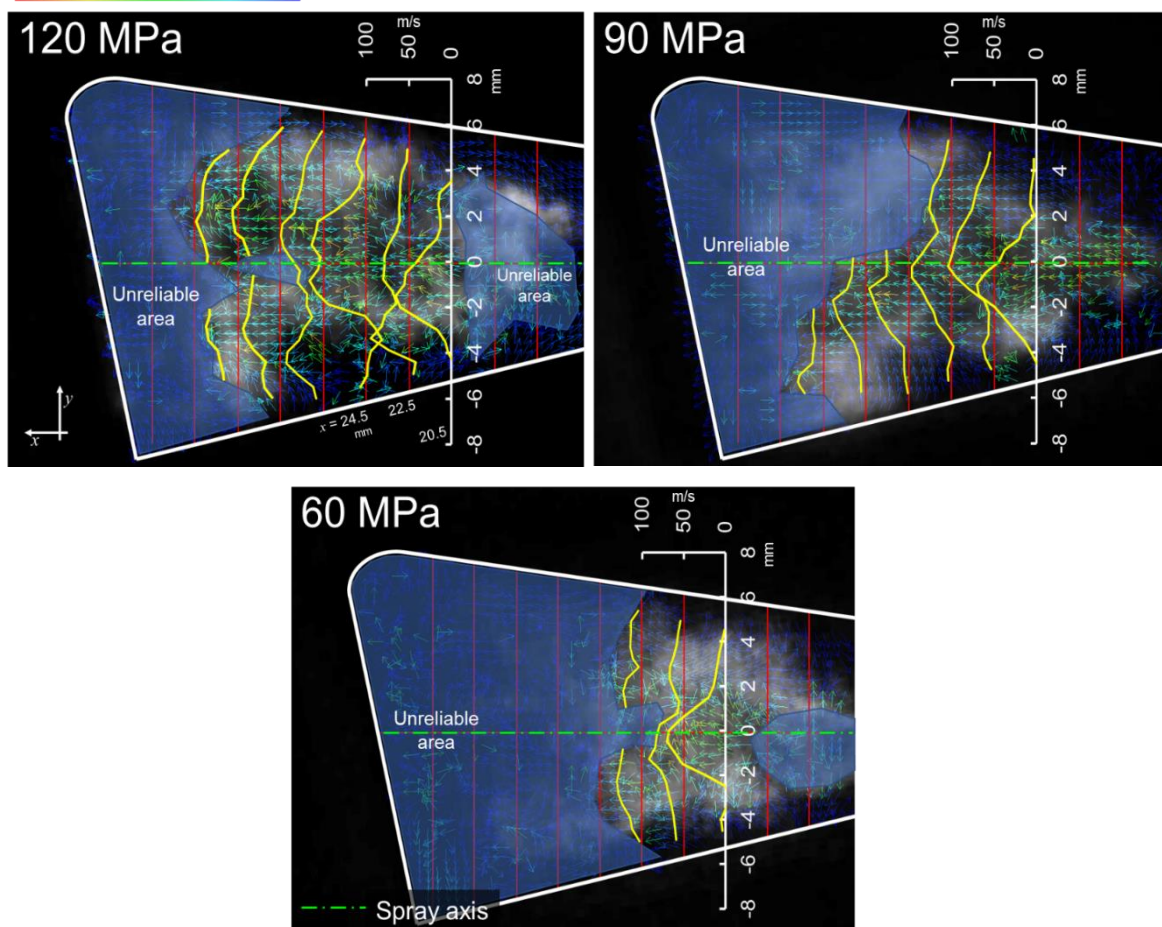


Figure 2.12 Analyzing velocity distribution result of 120 MPa, 90 MPa and 60 MPa at 0.06°CA

Figure 2.13 shows the velocity distribution of the cross section that analyzed the local velocity fluctuation intensity. The graph below shows the local velocity fluctuation intensity in the cross section. The calculation radius is the same as $r = 1$ mm. The x -axis of the graph represents the distance from the spray axis, and the left and right sides of the vertical axis represent the local velocity fluctuation intensity and the OH* chemiluminescence intensity, respectively. Each cross-section shows the result of $x = 24.5$ mm when the injection pressure is 120 MPa and 90 MPa. At $x = 24.5$ mm of 60 MPa, since the reliability of the PIV analysis result is so low, the cross-section where can measure the local velocity fluctuation intensity ($x = 20.5$ mm) was analyzed. As a result, even though the injection pressure was different, the position of maximum peak value of the velocity fluctuation intensity was slightly inside the maximum value of the OH* chemiluminescence intensity, which corresponds to the boundary of the high-temperature region. Furthermore, as the injection pressure decreases, the velocity fluctuation intensity decreases. The velocity fluctuation intensity of the injection pressure at 60 MPa

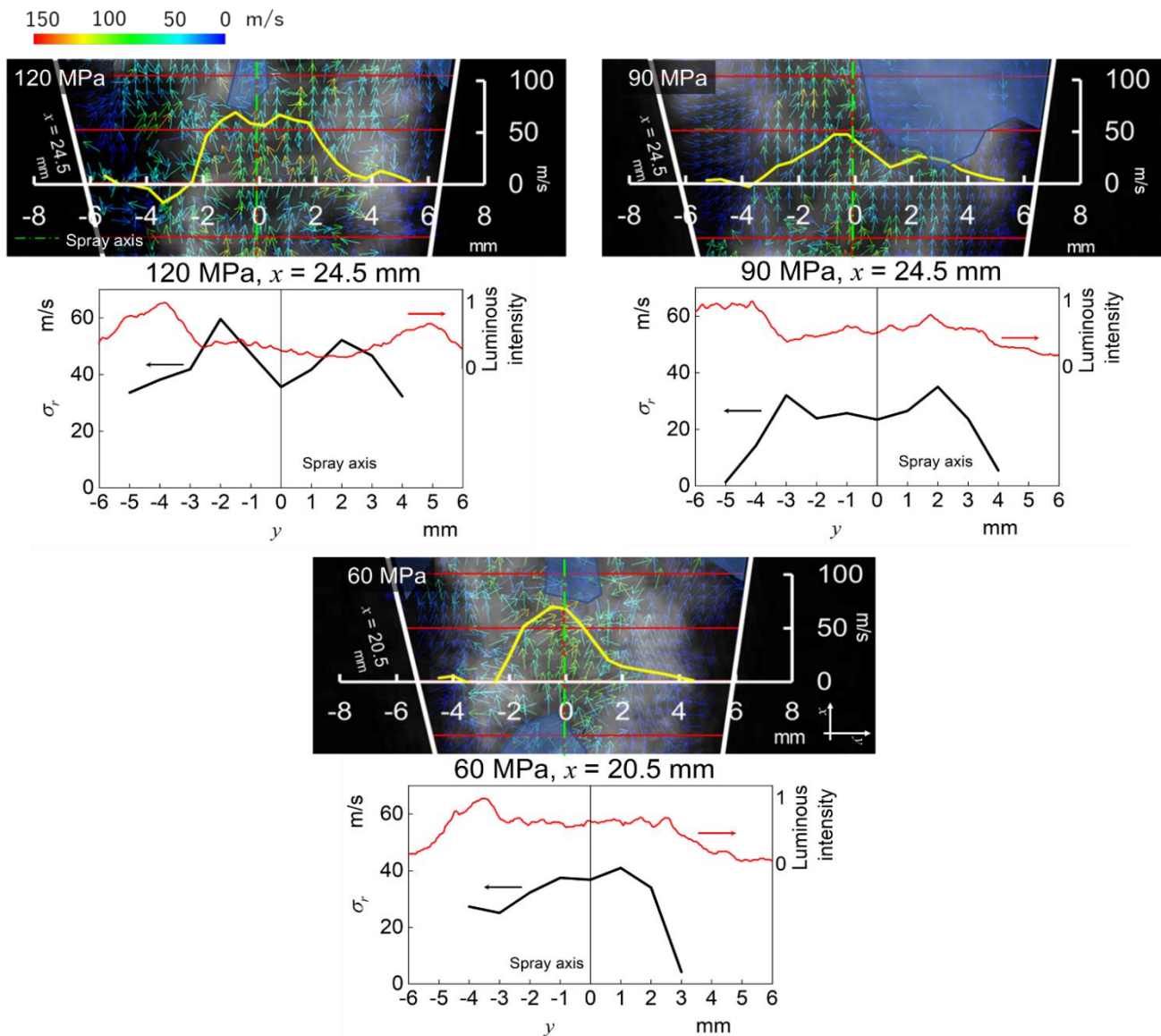


Figure 2.13 Analyzing velocity fluctuation intensity result of 120 MPa, 90 MPa, and 60 MPa ($r = 1.0 \text{ mm}$)

is similar with 90 MPa because the cross-section of 60 MPa is located closer to the injector tip than the cross-section of 90 MPa. Thus, when the injection pressure is low in the same cross-section, it is possible to assume that the turbulent intensity is decreased by the decrease of the velocity fluctuation intensity. Through the experimental results, the characteristic of velocity distribution, velocity fluctuation intensity, and high-temperature region in a diesel spray flame as shown in Figure 2.14 can be constructed. The shape of the diesel spray flame could be estimated from the OH* chemiluminescence image and the PIV result. The surrounding air of the diesel spray flame showed a like the black arrow flow in Figure 2.14. The overall flow direction of the surrounding air is backward

flow. As can be shown from the image, the maximum value of the turbulence intensity slightly inside the boundary of the high-temperature region and then decreased again at the center of the diesel spray axis. And, it was found that as the injection pressure decreased, the maximum value of the turbulence intensity decreased.

Based on these results, it was newly found that, after a strong mixture of fuel and air is formed in a region with high turbulence intensity, the region where the stoichiometric is formed is slightly pushed outward due to the diffusion phenomenon as combustion starts. And, through these research, it was found that the injection pressure affects the turbulence intensity of the diesel spray flame, and it can also affect the local heat release rate. This suggests that increasing the injection pressure can increase the local heat release rate due to the high turbulence intensity inside the diesel spray flame.

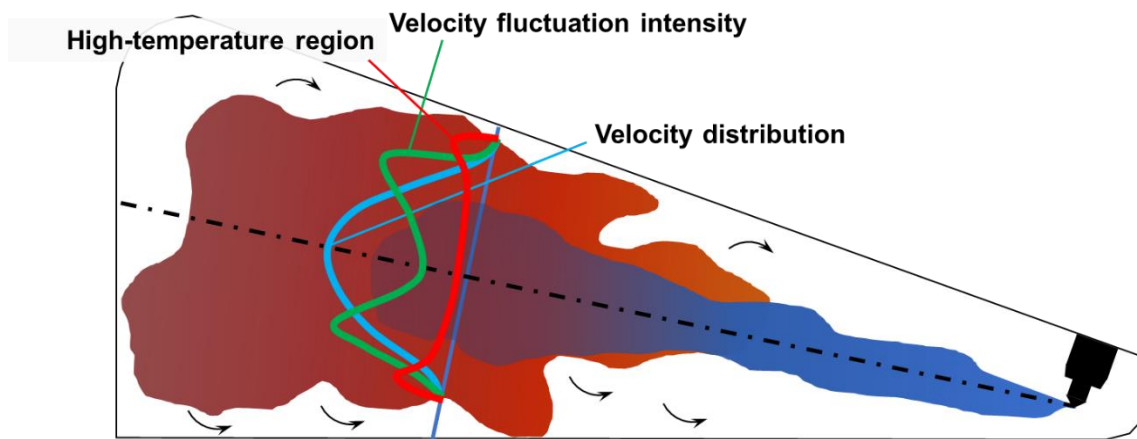


Figure 2.14 Structure of the diesel spray flame through the velocity distribution, velocity fluctuation intensity and high-temperature region

2.4 Summary

The aim of this study was to reveal the velocity distribution and the high-temperature region in the diesel spray flame. For this purpose, an image taken simultaneously by the PIV and the OH* chemiluminescence methods were compared in a visualization using an RCEM. The region where the OH* chemiluminescence appears in the combustion process was overlapped with the PIV analysis image in order to analyze the relationship between a high-temperature region and the velocity distribution. In addition, the local velocity fluctuation intensity was calculated and analyzed for the turbulence intensity characteristics inside the high-temperature region. Based on these results, the following conclusions were reached.

1. In the PIV analysis, the result shows that the flow of the diesel spray and the surrounding air entrained to the diesel spray flame in the RCEM. Thus, it was found that the PIV result of the RCEM can measure the velocity distribution of a diesel spray in a realistic engine situation.
2. To investigate the mixing process inside the high-temperature region of the diesel spray flame, a method of calculating the velocity fluctuation intensity was used. When comparing the velocity fluctuation intensity and the intensity of the OH* chemiluminescence, which shows the high-temperature region, it was found that the maximum of the turbulence intensity appears slightly inside of the high-temperature region.
3. As the injection pressure increased, the velocity of the diesel spray increased. However, the high-temperature region was not strongly affected by the injection pressure.
4. Even if the injection pressure was changed, the position of the maximum velocity fluctuation intensity was slightly inside of the high-temperature region. As the injection pressure decreased, the maximum velocity fluctuation intensity decreased. It was found that the injection pressure affects the turbulence intensity of the diesel spray flame.

Through these results, it was newly found that, after a strong mixture of fuel and air is formed in a region with high turbulence intensity, the region where the stoichiometric is formed is slightly pushed outward due to the diffusion phenomenon as combustion starts. So, the discrepancy between the high-temperature region and the region with high intensity of velocity fluctuation was confirmed. Although, it is well known that increasing the injection pressure is effective in shortening the combustion duration by shortening the fuel injection duration, it got clear that the relationship between the high-temperature region and the high turbulence region remains unchanged. For further understanding, it would be necessary to investigate the effects of nozzle diameter, ambient pressure, and ambient oxygen concentration. Also, to clarify the spray structure using oxygenated fuels and ducted fuel injection in order to actively modify the relationship between velocity distributions and local equivalent ratio in the spray flame.

Representative nomenclature

θ : Crank angle

$dQ/d\theta$: Heat release rate

p : In-cylinder pressure

u : Velocity of parallel direction with diesel spray axis

v : Velocity of vertical direction with diesel spray axis

r : Radius of velocity components

σ_r : Fluctuation intensity

x : Position of parallel direction with diesel spray axial

y : Position of vertical direction with diesel spray axial

References

- [1]. Funayama, Y., Nakajima, H. and Shimokawa, K., "A Study on the Effects of a Higher Compression Ratio in the Combustion Chamber on Diesel Engine Performance," SAE Technical Paper 2016-01-0722, 2016, doi:10.4271/2016-01-0722.
- [2]. Kimura, S., Matsui, Y., and Itoh, T., "Effects of Combustion Chamber Insulation on the Heat Rejection and Thermal Efficiency of Diesel Engines," SAE Technical Paper 920543, 1992, <https://doi.org/10.4271/920543>.
- [3]. Shudo, T., Nabetani, S., Nakajima, Y., "Analysis of the degree of constant volume and cooling loss in a spark ignition engine fuelled with hydrogen", SAGE journal Volume: 2 issue: 1, page(s): 81-92 Issue published: February 1, 2001, <https://doi.org/10.1243/1468087011545361>
- [4]. Kojima, H., Kawanabe, H., Ishiyama, T., and Furutani, H., "LES Analysis of Fuel/Air Mixing and Heat Release Processes in a Diesel Spray", SAE Technical Paper 2013-01-2537, 2013, <https://doi.org/10.4271/2013-01-2537>.
- [5]. Khalid, A., Yatsufusa, T., Miyamoto, T., Kawakami, J., Kidoguchi, Y., "Analysis of Relation between Mixture Formation during Ignition Delay Period and Burning Process in Diesel Combustion", Small Engine Technology Conference & Exposition, 2009-32-0018
- [6]. Cao, Z., Nishino, K., Mizuno, S. et al., "PIV measurement of internal structure of diesel fuel spray," Experiments in Fluids 29, S211–S219, 2000, doi:10.1007/s003480070023
- [7]. Kobashi, Y., Yokogawa, K., Miyabe, H., Hase, R., Kato, S., "Flow fields and turbulent characteristics in non-evaporating diesel sprays", Atomization and Sprays, Volume 28, 2018 issue 8, doi:10.1615/AtomizSpr.2018026468
- [8]. Zama, Y., Ochiai, W., Sugawara, K., Furuhashi, T., and Arai, M., "Study on Mixing Process of Diesel Spray under High Ambient Gas Density Condition," Atomization Sprays, vol. 23, no. 5, pp. 443–461, 2013. DOI: 10.1615/AtomizSpr.2013007347
- [9]. Kojima, H., Kawanabe, H., Ishiyama, T., "A study on mixture formation process in a diesel spray using a PLIF method", THIESEL 2010 Conference on Thermo- and Fluid Dynamic Processes in Diesel Engines
- [10]. Bruneux, G., "Liquid and vapor spray structure in high-pressure common rail diesel injection", Atomization and Sprays, Volume 11, 2001 issue 5, page 24, doi: 10.1615/AtomizSpr.v11.i5.40

- [11]. Bruneaux, G., "Mixing Process in High Pressure Diesel Jets by Normalized Laser Induced Exciplex Fluorescence Part I: Free Jet," SAE Technical Paper 2005-01-2100, 2005, <https://doi.org/10.4271/2005-01-2100>
- [12]. Bottone, F., Kronenburg, A., Gosman, D. et al. The Numerical Simulation of Diesel Spray Combustion with LES-CMC. *Flow Turbulence Combust* 89, 651–673 (2012). <https://doi.org/10.1007/s10494-012-9415-y>.

Chapter 3. Characteristics of the diesel spray flame in various condition with different jet-jet angle

3.1 Introduction

Diesel engine plays an important role in the transportation sector, especially in heavy-duty (HD) vehicles. The thermal efficiency of the diesel engine has increased significantly, and the harmful emissions have improved considerably, through the advancement of diesel engine technology [1]. Currently, alternative power sources for decarbonized society are being developed [2], but they are still far from ready for HD vehicle application. Therefore, higher thermal efficiency is needed. In particular, increased supercharging, high compression ratio, and high torque at low speed are mainstream strategies used to increase thermal efficiency in HD diesel engines [3, 4]. To achieve higher torque, the fuel injection amount per cycle needs to increase. However, when the fuel injection duration lengthens to increase the injection amount, the combustion duration also lengthens, and the degree of constant volume decreases, deteriorating thermal efficiency. To shorten the combustion duration, the fuel injection duration must be shortened. This can be achieved by increasing the fuel injection pressure and/or the fuel flow rate by increasing the number or diameter of the nozzle holes [5]. However, since the maximum injection pressure of current commercial injection devices has reached 250 MPa, increasing the injection pressure even more is a challenge. In addition, many studies show that the large nozzle hole leads to the negative effects on smoke emissions [6-10]. Therefore, increasing the number of nozzle holes is the remaining option to reduce the injection duration. However, diesel engine developers have observed that smoke emissions increase when the number of nozzle holes exceeds a certain limit. For example, Horibe et al. [11] showed the effect of the number of nozzle holes with the constant fuel flow rate on engine performance emissions. The smoke emission decreased as the number of nozzle holes was changed from six to eight, while smoke emission increased with a 10-hole nozzle. The cause is likely due to the interference between adjacent sprays.

There have been some studies on the effect of jet-jet interaction between adjacent sprays on the combustion process. Chartier et al. [12] investigated the influence of jet-jet interaction on the “lift-off length,” which was introduced by Higgins and Siebers [13], in a Bowditch-design optical engine using symmetrical and asymmetrical nozzles with four nozzle holes. The angle between the objective spray and the adjacent sprays was 45°, 90°, or 135°. The inter-jet spacing became smaller, and the lift-off length was shortened, as the jet-jet angle decreased. Toda et al. [14] analyzed the surrounding airflow of the diesel spray. The inter-jet air-flow with a multi-hole nozzle has a stronger backward velocity component (toward the nozzle) compared to the single-hole nozzle. Also, Fuyuto et al. [15, 16] clarified the mechanism of backward flow and investigated the effect of injection pressure and nozzle hole diameter on lift-off length using a single-hole nozzle with a fan-shaped chamber, which restricted

the air entrainment without having adjacent sprays. Bazyn et al. [17] investigated the lift-off and liquid length by a multi-hole nozzle in a high-pressure continuous flow chamber, in which the number of nozzle holes was varied between 6 and 18. A significant shortening of the lift-off length was found as the number of nozzle holes increased. However, few studies have been performed to investigate the lift-off and liquid length with a multi-hole nozzle under engine condition with a realistic piston cavity. When the number of nozzle holes is changed under such a condition, it is difficult to investigate only the effect of the number of nozzle holes, because the difference in the injection rate causes the difference in-cylinder pressure and heat release rate and affects the combustion.

Therefore, in this study, we aimed to isolate the effect of the number of nozzle hole on the diesel combustion phenomena with narrow jet-jet angles and elucidate the relationship between lift-off length and liquid length under realistic diesel engine conditions. For the purpose, a series of experiments was carried out using an optical accessible rapid compression and expansion machine (RCEM) equipped with a custom-made asymmetric six-hole nozzle having jet-jet angles α of 30° and 45°. The RCEM has a realistic piston cavity and it is possible to investigate the influence of the number of nozzle hole (jet-jet angle) in the same macroscopic in-cylinder pressure and heat release histories. High-speed direct photo imaging with the Mie scattering method and high-speed OH* chemiluminescence imaging were applied to capture the evolution of the spray flame, characterized by lift-off length and liquid length. In addition, using the PIV method, when the jet-jet angle is 30° and 45°, the flow velocity between the jets was measured, and the flow characteristics were investigated in the backward direction of the spray and injected into the spray according to the jet-jet angle.

3.2 Experimental setup

3.2.1 *Experimental apparatus*

The experimental apparatus consisted of an RCEM, a fuel injection system, a control unit, and an intake and exhaust system as shown in Figure 3.1. The specification of RCEM is summarized in Table 3.1. The bore and stroke were 110 and 106 mm, respectively, the compression ratio was 12.3, and the displacement was 1 L. The swirl ratio of this RCEM was almost 0, and this RCEM examined only the single-injection case. The cylinder head has two optical windows. One pneumatic valve for intake and exhaust was installed on the cylinder liner to secure window space on the cylinder head, which resulted in a relatively low compression ratio.

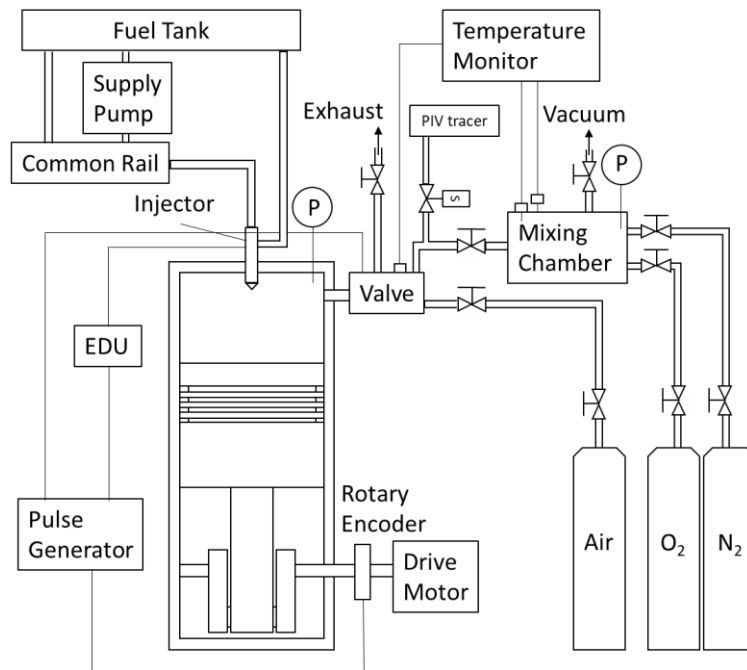


Figure 3.1 Schematic of the RCEM

Table 3.1 Specification of the RCEM

Bore × Stroke	85 mm × 96 mm
Displacement	$1.007 \times 10^{-3} \text{ m}^3$
Compression ratio	12.3
Valve system	Pneumatic 1 valve
Injection system	Common rail system with piezoelectric drive injector

Figure 3.2 shows the piston shape, spray direction, and optical area. The piston cavity was a step-lip type with an inner diameter of 61 mm and an outer diameter of 76 mm. The cylinder head had two optical windows made of quartz. The diameter of the optical area was 42 mm, and the window field limit was 3.5 mm away from the injector because of manufacturing limits. The asymmetric injector had six holes with an included angle of 155° . Three holes had a jet-jet angle of 30° , corresponding to a 12-hole nozzle, and the other side had a jet-jet angle of 45° , corresponding to an 8-hole nozzle. The reason that this injector was specially manufactured for this study is to reduce the variables of the temperature and pressure change characteristics inside the combustion chamber that can occur when the jet-jet angle of the injector is changed during the combustion process.

Here $dQ/d\theta$, γ , p , V , θ are the apparent heat release rate, the ratio of specific heats, the in-cylinder pressure, the in-cylinder volume, and the crank angle, respectively. A constant value of $\gamma = 1.33$ was used.

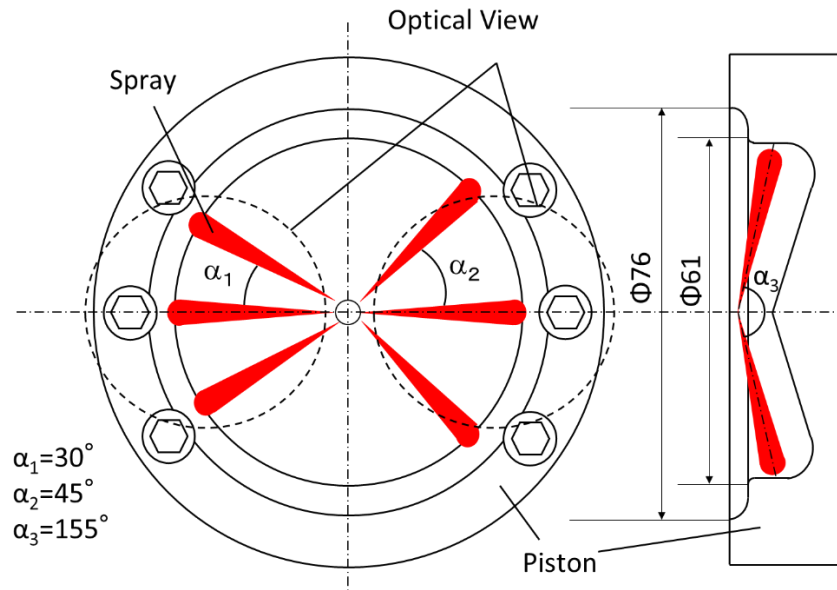


Figure 3.2 Schematic of the injector and optical access

At the start of the experiment, the intake valve was closed, and the mixing chamber and its pipeline to the intake valve were evacuated by a vacuum pump. The mixing chamber was then filled with high-pressure gas consisting of nitrogen and oxygen. The intake valve was opened, and the motor started to drive the machine. Gases contained in the mixing chamber flowed in and out of the cylinder through the intake valve, and the temperature increased. When the intake gas temperature reached a particular level, the valve was closed, and one compression stroke began. The fuel was then injected at the specified injection timing.

Table 3.2 Experimental condition

Cranking speed	1200 rpm
Fuel	JIS No.2 Diesel fuel
Injection quantity	27.1 mg
Start of Injection (SOI)	-5° ATDC
In-cylinder pressure @ SOI	6.1 MPa
In-cylinder temperature @ SOI	780 K
Injection pressure	120, 80 MPa
Jet-jet angle	30° (12-hole injector), 45° (8-hole injector)
Nozzle hole diameter	0.126 mm, 0.100 mm
Oxygen concentration	19%, 15%

The basic experimental conditions are shown in Table 3.2. The engine speed was 1200 rpm. The fuel amount was 27.1 mg, which was 4.52 mg/hole in each hole. The injection timing was set to -5° ATDC. The in-cylinder pressure and temperature at the injection timing were 6.1 MPa and 780 K, respectively. This condition achieved a short ignition delay, although the temperature was lower than that of a typical diesel engine owing to the low compression ratio. The standard conditions for injection pressure, nozzle hole diameter, and oxygen concentration were 120 MPa, 0.126 mm, and 19%, respectively. The injection pressure, injector nozzle hole diameter, and oxygen concentration were varied during the tests. The nozzle hole was straight, with the nozzle sack diameter being a function of the nozzle hole diameter. For nozzle hole diameter of 0.126 mm and 0.100 mm, the sac diameters were 1.0 and 0.9 mm, respectively. Therefore, the injection hole length depends on the injection hole diameter.

3.2.2 Imaging technique for OH^* chemiluminescence and direct imaging

The schematic of the optical setup is shown in Figure 3.3 and the imaging condition is summarized in Table 3.3. Two kinds of imaging techniques were applied. One was direct imaging to catch the spray and the luminous flame. When performing direct imaging, a 532 nm laser expanded through a cylindrical lens was irradiated to the middle of the three sprays, and a Mie scattering of droplets in the spray was measured to determine the liquid length as shown in Figure 3.4. In this study, since an asymmetric injector with different jet-jet angles was specially manufactured. So, the liquid length and lift-off length of the central spray were measured to accurately analyze the influence of adjacent sprays among the three spray jets. The other imaging technique was OH^* chemiluminescence imaging used to capture the high-temperature region near the combustion. The wavelength value of OH^* was filtered in flames using a band-pass filter of 310 ± 10 nm. An image intensifier was used to increase the intensity value. The lift-off length was measured based on the OH^* chemiluminescence imaging.

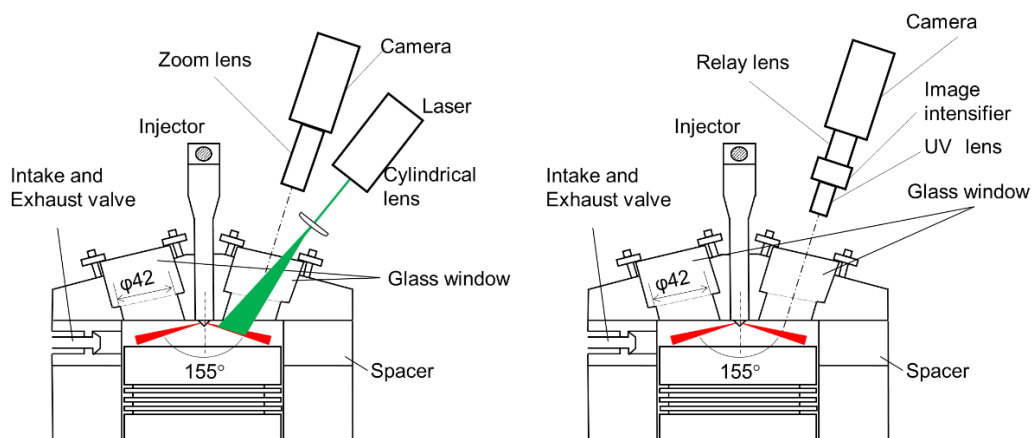


Figure 3.3 Schematic of the optical set up for direct imaging (a) and OH^* chemiluminescence (b)

Table 3.3 Imaging condition

Target	Luminous flame	OH* chemiluminescence
Camera	Photron Fastcam SA-Z	
Optical filter	-	Bandpass filter 310 ± 10 nm
Image intensifier	-	Used (Gain: 650)
Frame rate	48,000 Hz	
Image resolution	896×472 ($43.3 \mu\text{m}/\text{pixel}$)	
Exposure	$0.16 \mu\text{s}$	$0.6 \mu\text{s}$

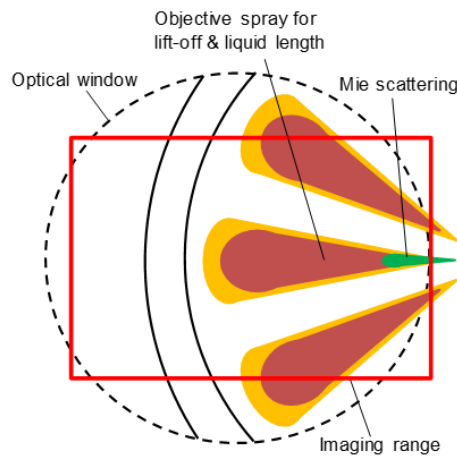


Figure 3.4 Image range of OH* chemiluminescence and direct imaging

The liquid length and lift-off length were measured for the middle of three sprays on the images. As shown in Figure 3.5(a), the liquid length was determined based on the intensity of the green color of the direct imaging. The liquid length is important to provide an insight on the relationship between the fuel vaporization and combustion. To distinguish the spray from the flame, the area where the green RGB value was sufficiently stronger than the red RGB value was defined as the spray area, and the farthest part from the injector was determined as the liquid length. As shown in Figure 3.5(b), lift-off length was analyzed by images measured through the OH* chemiluminescence method. The flame lift-off affects in diesel combustion and emission processes where the fuel and air premix prior to reaching the initial combustion zone. And, OH* radical is a known for marker of stoichiometric, which the location of a high-temperature region. So, lift-off length is important to know where the combustion and emission is initiated. After measuring the intensity in whole objective (middle) spray, the distance to half of the first appearing peak was determined as the lift-off length, since the thick flame impinging onto the piston wall emitted more intense chemiluminescence, thereby disturbing the detection of lift-off length. The frame rates of both methods were 48,000 Hz. For each jet-jet angle of 30° and 45° , direct imaging and OH* chemiluminescence imaging were performed six times under all conditions.

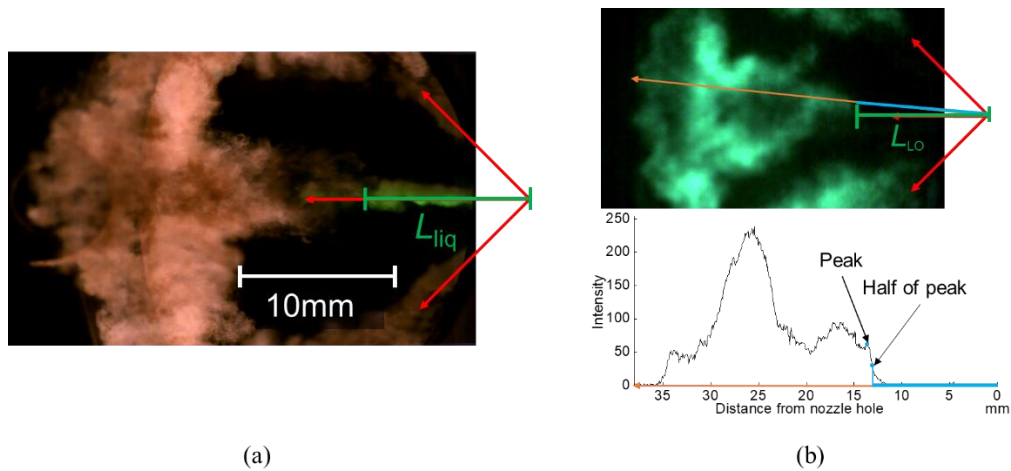


Figure 3.5 Image analysis method of liquid length (a) and lift-off length (b)

3.2.3 Experimental setup for PIV

In this study, the particle image velocimetry (PIV) was performed to measure the flow velocity inside the combustion chamber. The PIV is a technology that simultaneously analyzes the velocity and direction of flow through a flow field visualized by tracer.

The measuring method of the PIV is as follows. The sheet form of a laser is incident on the flow field mixed with the tracer, and the position change of the tracers existing in the two-dimensional flow field within the cross-section of the laser sheet is continuously imaged through the high-speed camera. Through this, a vector map of the flow field can be created by calculating the position change and time interval of tracers through images take at short time intervals.

The experiment was conducted in the following order. The air, which include the tracer, was introduced into the intake pipe at 1 MPa through the solenoid valve between the pipe from the premixing tank to the combustion chamber. Through this, it was possible to introduce the tracer into the combustion chamber without affecting the combustion experiment during the intake stroke of the RCEM.

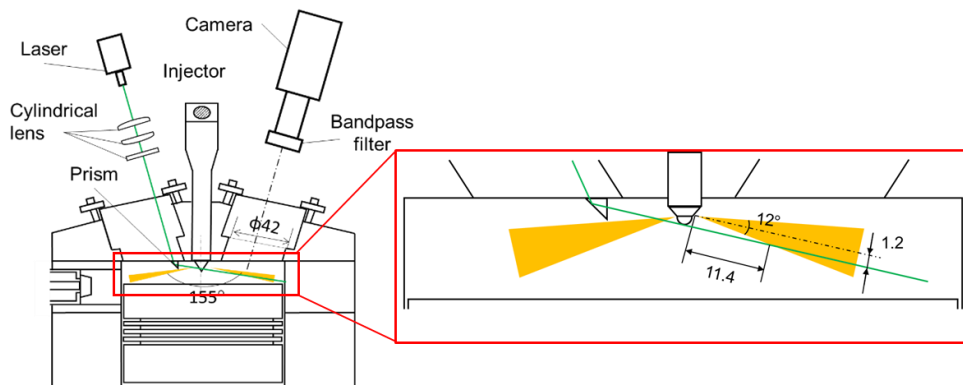


Figure 3.6 Schematic of the optical set up and position of the laser sheet for PIV

A schematic diagram of the equipment for laser incidence inside the combustion chamber for PIV is shown in Figure 3.6. For the laser, a green color high-power laser (Civil Laser PSU-W-LED 10 W) with a wavelength of 532 nm was used, and a cylindrical lens was used to form a sheet. For this study, a prism was attached to a window glass mounted on a cylinder head to penetrate the laser sheet between the spray jets so that the laser sheet could be reflected inside the combustion chamber and penetrate the diesel spray. As shown in the enlarged image of Figure 3.6, a prism is installed at the position where the laser is incident from the window glass attached to the cylinder head. The laser sheet reflected by the prism was made incident along the diesel spray axis. Scattering light from the tracer by the laser sheet, and it was imaged with a high-speed camera equipped with a 532 nm bandpass filter. However, the laser sheet could not completely penetrate the center of the diesel spray axis due to the layout characteristics of the experimental device. So, as shown in Figure 3.6, the laser sheet was incident under 1.2 mm parallel to the diesel sprat axis. Assuming that the spray angle of the diesel spray is 12° , the diesel spray first contacts the laser sheet at a distance of 11.4 mm from the injector tip.

The ambient flow field of a diesel spray is influenced not only by the adjacent diesel spray but also by the piston wall [18]. Therefore, the positional relationship between the laser sheet and the adjacent diesel spray and piston wall was evaluated in the following way, and it is shown in Figure 3.7. First, make a drawing of the position of the laser sheet, diesel spray, and piston wall. Then, based on the drawing, a plane was cut perpendicular to the spray axis of the target diesel spray at distance of 9, 13, and 17 mm from the injector tip and a cross-section was made. The positional relationship between the laser sheet, diesel spray, and piston wall can be obtained through the cross-section.

Figure 3.7 shows the results according to the distance and jet-jet angle of the section away from the injector tip through the above process.

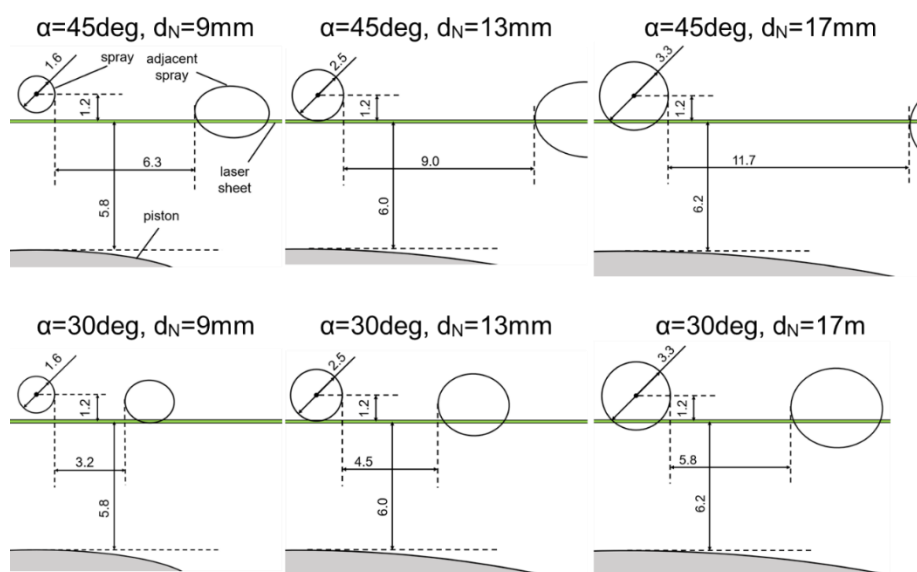


Figure 3.7 Positional relationship between laser sheet and diesel spray

Looking at the Figure 3.7, it can be seen that from the jet-jet angle of 45°, the distance between the diesel spray and the laser sheet is sufficiently close from 9 mm from the tip of the injector to the analysis of the flow field. Likewise, when the jet-jet angle is 30°, the distance between the diesel spray and the laser sheet from around 9 mm from the injector tip is close that can be analyzed.

Table 3.4 Experiment condition for the PIV experiment

Cranking speed	1200 rpm	
Injection quantity	27 mg	
Injection pressure	120 MPa	
Start of injection (SOI)	-5°CA	
In-cylinder pressure @ SOI	6.0 MPa	
Intake temperature	393 K	
Jet-jet angle	30°, 45°	
Injector nozzle diameter	0.100 mm	
Pre-mixture composition	Combustion N ₂ = 41 mol% Ar = 40 mol% O ₂ = 19 mol%	Non-combustion N ₂ = 100 mol%
PIV tracer	Goddball E-90C (SiO ₂): 10 μm	

Table 3.4 shows the experimental conditions in the PIV experiment. Most of the experimental conditions are the same as for lift-off length and liquid length. The cranking speed is 1200 rpm, the fuel injection amount is 27 mg, the fuel injection timing is -5°CA, and the in-cylinder pressure at the fuel injection is 6.0 MPa. The difference is that an injector with a diameter of 0.100 mm is used, and the compression ratio of the premixed air during combustion is 41 mol% of N₂, 40 mol% of Ar, and 19 mol% of O₂. The reason for this is to increase the fuel injection duration when injecting the same amount of the fuel and use Ar to decrease the ignition delay to increase the quasi-steady period of the injection rate, thereby increasing the visible time period of the flow.

Table 3.5 PIV imaging conditions and analysis method

Camera	Photoron Fastcam SA-Z
Frame rate	48,000 Hz
Image resolution	512 × 512 (48 μm/pixel)
Exposure	19.23 μs
Analysis algorithm	Multiple-pass interrogation
Number of iterations	10
Template size	16 × 16
Overlap	50%

The image conditions are shown in the following Table 3.5. A high-speed camera (Photron Fastcam SA-Z) was used for imaging. The frame rate is 48,000 Hz, the resolution is 512×512 , the spatial resolution is $48 \mu\text{m}/\text{pixel}$, and the exposure time is $19.23 \mu\text{s}$. Table 3.5 shows the PIV analysis conditions for images taken with a high-speed camera. Multiple-pass interrogation was selected as the analysis algorithm, and the number of iterations was set to 10. The size of the template was 16×16 pixels, and the overlap was 50%.

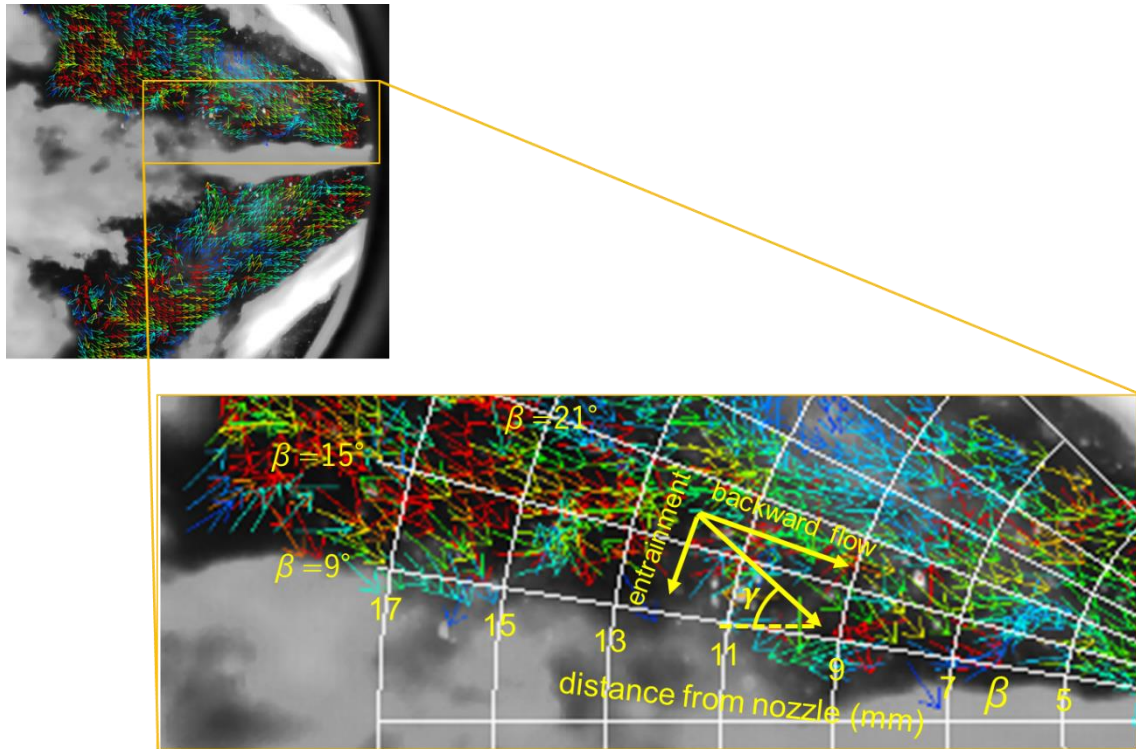


Figure 3.8 Velocity vector map and the calculated area from the captured PIV image

Figure 3.8 shows the velocity vector map of the flow using PIV from the captured image. The image on the upper left is a velocity vector map made by the PIV method for the entire imaged part, and the image in which the concentrated part is highlighted with a yellow rectangle to analyze the flow phenomenon with the adjacent spray is shown as the lower right. Using the distance from the injector tip, d_N , and the angle β from the main diesel spray axis, the polar coordinates were used to calculate the vector of the area between the sprays. The range of the cell to be distinguished was set at 2 mm intervals of $d_N = 9, 11, 13, 15,$ and, 17 mm and 6° intervals with angles $\beta = 9, 15,$ and 21° . The average value of the velocity vectors in the divided cells is calculated, and the calculated velocity vectors are divided into the back-flow direction and the entrainment direction based on the target diesel spray. The backward flow velocity and the entrainment velocity were calculated and analyzed based on the angle γ between the velocity vector of each cell and the target spray axis.

For PIV analysis, each condition was experimented with 15 times, and the results were analyzed.

Figure 3.9 shows the angle, γ , between the velocity vector and the diesel spray axis in a cell with distances from the injector tip of $d_N = 13$ to 15 mm and 15 to 17 mm, and an angle $\beta = 9$ to 15° . The horizontal axis of the graph on the left shows the time, and the vertical axis shows the angle, γ , between the velocity vector and the diesel spray axis. The dotted line on the graph indicates when fuel injection started. The points on the graph show the values calculated with the cell average vector, and the error values are expressed as thin range lines. If you look at the error range, it shows that it is quite large at the moment the injection starts, and then gradually decreases as the injection continues. It showed a random flow of air inside of the combustion chamber before injection started. However, this is because the flow between sprays flows in the direction of the injector tip after the injection starts. Therefore, it was judged that it was possible to analyze the results of this PIV results by averaging data based on the non-random observation of the flow direction after the start of injection.

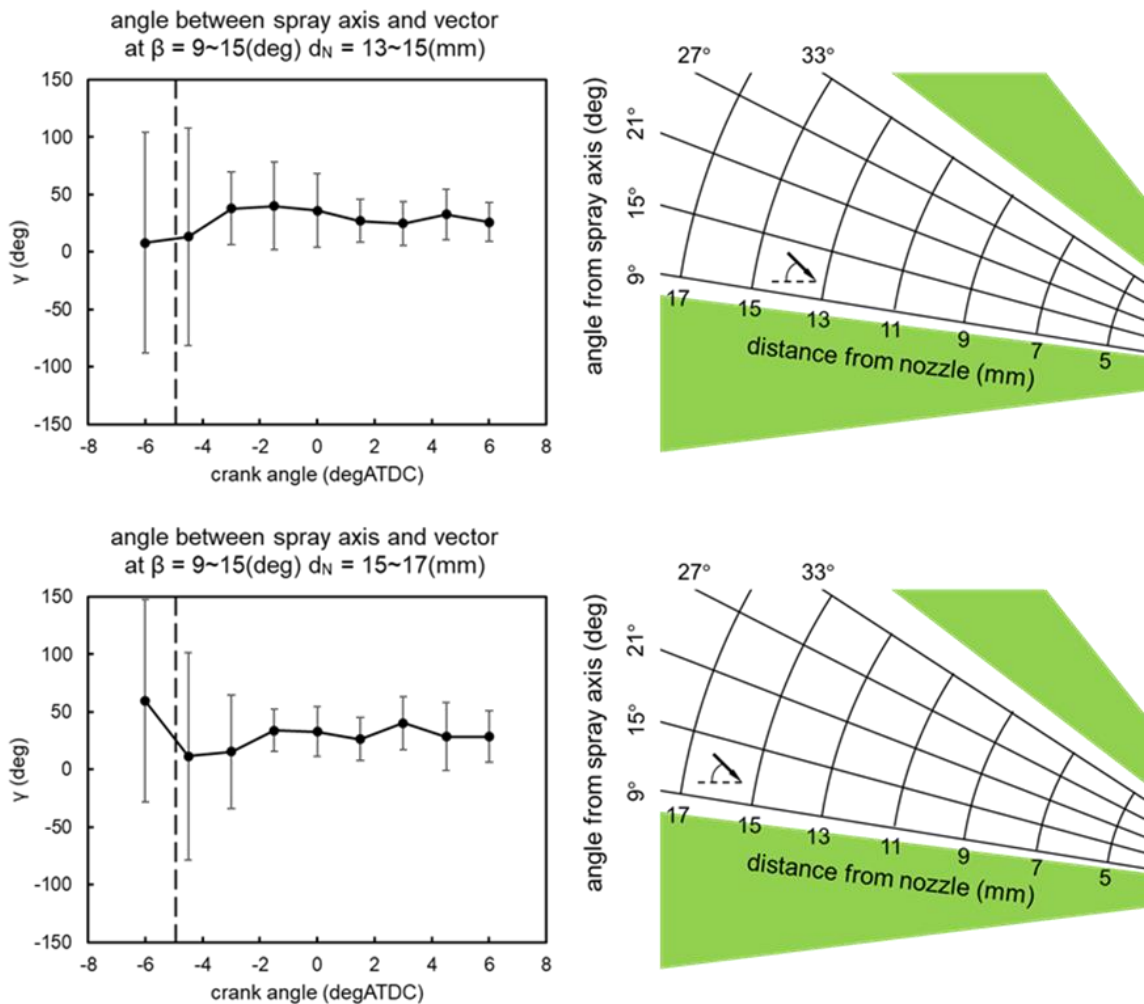


Figure 3.9 Average angle and margin of error between the diesel spray axis and the velocity vector over time in the calculation domain.

3.3 Results and discussions

3.3.1 Effect of jet-jet angle

First, the effect of the jet-jet angle on the combustion process was investigated under the standard condition, i.e., the injection timing of -5°ATDC , $p_{\text{inj}} = 120\text{ MPa}$, $d_N = 0.126\text{ mm}$, and $r_{\text{O}_2} = 19\%$. The experiments were performed 24 times, including the jet-jet angle α of 30° and 45° for both imaging methods, with no significant difference in the heat release rates. Figure 3.10 indicates the representative in-cylinder pressure p , heat release rate $dQ/d\theta$, and injection duration against crank angle θ . The ignition occurs at around -2°ATDC , and the mixing-controlled combustion phase is shown.

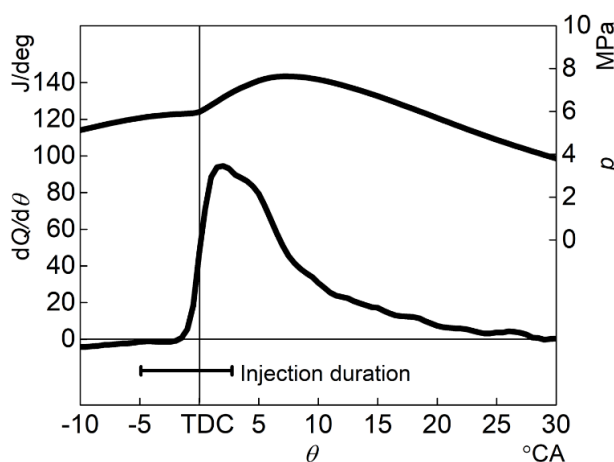


Figure 3.10 Heat release rate and in-cylinder pressure under the standard condition ($r_{\text{O}_2} = 19\%$, $p_{\text{inj}} = 120\text{ MPa}$, and $d_N = 0.126\text{ mm}$)

Figure 3.11 shows the sequence images of the direct imaging of $\alpha = 30^\circ$ and 45° . The red arrow indicates the injection direction. The two thin lines on the left side of each image correspond to the edge of the piston cavity, and the thick line on the right side of each image corresponds to the window edge. The bright green area shows the dense spray area by Mie scattering. The spray grew to the steady condition at -1.5°ATDC , and then the spray shortened after 1.5°ATDC because when the ignition occurred at around -2°ATDC , as shown in Figure 3.11. The luminous flame appeared at TDC, impinged onto the piston wall, and then spread toward the nozzle. The smaller jet-jet angle narrowed the inter-jet spacing.

Figure 3.12 shows the OH^* chemiluminescence of $\alpha = 30^\circ$ and 45° . The OH^* area seems roughly similar to the luminous flame area of Figure 3.12; however, the appearance of OH^* occurs earlier than that of the luminous flame. Also, the combustion area can be detected without being disturbed by the scattered light from the spray.

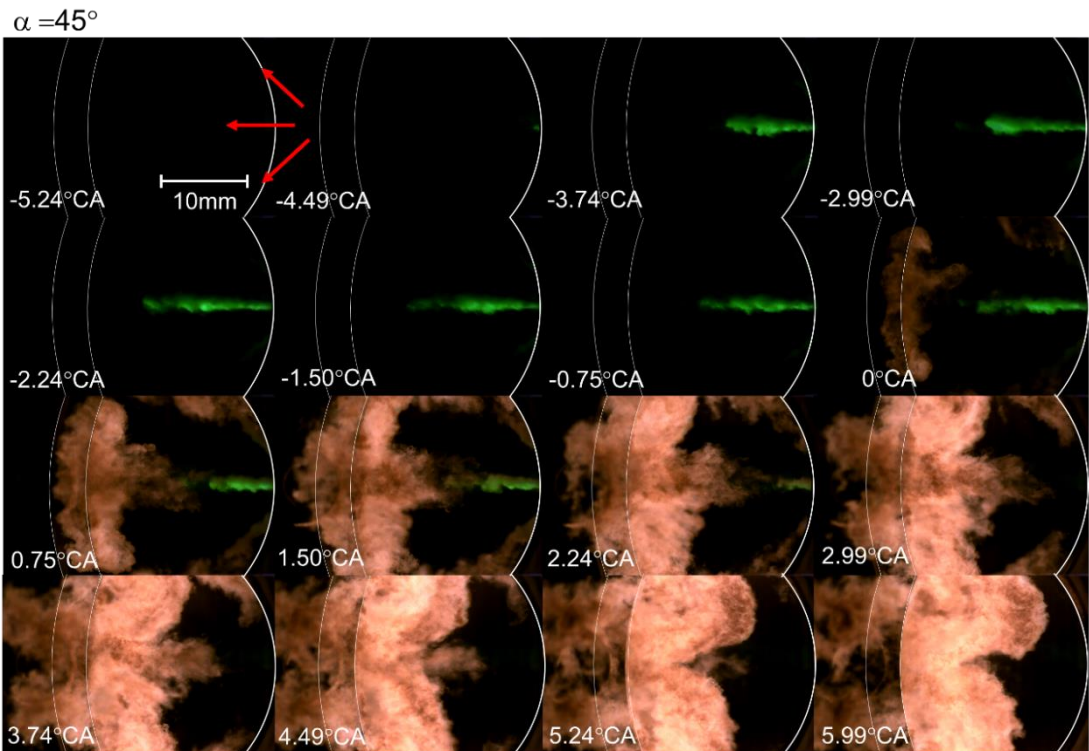
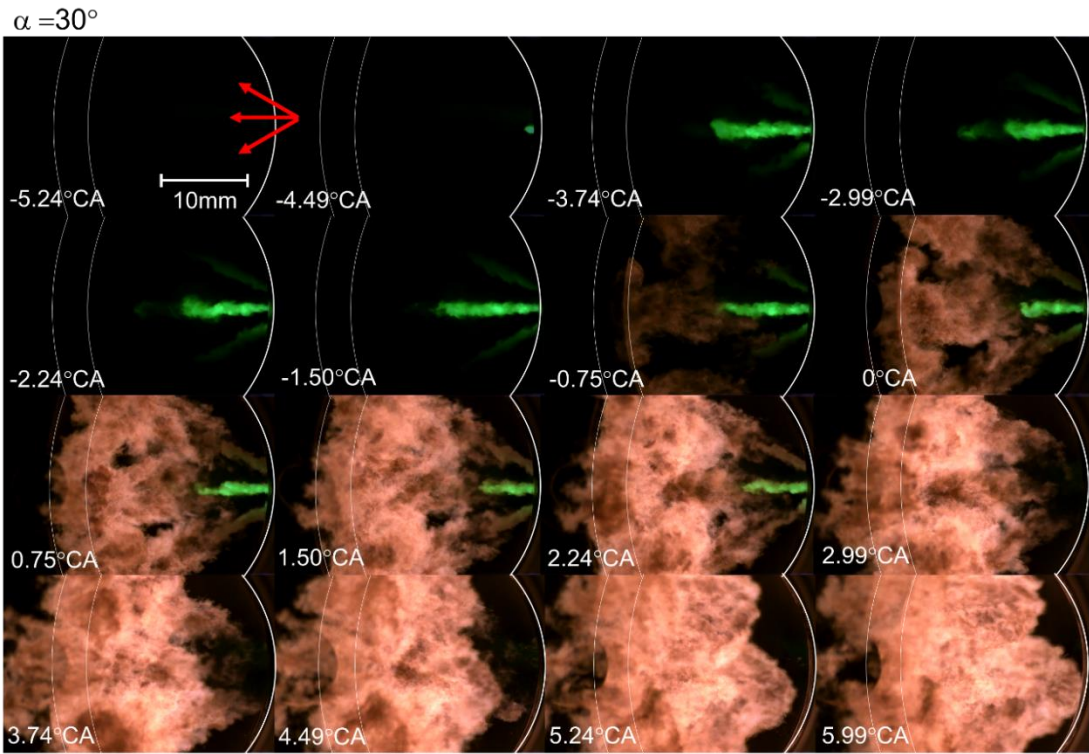


Figure 3.11 Image of direct imaging at different jet-jet angle ($\alpha = 30^\circ$ and 45°) under the standard condition ($r_{O_2} = 19\%$, $p_{inj} = 120$ MPa, and $d_N = 0.126$ mm)

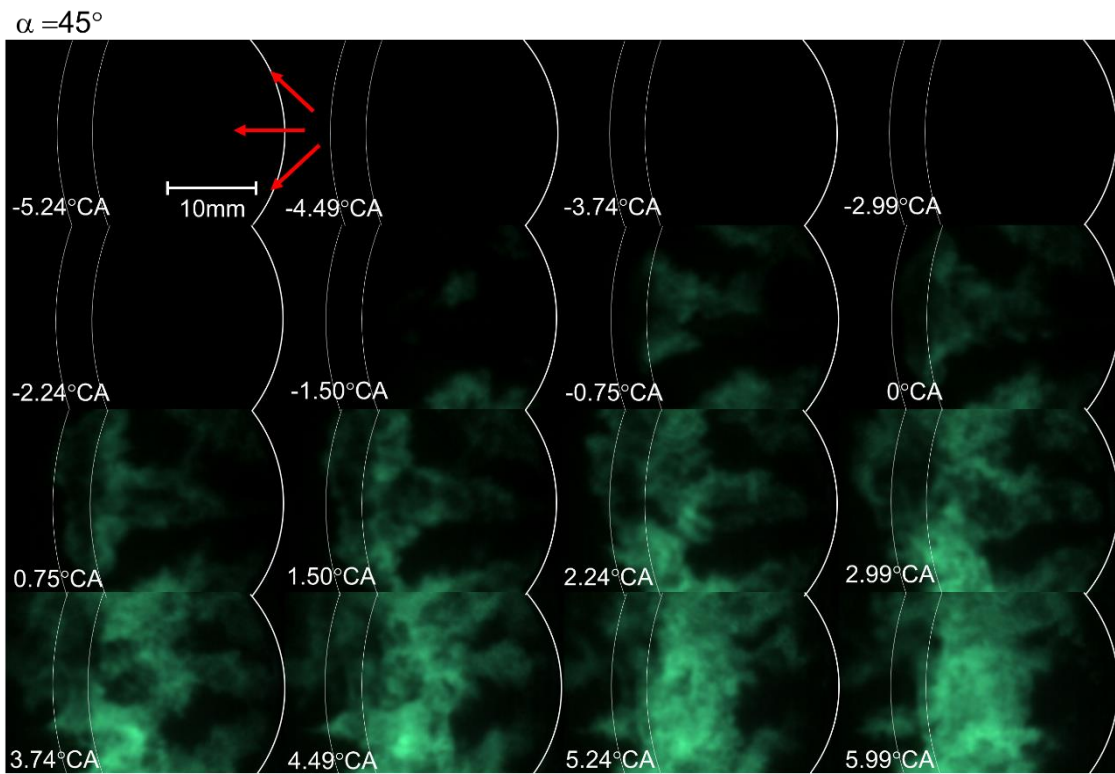
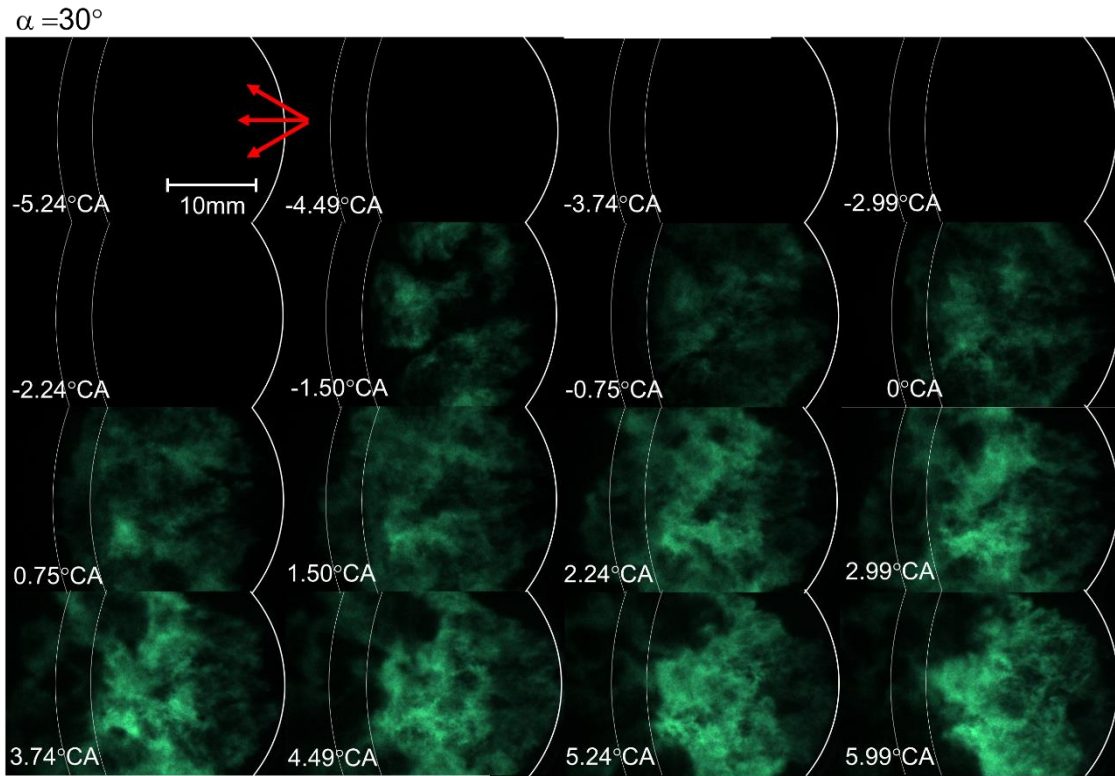


Figure 3.12 Image of OH* chemiluminescence at different jet-jet angle ($\alpha = 30^\circ$ and 45°) under the standard condition ($r_{O_2} = 19\%$, $p_{inj} = 120$ MPa, and $d_N = 0.126$ mm)

To determine the effect of the jet-jet angle on the liquid and lift-off length, the direct imaging and OH* imaging was analyzed. Figure 3.13 shows the liquid length, L_L , and lift-off length, L_{LO} , according to the jet-jet angle α . The plots are the average of six experimental results. Before the ignition at -2°ATDC , the liquid length of each jet-jet angle was nearly equal. The lift-off length of each jet-jet angle at the ignition timing of -2°ATDC were nearly equal as well. However, the behavior of the liquid and lift-off length after the ignition differed between the different jet-jet angles. In the case of $\alpha = 45^\circ$, the initial liquid and lift-off length were constant and then slowly decreased. However, the liquid and lift-off length of $\alpha = 30^\circ$ leveled off near TDC and then rapidly decreased. Subsequently, the liquid length decreased at the end of injection. The liquid and lift-off length decrease similarly just after the ignition.

The main reason for this should be entrainment into the hot-burned gas, which the backward flow by the adjacent diesel spray flame, was strong in small jet-jet angle case. And also, it seems that the lift-off length changed according to the change of the liquid length. This indicates that a backflow approaching the nozzle tip or thermal radiation from an adjacent spray flame enhanced the evaporation of the spray under analysis.

To determine why liquid and lift-off length shorten with the narrower jet-jet angle, the relationship between them under various conditions was examined in more detail. The effects of injection pressure and nozzle hole diameter, which influence the atomization of the spray, and oxygen concentration, which influences the temperature of entrained gas, were investigated in the following sections.

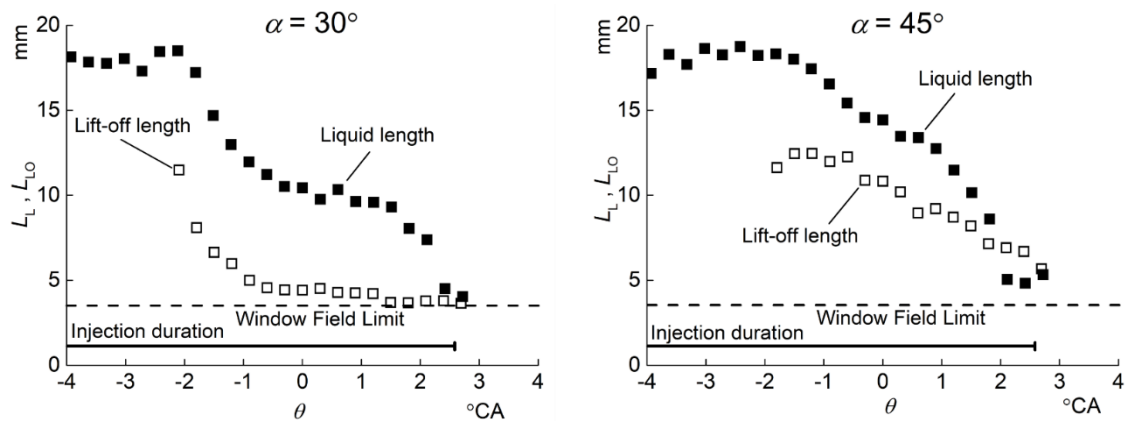


Figure 3.13 Lift-off length and liquid length at different jet-jet angle ($\alpha = 30^\circ$ and 45°) under the condition of $r_{O_2} = 19\%$, $p_{inj} = 120$ MPa, and $d_N = 0.126$ mm

3.3.2 Effect of injection conditions in different jet-jet angle

In this section, the effect of the jet-jet angle on the combustion process with an injection pressure of 80 MPa and then with a nozzle hole diameter of 0.100 mm. The results were compared to those under the standard conditions in the previous section.

First, the injection pressure p_{inj} of 80 MPa was applied to isolate the effect of injection pressure, with $d_N = 0.126$ mm and $r_{O_2} = 19\%$. Figure 3.14 indicates the representative in-cylinder pressure p , heat release rate $dQ/d\theta$, and injection duration. The ignition delay was not significantly affected, but the maximum heat release rate decreased, and the combustion duration lengthened, owing to the low injection pressure and long injection duration.

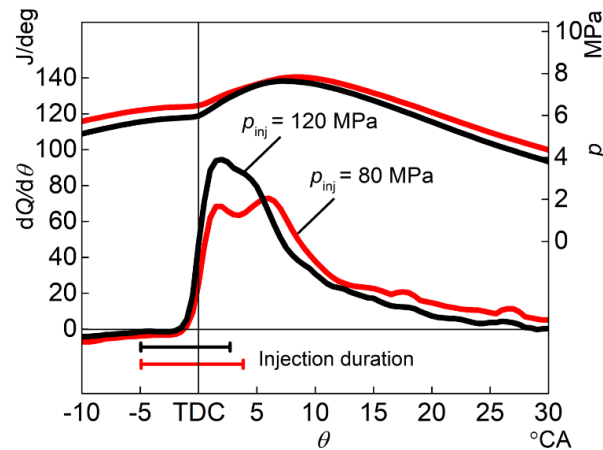


Figure 3.14 Heat release rate and in-cylinder pressure at different injection pressure ($p_{inj} = 120, 80$ MPa) under the condition of $r_{O_2} = 19\%$ and $d_N = 0.126$ mm when the injection pressure is different

Figure 3.15 shows the direct imaging and OH* chemiluminescence in different jet-jet angle when the injection was different. Similar with the case of $p_{inj} = 120$ MPa, the narrower jet-jet angle resulted in a shorter liquid length and the luminous flame closer to the nozzle. In addition, the lower injection pressure, which injection pressure was 80 MPa, spread the luminous flame more upstream of the fuel spray for both jet-jet angles. However, in the OH*chemiluminescence image, there is no major effect of the different injection pressures.

The effect of the jet-jet angle on the liquid length and the lift-off length under different injection pressures was also analyzed. Figure 3.16 shows the lift-off length and the liquid length for each injection pressure p_{inj} and jet-jet angle α . The liquid length at $p_{inj} = 80$ MPa for both α do not appear constant before -3° ATDC because the rising of the injection rate at $p_{inj} = 80$ MPa is lower than that of $p_{inj} = 120$ MPa. Then, at the ignition timing of -2° ATDC, the liquid length of all conditions was nearly equal. At $p_{inj} = 80$ MPa, the lift-off length of $\alpha = 45^\circ$ slowly decreased, and the liquid and lift-off length of $\alpha = 30^\circ$ rapidly decreased. These tendencies were similar to the case of the higher injection pressure. In a study using a single-hole nozzle, lower injection pressure shortened the lift-off length [18] but did not change the liquid length [19]. However, the lift-off length of both jet-jet angles were not significantly affected by the injection pressure in this study, which was similar to the case of Fuyuto's experiments with a single-hole nozzle and a fan-shaped combustion chamber [15]. The liquid length of $\alpha = 45^\circ$ was also not affected by the injection pressure. However, the falling timing of the liquid length of $\alpha = 30^\circ$ with the lower injection pressure occurred late.

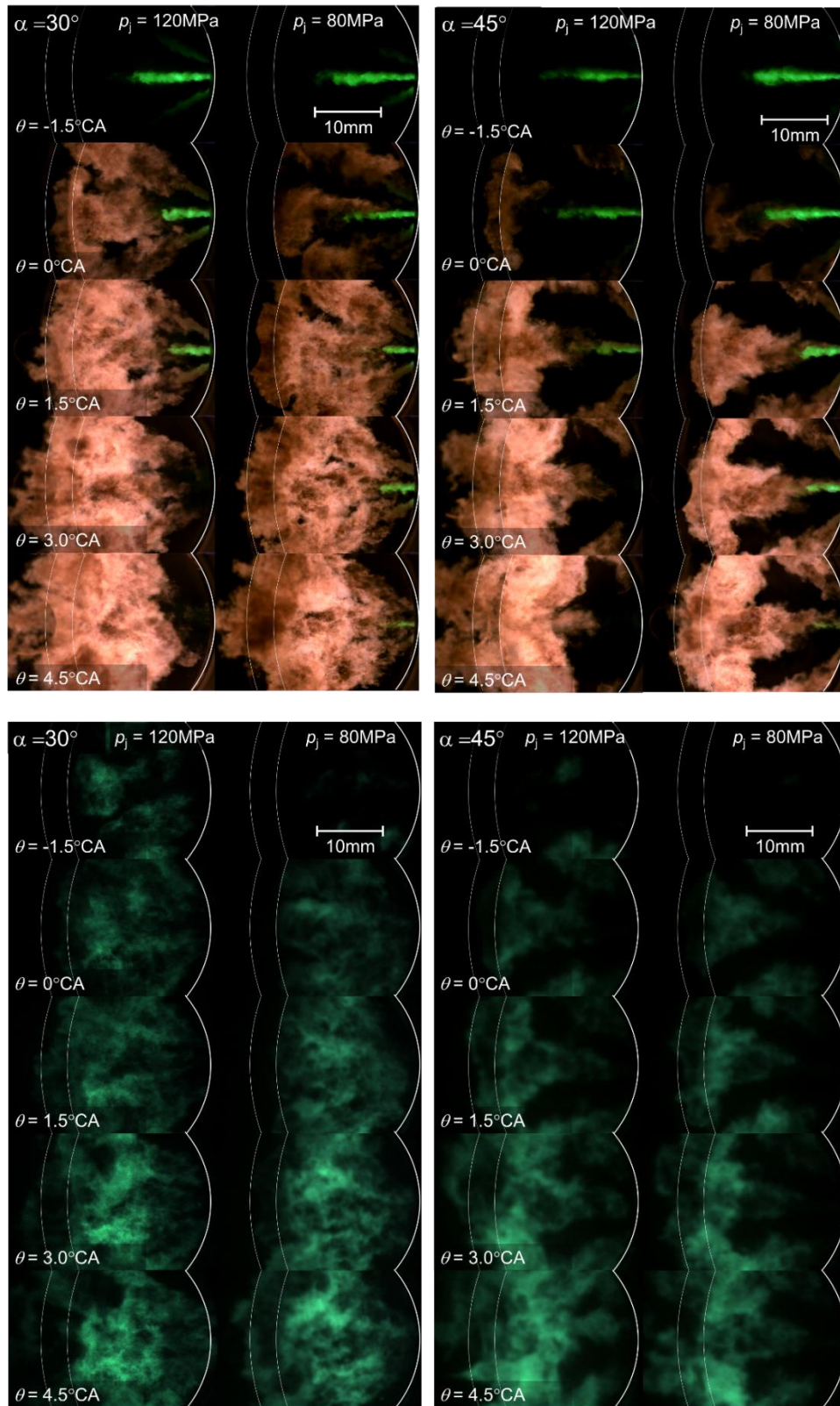


Figure 3.15 Image of direct imaging and OH* chemiluminescence to observe ignition phenomenon at different jet-jet angle ($\alpha = 30^\circ, 45^\circ$) and injection pressure ($p_{inj} = 80, 120\text{MPa}$) at $r_{O_2} = 19\%$ and $d_N = 0.126\text{mm}$

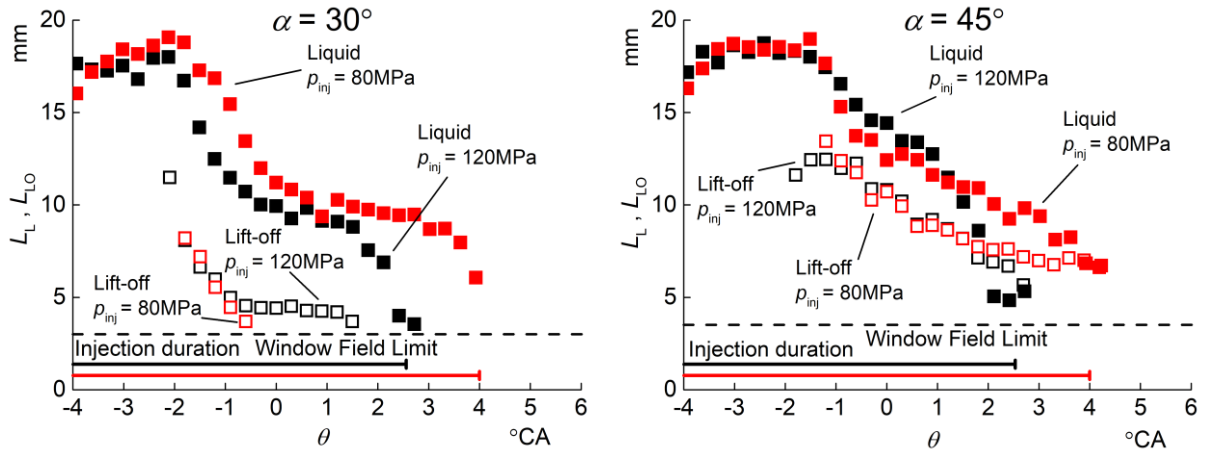


Figure 3.16 Lift-off length and Liquid length at different injection pressure ($p_{inj} = 80, 120$ MPa)

In other words, in the case of $\alpha = 45^\circ$, both liquid and lift-off length were not affected by injection pressure; however, in the case of $\alpha = 30^\circ$, the timing of shortening the liquid length was delayed with the lower injection pressure, while the lift-off length was unaffected. In the case of $\alpha = 45^\circ$, the effect of small-scale recirculation [15] is relatively small; therefore, there was little difference in the histories of liquid and lift-off length. In the case of $\alpha = 30^\circ$, the influence of small-scale recirculation is strong; however, lowering injection pressure reduces the recirculation speed. Therefore, it should affect the lift-off length before affecting the liquid length.

Next, the injector nozzle hole diameter d_N of 0.100 mm was applied to examine the effect of nozzle hole diameter, with $p_{inj} = 120$ MPa and $r_{O_2} = 19\%$. Figure 3.17 indicates the representative in-cylinder pressure p , heat release rate $dQ/d\theta$, and injection duration. The injection duration for $d_N = 0.100$ mm was longer than that of $d_N = 0.126$ mm. The ignition of $d_N = 0.100$ mm occurred earlier because of the evaporation ratio increase with the smaller nozzle hole [20].

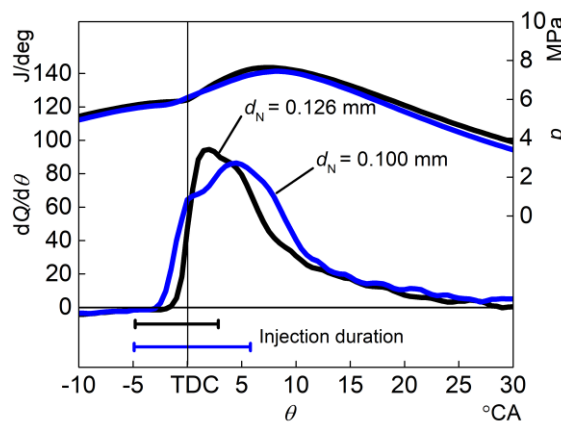


Figure 3.17 Heat release rate and in-cylinder pressure when using different nozzle hole diameter ($d_N = 0.100, 0.126$ mm) under the condition of $r_{O_2} = 19\%$ and $p_{inj} = 120$ MPa when the nozzle hole diameter is different

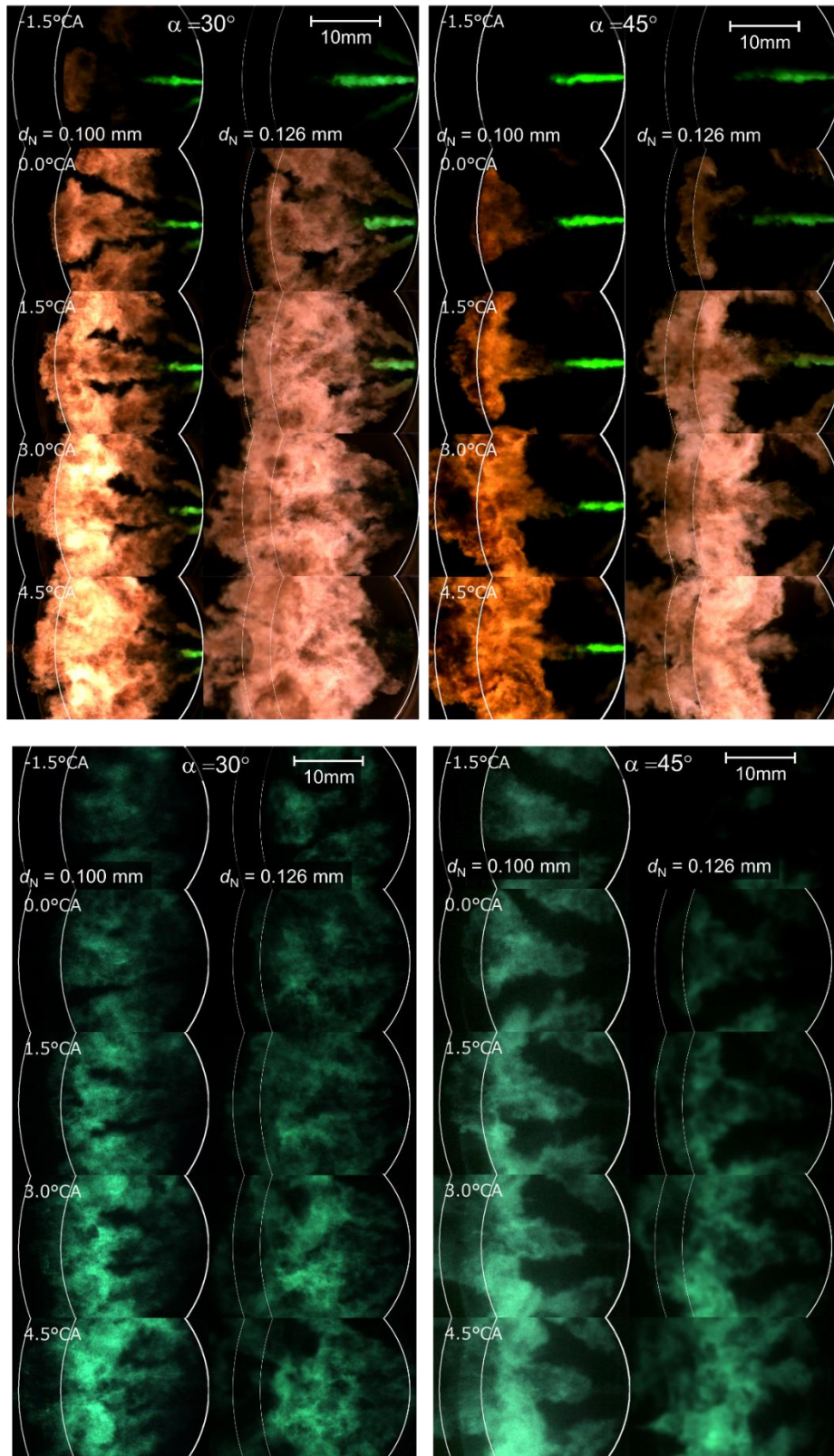


Figure 3.18 Image of direct imaging and OH* chemiluminescence to observe ignition phenomenon at different jet-jet angle ($\alpha = 30^\circ, 45^\circ$) using different nozzle hole diameter ($d_N = 0.100, 0.126$ mm) at $r_{O_2} = 19\%$ and $p_{inj} = 120$ MPa

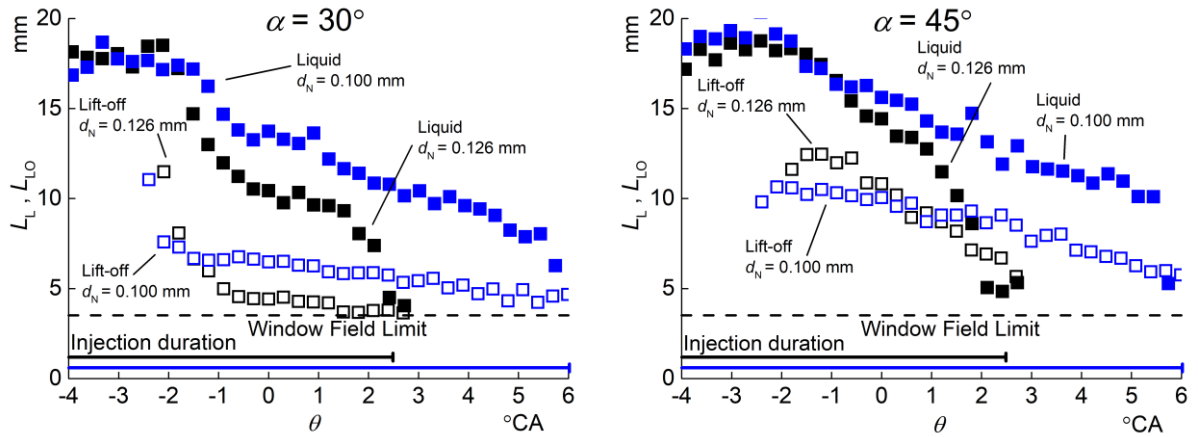


Figure 3.19 Lift-off length and liquid length depending on nozzle hole diameter ($d_N = 0.100, 0.126$ mm)

Figure 3.18 shows the direct imaging and OH* chemiluminescence of the combustion phenomena according to jet-jet angle α at $d_N = 0.100$ mm and 0.126 mm. The images on the left show the direct imaging at 1.5°ATDC, and the images on the right show the OH* chemiluminescence at the 3°ATDC. The timings for OH* chemiluminescence and direct imaging were different because the combustion phenomena according to the nozzle hole diameter were clearly distinguished. The jet-jet spacing of the luminous flame and OH* of $d_N = 0.100$ mm appeared wider compared to that of $d_N = 0.126$ mm. This phenomenon can be considered to be due to the result that the spray angle decreases when the nozzle hole diameter becomes small, which was found in previous studies.

The images were analyzed to measure the lift-off length and liquid length. Figure 3.19 shows the lift-off length and liquid length for each nozzle hole diameter and jet-jet angle. In the case of using a single-hole nozzle, a smaller nozzle shortened both liquid and lift-off length [19]. After the ignition, the liquid and lift-off length of $\alpha = 45^\circ$ with $d_N = 0.100$ mm slowly decrease, while those of $\alpha = 30^\circ$ with $d_N = 0.100$ mm rapidly decreased, although the falling timing of liquid length was later. These tendencies were similar to the case of the lower injection pressure because lowering the injection pressure and reducing the nozzle hole diameter both decrease the backward gas flow velocity, which lessens the influence of the recirculation of hot-burned gas in inter-jet spacing.

In the case of $d_N = 0.100$ mm, the decrease in lift-off and liquid length by narrowing the jet-jet angle was smaller compared to $d_N = 0.126$ mm. Also, with the smaller nozzle diameter, the lift-off length with $\alpha = 45^\circ$ decreased similarly to the case of a single-hole nozzle [18], while the liquid and lift-off length increased with $\alpha = 30^\circ$. From this result, it assumes that the smaller nozzle decreases the backward gas flow velocity, therefore, weakening the effect of inter-jet gas, including burnt gas on the liquid and lift-off length.

Summarizing the effect of injection condition, when the jet-jet angle was small, the liquid and lift-off length decreased rapidly just after the ignition; however, when the backward gas flow velocity was low, the moment of liquid length shortened was delayed. On the other hand, when the jet-jet angle was relatively large, the liquid and lift-off length gradually decreased. A major reason for these phenomena is small-scale recirculation which a backward flow from the burned gas [15].

3.3.3 Effect of oxygen concentration in different jet-jet angle

In this section, the effect of the oxygen concentration in the intake gas on the combustion process was examined. With a lower oxygen concentration, the temperature of in-cylinder gas before ignition does not change, but the burnt gas temperature and the thermal radiation of soot decrease, which could decrease the evaporation rate of spray. In the experiments, an oxygen concentration of 15% was applied under the conditions of injection timing of -5°ATDC , $p_{\text{inj}} = 120\text{ MPa}$, and $d_N = 0.126\text{ mm}$. Figure 3.20 indicates the representative in-cylinder pressure p , heat release rate $dQ/d\theta$, and injection duration against crank angle θ with r_{O_2} values of 15% and 19%. The ignition timing did not change with r_{O_2} , but the timing of the maximum heat release rate was delayed, and the combustion duration was lengthened, with decreasing oxygen concentration.

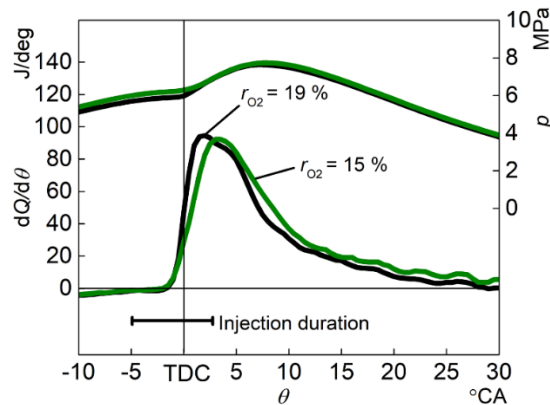


Figure 3.20 Heat release rate and in-cylinder pressure at different oxygen concentration ($r_{\text{O}_2} = 15, 19\%$) under the condition of $d_N = 0.126\text{ mm}$ and $p_{\text{inj}} = 120\text{ MPa}$ when the oxygen concentration is different

Figure 3.21 shows the direct imaging and OH^* chemiluminescence as a function of the oxygen concentration and jet-jet angle at 1.5°ATDC . Since the intensity of OH^* for $r_{\text{O}_2} = 15\%$ was significantly low, the contrast was adjusted so that the brightness was similar to the image of $r_{\text{O}_2} = 19\%$. Looking at the direct imaging, the luminous flame of $r_{\text{O}_2} = 15\%$ was dim because of the low flame temperature. The liquid length of $\alpha = 45^\circ$ does not differ significantly with the oxygen concentration. Unlike the case of $r_{\text{O}_2} = 19\%$, the spray length did not appear to change even if the jet-jet angle was smaller. The distance between the nozzle and the luminous flame and OH^* radical at $r_{\text{O}_2} = 15\%$ was clearly larger than at $r_{\text{O}_2} = 19\%$.

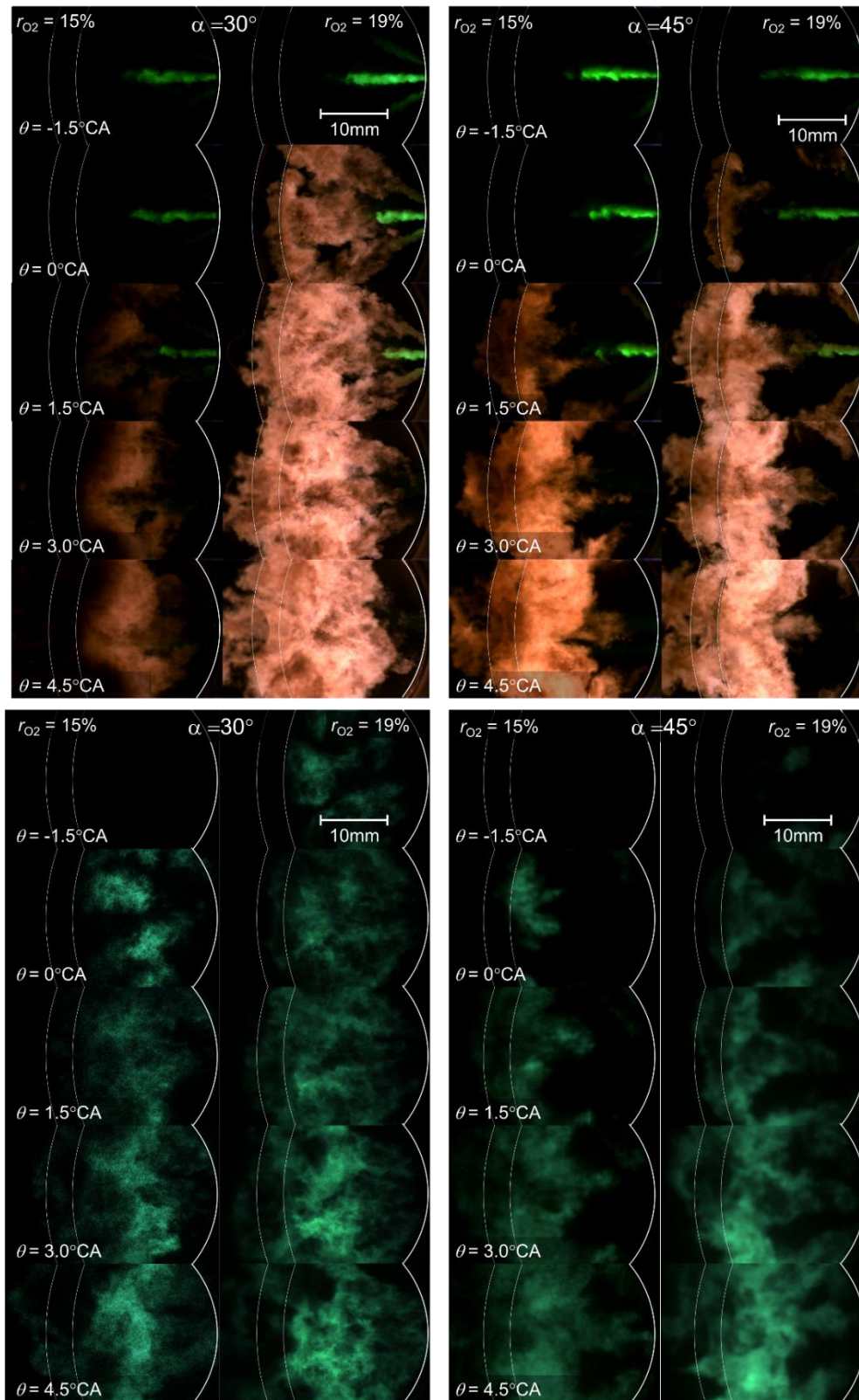


Figure 3.21 Image of direct imaging and OH* chemiluminescence to observe ignition phenomenon in different jet-jet angle ($\alpha = 30^\circ, 45^\circ$) and oxygen concentration ($r_{O_2} = 15, 19\%$) at $d_N = 0.126\text{ mm}$ and $p_{inj} = 120\text{ MPa}$

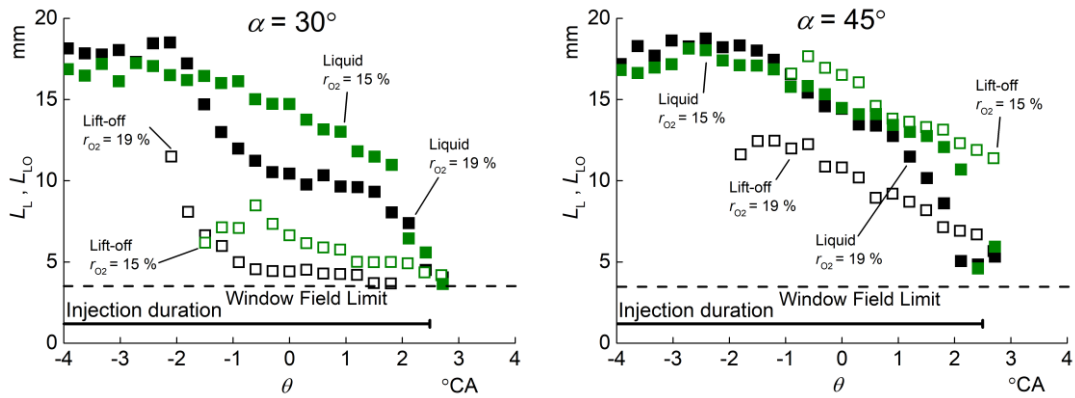


Figure 3.22 Heat release rate and in-cylinder pressure at different oxygen concentration ($r_{O_2} = 15, 19\%$) under the condition of $d_N = 0.126$ mm and $p_{inj} = 120$ MPa when the oxygen concentration is different

Next, the liquid length and lift-off length were analyzed. Figure 3.22 shows the lift-off length and liquid length with respect to oxygen concentration and jet-jet angle. The liquid length of both jet-jet angles at $r_{O_2} = 15\%$ was similar to that of $\alpha = 45^\circ$ at $r_{O_2} = 19\%$, which means the effect of entrainment of hot-burned gas was relatively small. The lift-off length of both jet-jet angles increased with less oxygen concentration, as expected. However, in the case of $\alpha = 45^\circ$, the lift-off length increased significantly, whereas, in the case of $\alpha = 30^\circ$, the increase in lift-off length was small. At $r_{O_2} = 15\%$, the lift-off length of $\alpha = 45^\circ$ tended to be longer than the liquid length, but the lift-off length of $\alpha = 30^\circ$ was shorter than the liquid length, similar to the case of $r_{O_2} = 19\%$. As clarified in previous studies, soot formation is high in atmospheric conditions with low oxygen concentration. Therefore, the thermal radiation effect of soot can be regarded as small. And, it can be considered that the entrainment of the hot burned gas in the multi-hole injector situation is the main cause of shortening the lift-off length.

3.3.4 Analysis of the velocity between sprays according to the jet-jet angle through the PIV method

Figure 3.23 shows the in-cylinder pressure, heat release rate, and fuel injection rate in this experiment. The red line shows the result under the combustion condition, and the black line shows the result under the non-combustion condition. The composition ratio of the premixed air under combustion conditions was 41 mol% of N_2 , 40 mol% of Ar, and 19 mol% of O_2 , which was selected to reduce the ignition delay in order to extend the quasi-steady state after fuel injection as described above. Since the fuel injection start timing was $-5^\circ CA$ and the ignition timing was $-1.7^\circ CA$, the ignition delay was $3.3^\circ CA$. Looking at the heat release rate results, it was judged that premixed combustion proceeded until $1.2^\circ CA$ after ignition started, and then diffusion combustion proceeded until fuel injection was finished.

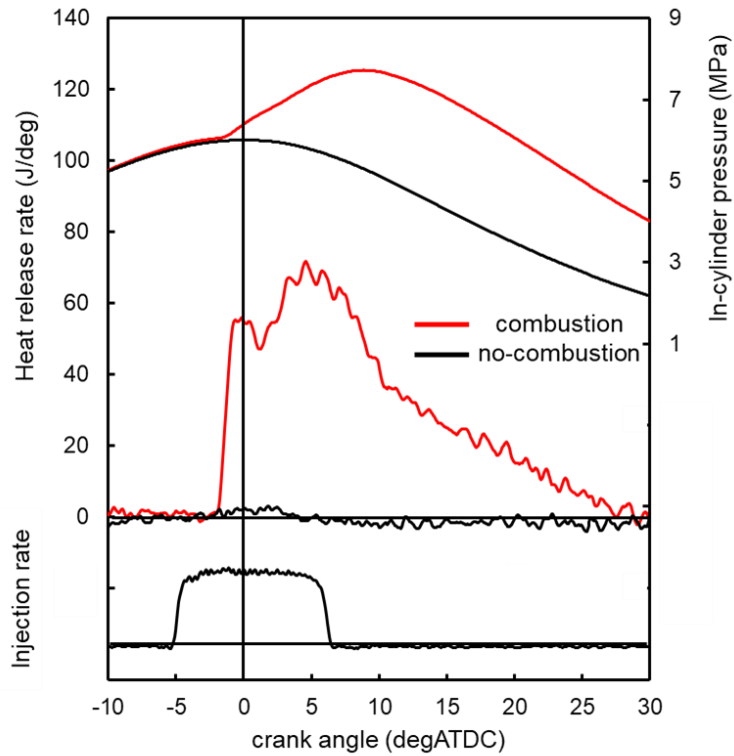


Figure 3.23 Heat release rate and in-cylinder pressure for PIV experiment
($d_N = 0.100$ mm under the condition of $r_{O_2} = 19\%$ and $p_{inj} = 120$ MPa)

In this study, experiments were conducted not only under combustion conditions but also non-combustion conditions. Because it was necessary to check whether the results differ depending on the combustion and non-combustion conditions. So, we compared whether there is a difference between the velocity in the backward flow velocity and the entrainment velocity in the combustion and non-combustion conditions when the jet-jet angle was 45° .

Figure 3.24 shows the original image of PIV in the non-combustion situation where the jet-jet angle was 45° , and the analyzed image of the velocity vector map. At -4.8°CA before fuel injection started, the flow inside the combustion chamber was very random. After that, the flow between the diesel sprays towards the injector tip when the injection starts. Even after that, the flow direction between the diesel sprays was toward the injector tip until the injection was completed in a quasi-steady state of fuel injection.

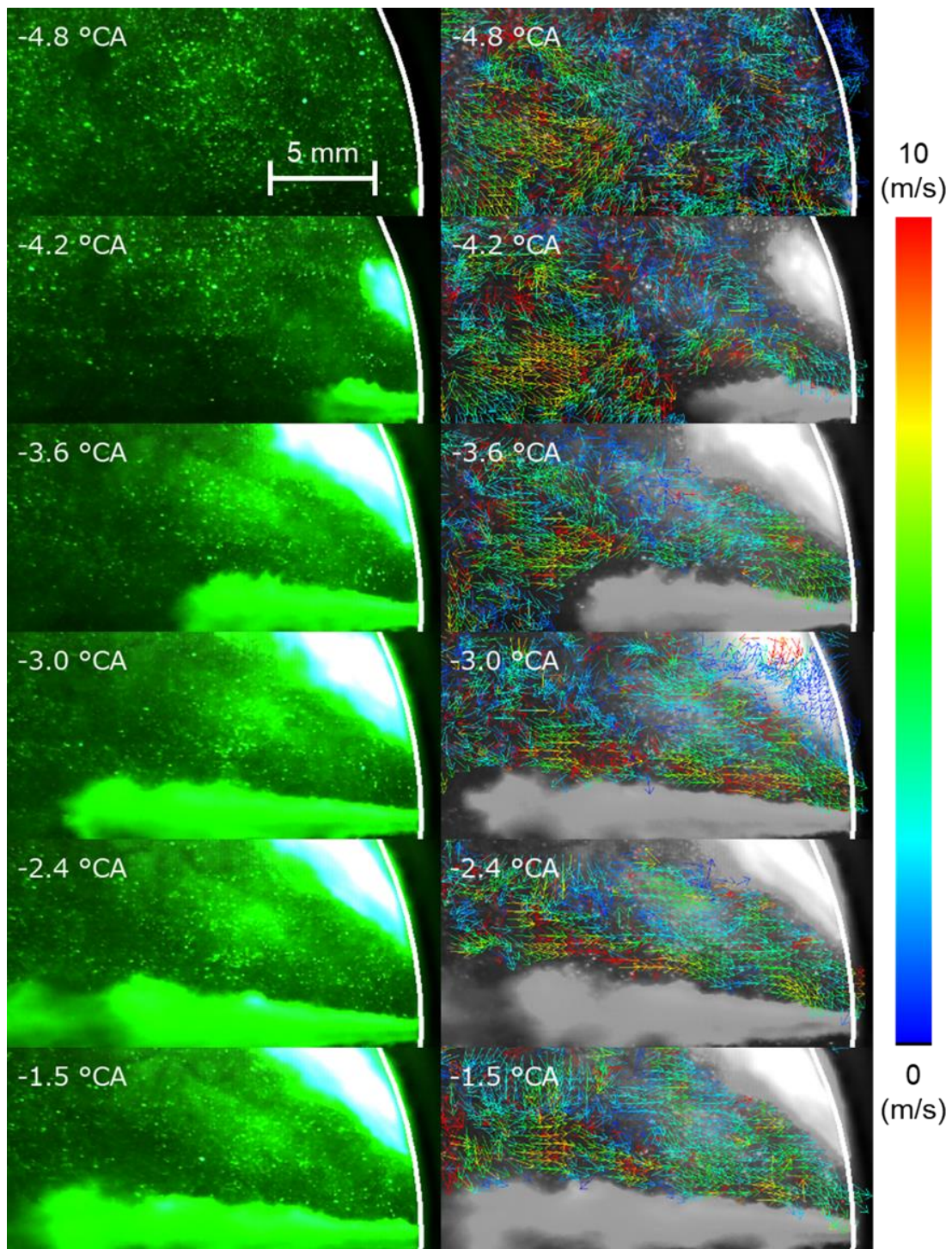


Figure 3.24-1 Raw PIV image and PIV analysis result image from -4.8 to 8.7°C

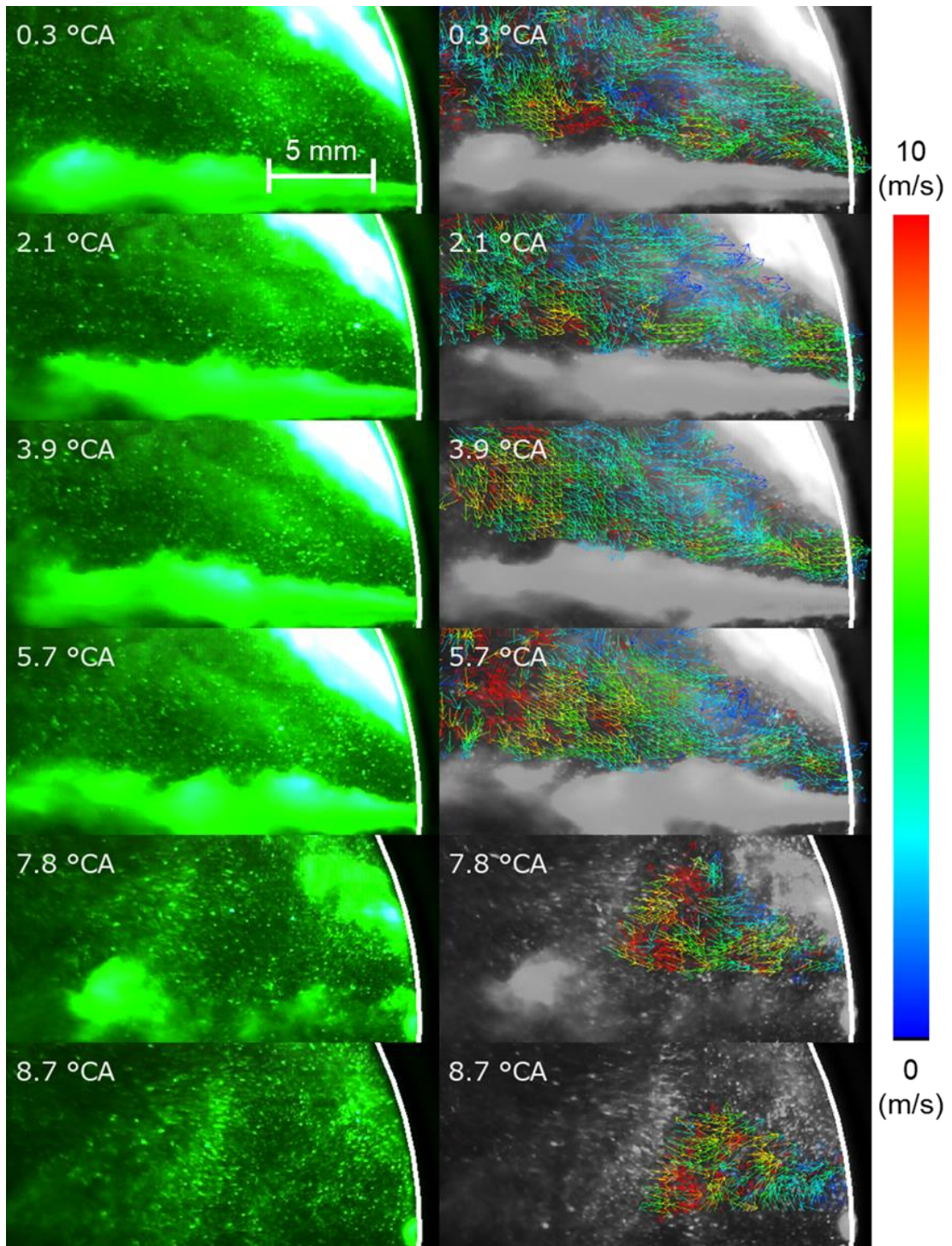


Figure 3.24-2 Raw PIV image and PIV analysis result image from -4.8 to 8.7°CA

Figure 3.25 shows the average backward flow velocity at each cell position between sprays. The horizontal axis of the graph shows the time, and the dotted line on the graph shows the timing at which fuel injection started. Looking at the graph, it showed that the backward flow velocity rapidly increased immediately after fuel injection started, and the magnitude of the velocity was about 4 m/s. The occurrence of backward flow field in the direction of the injector tip by an adjacent spray was also seen in a previous study by Toda et.al [14]. According to the previous research results, when the injection pressure was 200 MPa and the angle between adjacent sprays was 45° , the backward flow velocity was about 2 m/s. In this study, it is judged that the backward flow velocity was faster than in previous study because the spray impinging to the wall of the piston as well as the adjacent spray affect the flow field between the sprays. Also, from -3°CA , backward flow velocity was larger as it got closer to the injector tip. It was judged that the closer the distance to the adjacent diesel spray, the greater the influence. Therefore, it was determined that the closer to the injector tip, the faster the backward flow velocity.

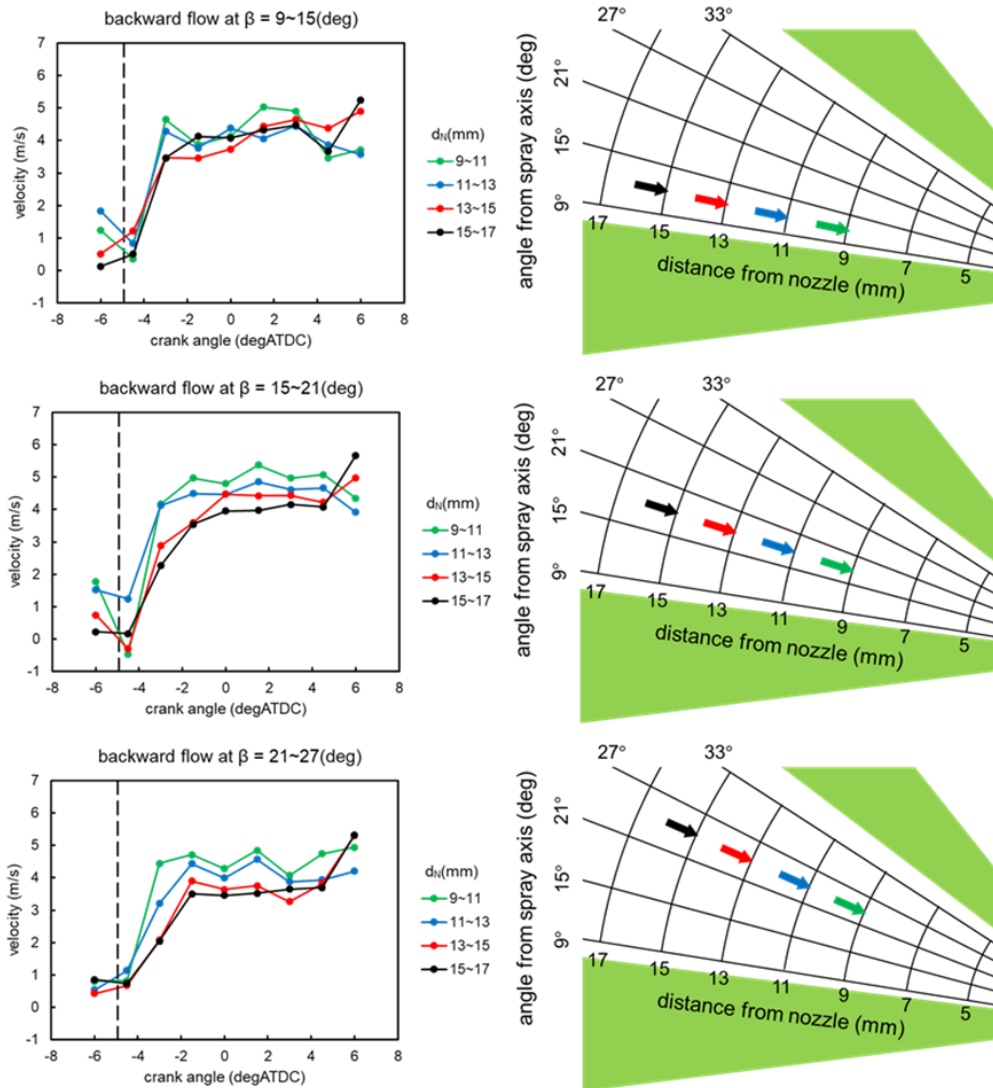


Figure 3.25 Average backward velocity over time in each calculation cell which same β position on $\alpha = 45^\circ$

Figure 3.26 shows the entrainment velocity at each cell position. Looking at the graph, the black line shows the result of the position closest to the target diesel spray. However, it can be seen that the entrainment velocity increases rapidly after injection starts, and it was maintained at about 1.5 m/s after reaching a quasi-steady state. And the larger the angle with the target diesel spray axis, the entrainment velocity was negative. This means that as the position of the cell is further away from the target diesel spray, the position with the adjacent diesel spray becomes closer. Therefore, the flow close to the adjacent spray is formed into a flow field that is entrained into the adjacent spray.

As a result, it was shown that the flow between the diesel spray was entrained into the adjacent diesel spray. And, it was shown that the closer to diesel spray, the entrainment velocity is faster.

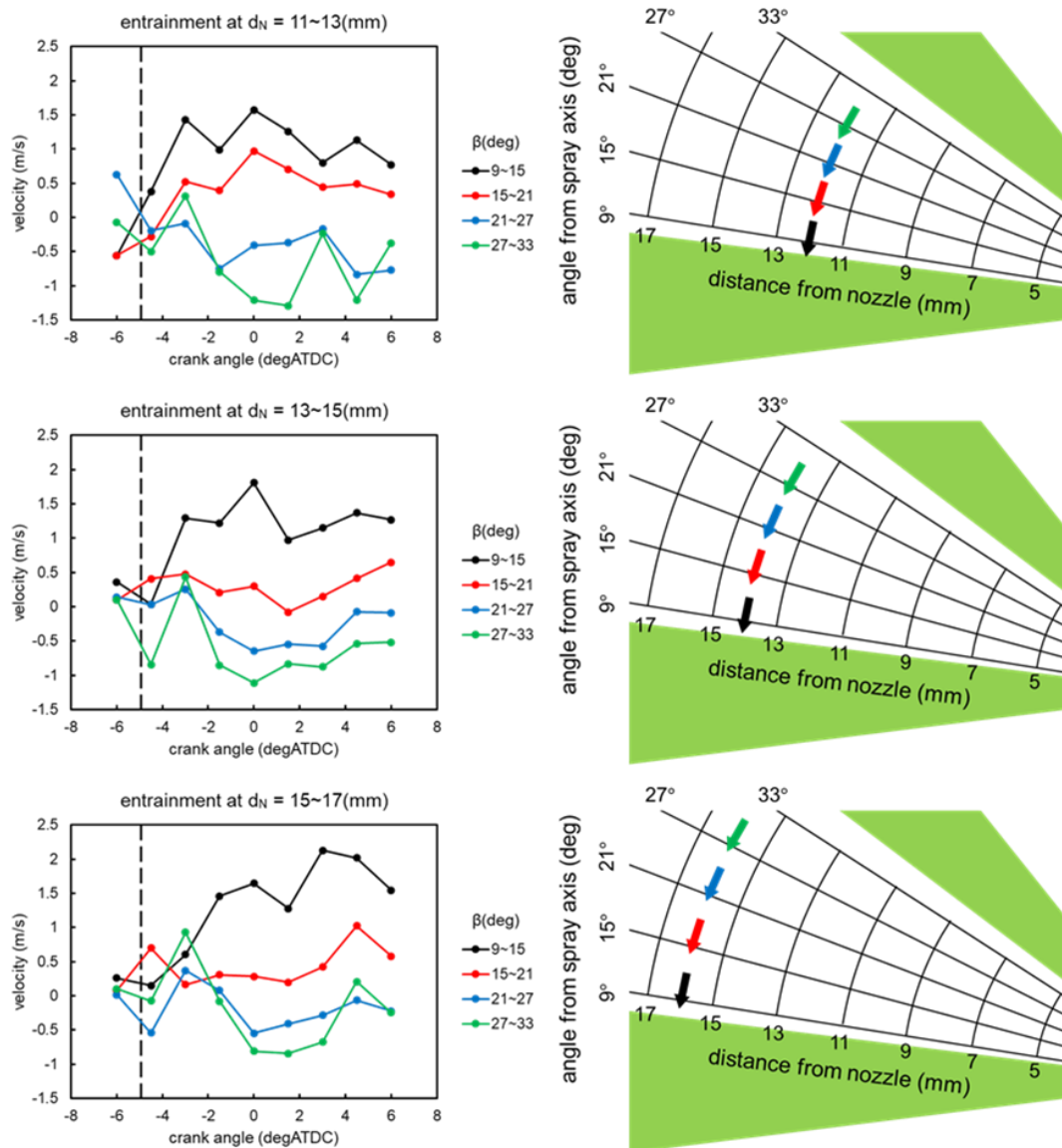


Figure 3.26 Average entrainment velocity over time in each calculation cell which the same d_N on $\alpha = 45^\circ$

Figure 3.27 shows the velocity vector maps over time between the sprays under non-combustion and combustion conditions. After 0.0°CA , the flame spread was shown in the spray shape of the image under combustion conditions. PIV could not be carried out in this area because the light emitted from the flame and scattered light from the tracer could not be captured in the liquid spray part. However, the trend of the flow between the sprays toward the injector tip in both the combustion and non-combustion conditions could be observed. Therefore, the results in the area where PIV was possible even in the combustion situation were compared and analyzed with the results in the non-combustion situation.

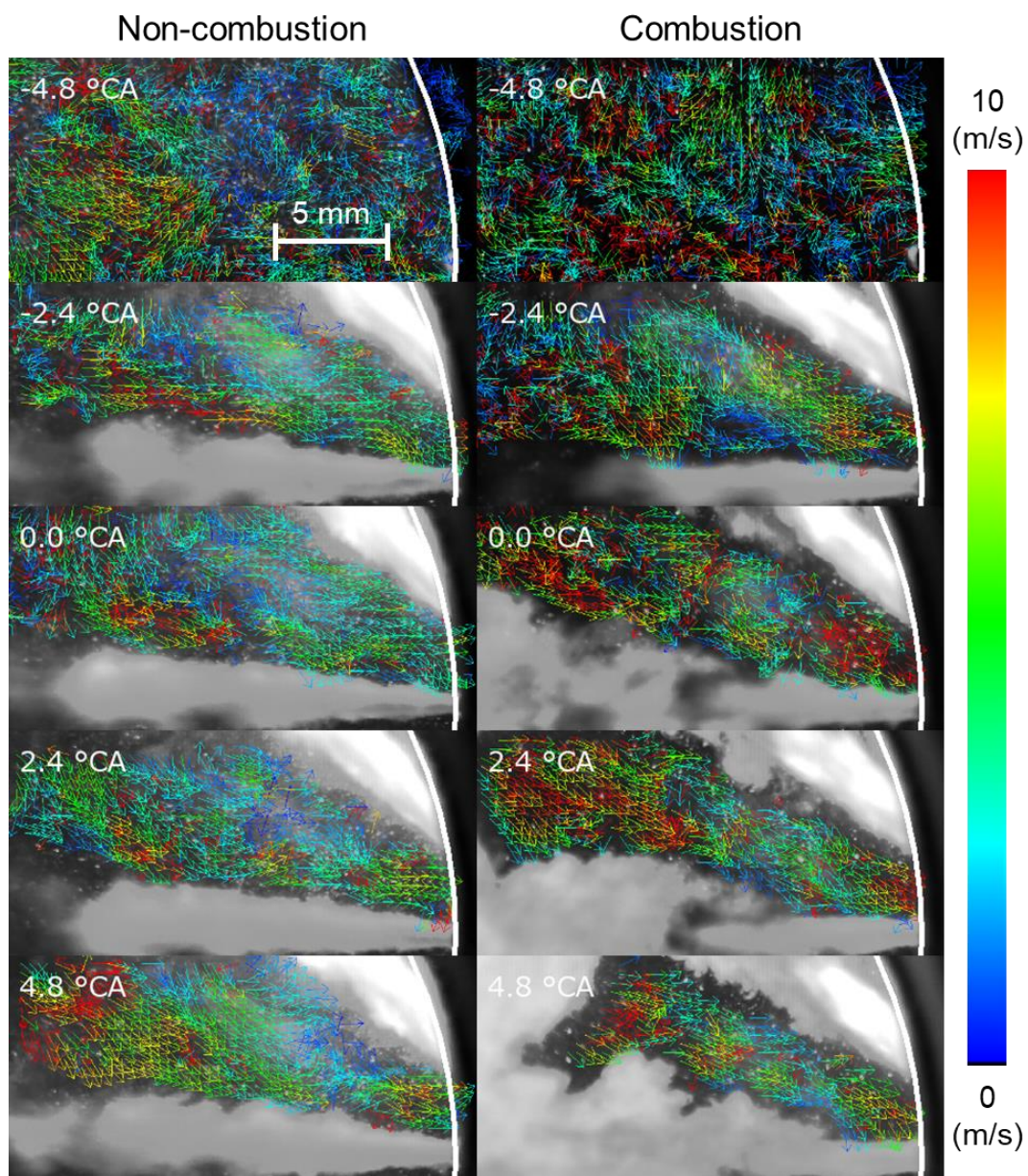


Figure 3.27 Vector map comparing non-combustion and combustion condition from -4.8 to 4.8°CA on $\alpha = 45^\circ$

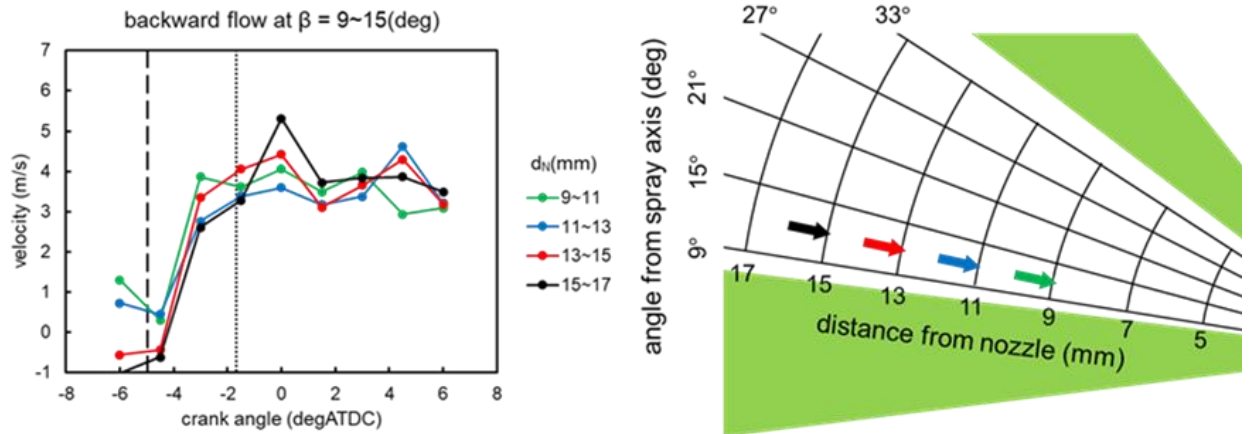


Figure 3.28 Average backward velocity in combustion over time in each calculation cell which the same β position and each d_N position on $\alpha = 45^\circ$

Figure 3.28 shows the result of the backward flow in the cell at a distance of 9 to 15 mm from the injector tip when the jet-jet angle is 45° and the angle with the target spray axis, β , was 9 to 15° under combustion conditions. The long-dash line on the left on the graph shows the injection timing, and the next dash line shows the ignition timing. After the injection starts, the backward flow velocity increased and then constantly maintained even at different locations. After the ignition starts, the backward flow velocity at the furthest position from the injector tip temporarily increase again. It was determined that this was because the air in the combustion chamber was pushed toward the injector tip as the pre-mixture of air and fuel, which was mainly formed downstream of the spray, was ignited and expanded.

Figure 3.29 shows the result of comparing the backward flow velocity under the combustion and non-combustion condition. In the graph, the solid line shows the backward flow velocity in non-combustion condition, and the dashed line shows the backward flow velocity in combustion condition. Looking at the result of $d_N = 15\sim 17$ mm located farthest from the injector tip at 0.0°CA , which is the peak moment of the premixed combustion, the backward flow velocity temporarily increased, exceeding the backward flow velocity in the non-combustion condition. However, during the combustion period, the backward flow velocity of the combustion condition was slightly reduced at any location. It can be judged that the average backflow velocity is relatively decreased as the backward flow is neutralized with the expanded surrounding air with the spray momentum due to combustion.

Figure 3.30 shows the result of comparing the entrainment velocity under combustion and non-combustion situation. As a result, no big difference was found according to the difference between the combustion condition and the non-combustion condition. Therefore, it was determined that the entrainment flow to diesel spray was not significantly affected by combustion.

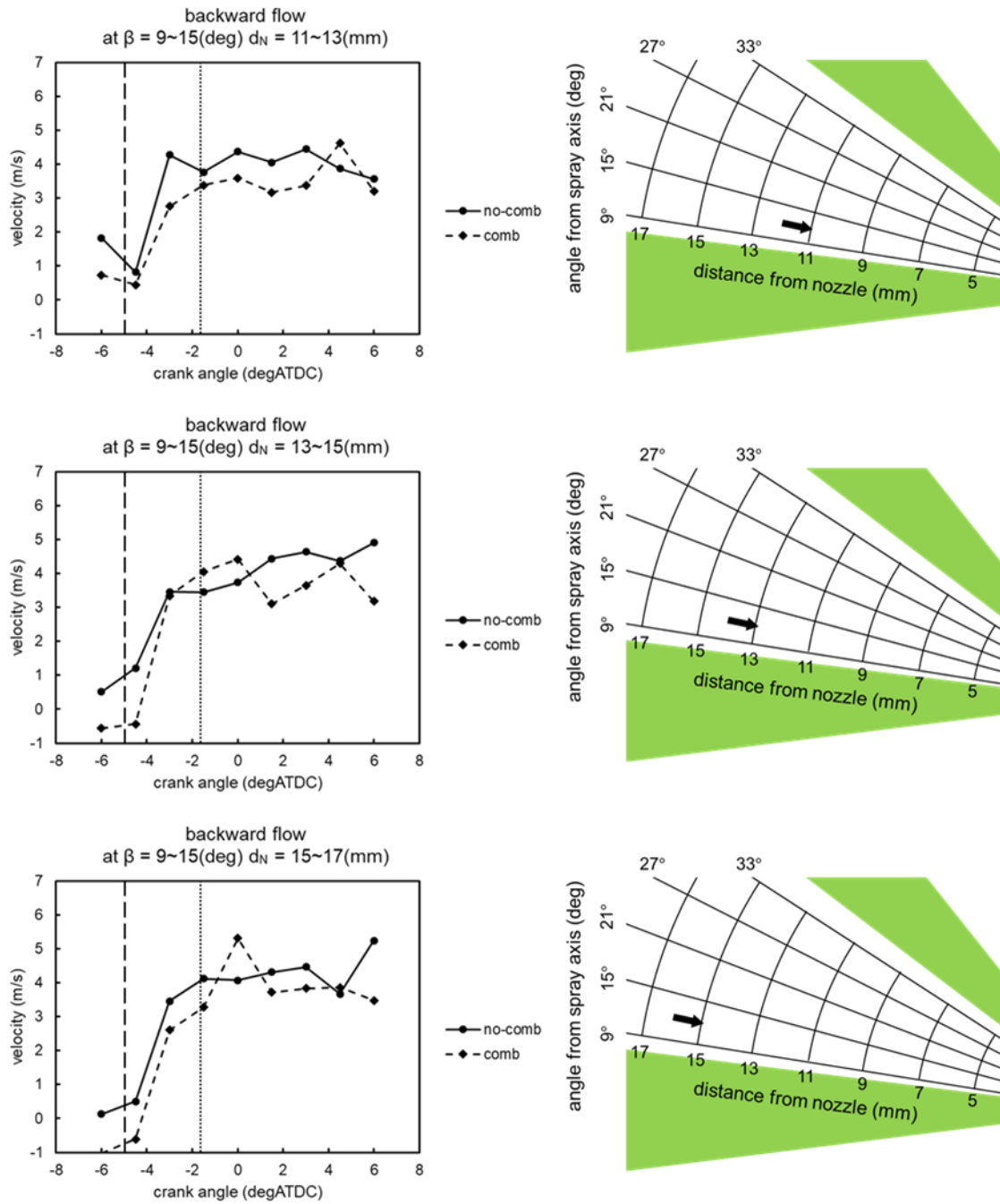


Figure 3.29 Average backward velocity in non-combustion and combustion over time in each calculation cell which the same β position and each d_N position on $\alpha = 45^\circ$

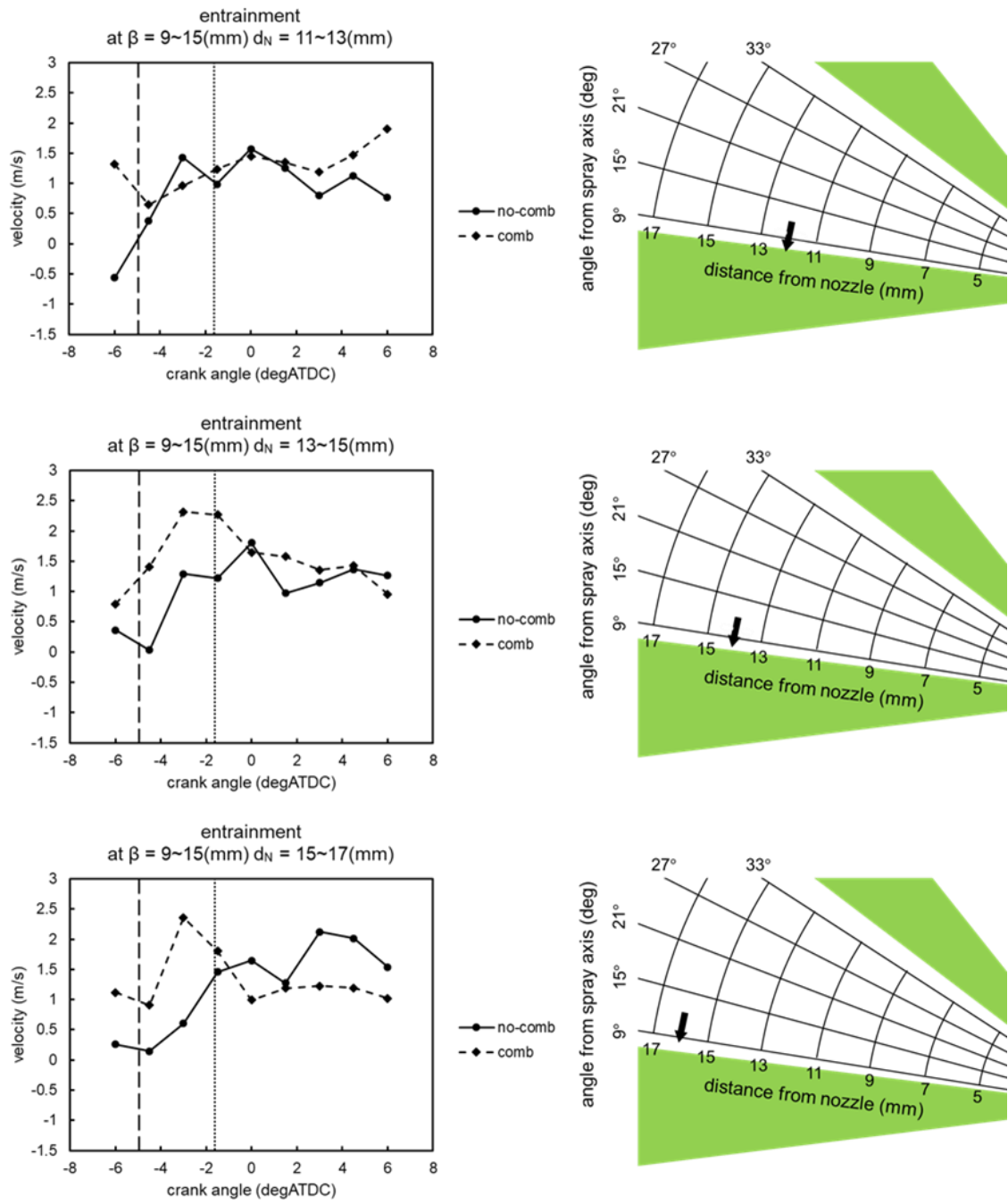


Figure 3.30 Average entrainment velocity in non-combustion and combustion over time in each calculation cell which the same β position and each d_N position on $\alpha = 45^\circ$

Next, the effect of jet-jet angle difference on the flow between sprays was investigated. To compare the effects of the flame, both non-combustion and combustion conditions were experimented and the results were analyzed.

First, explain how the flow between the sprays appears when the jet-jet angles are 30° and 45° , respectively, in the combustion situation. Figure 3.31 shows the velocity vector map when the jet-jet angle is $\alpha = 30^\circ$ on the left and $\alpha = 45^\circ$ on the right under non-combustion conditions. In both cases, the flow inside the combustion chamber was random before fuel injection started. After the fuel injection has started, the flow will appear moving towards the injector tip.

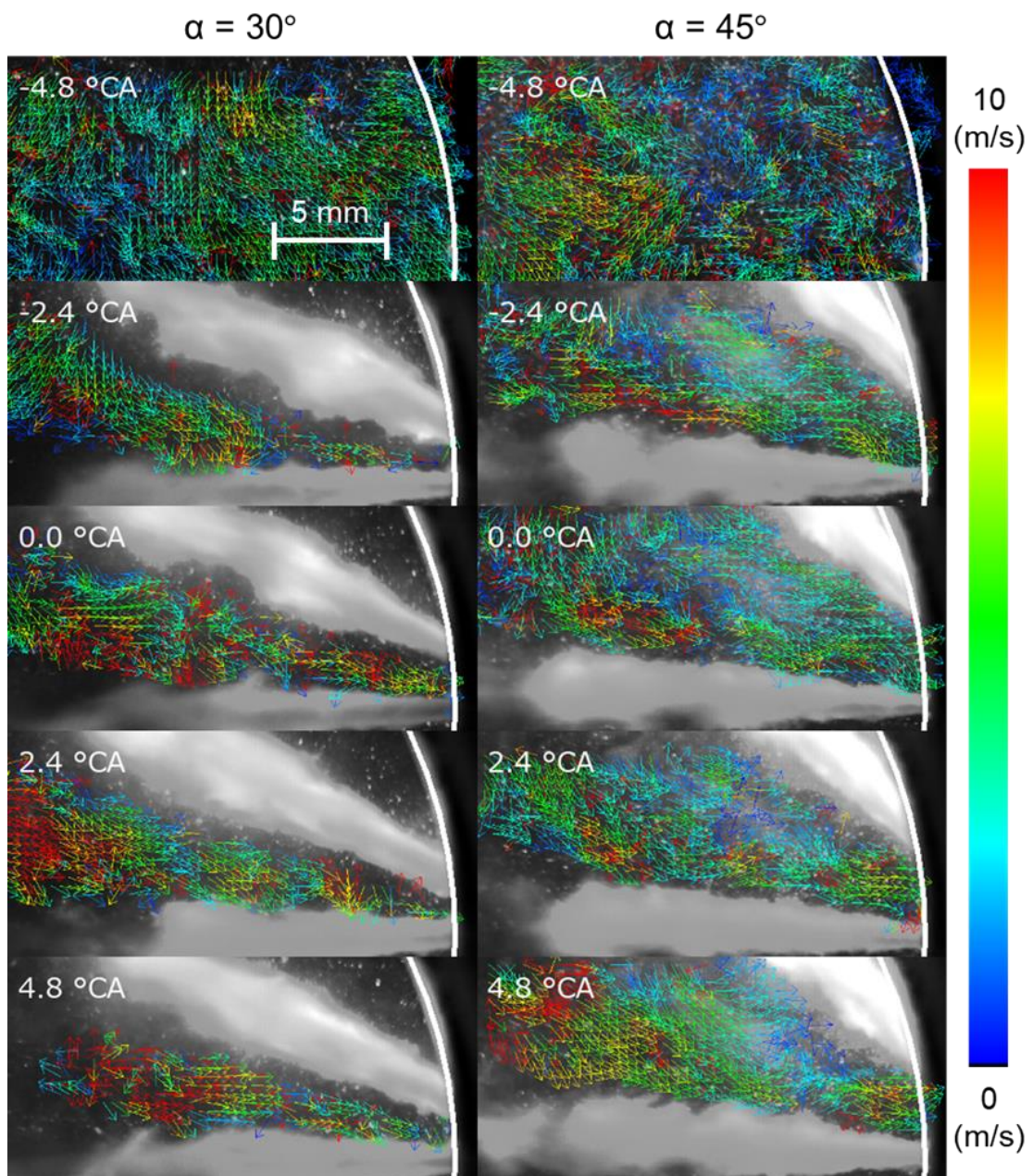


Figure 3.31 Vector map comparing non-combustion from -4.8 to 4.8°CA on $\alpha = 30^\circ, 45^\circ$

Figure 3.32 is a graph of the backward flow velocity at each position according to the jet-jet angle. The solid line in the graph shows the results of the backward flow velocity of $\alpha = 45^\circ$, and the dashed line shows the result of the backward flow velocity of $\alpha = 30^\circ$. As a result, it was shown that the backward flow velocity increases when the jet-jet angle was small. This can be explained based on the phenomenon that the backward flow velocity increases when the spacing between spray is narrowed. As the jet-jet angle decreases, the spacing between sprays become narrower, and it can be assumed that the backward flow velocity increases as the jet-jet angle decreases.

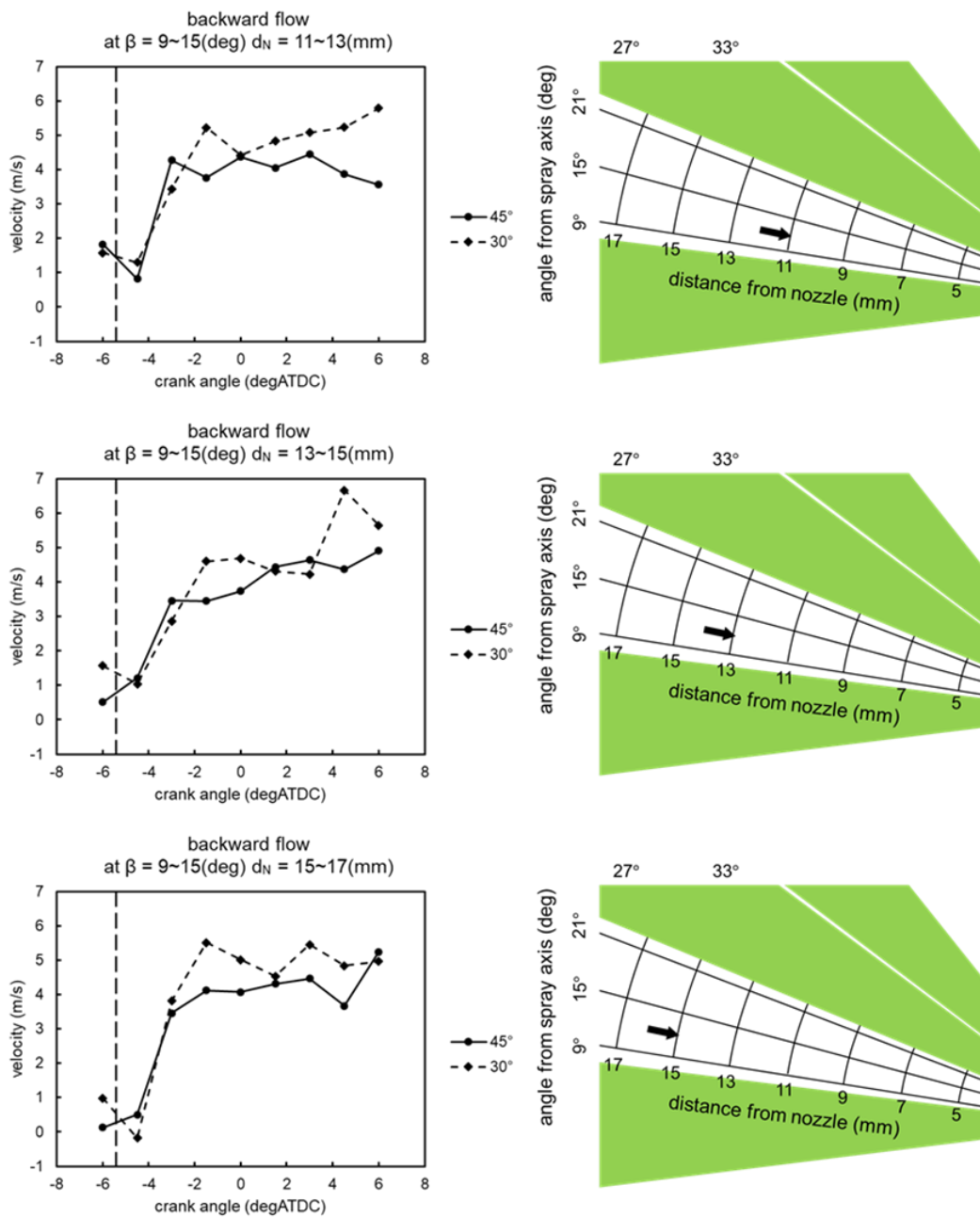


Figure 3.32 Average backward velocity in non-combustion over time in each calculation cell which the same β position and each d_N position on $\alpha = 30^\circ, 45^\circ$

Figure 3.33 is a graph showing the entrainment velocity at each position according to the jet-jet angle. Looking at the results, even if the jet-jet angle was changed, there was no significant difference at about 1.5 m/s in the quasi-steady state. In the previous results, as the spacing between sprays decreased, the backward flow velocity was increased, but the entrainment velocity did not change significantly. Likewise, even if the jet-jet angle was small, the change in entrainment velocity was not large. Considering that the same amount of air moves from the downstream of the spray toward the injector tip as the spacing between the sprays is smaller, it can be determined that the backward flow velocity is increased because there is no big difference in the entrainment velocity.

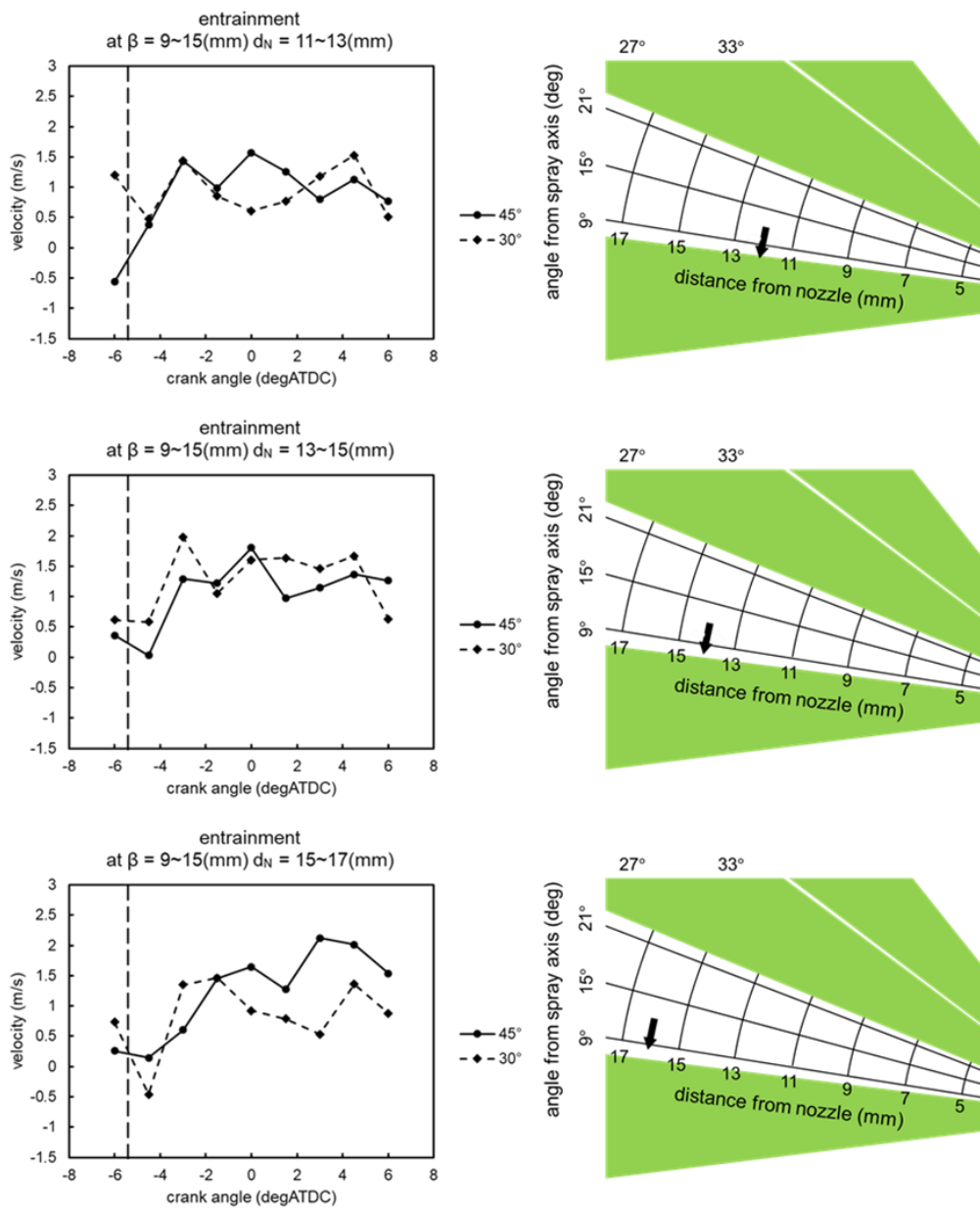


Figure 3.33 Average entrainment velocity in non-combustion over time in each calculation cell which the same β position and each d_N position on $\alpha = 30^\circ, 45^\circ$

Next is an analysis of the flow between the sprays according to the jet-jet angle under combustion conditions. Figure 3.34 shows the vector map according to the jet-jet angle in combustion conditions. Commonly, as the fuel injection started, the flow between the sprays was directed towards the injector tip. In the combustion situation, flame is creating an area where the tracer's scattered light, so the tracer was not visible in this area. In particular, at $\alpha = 30^\circ$, it can see that the flame spreads widely in the spacing between the sprays as well. So, in the case of combustion conditions, the areas where PIV analysis was possible were compared with each other.

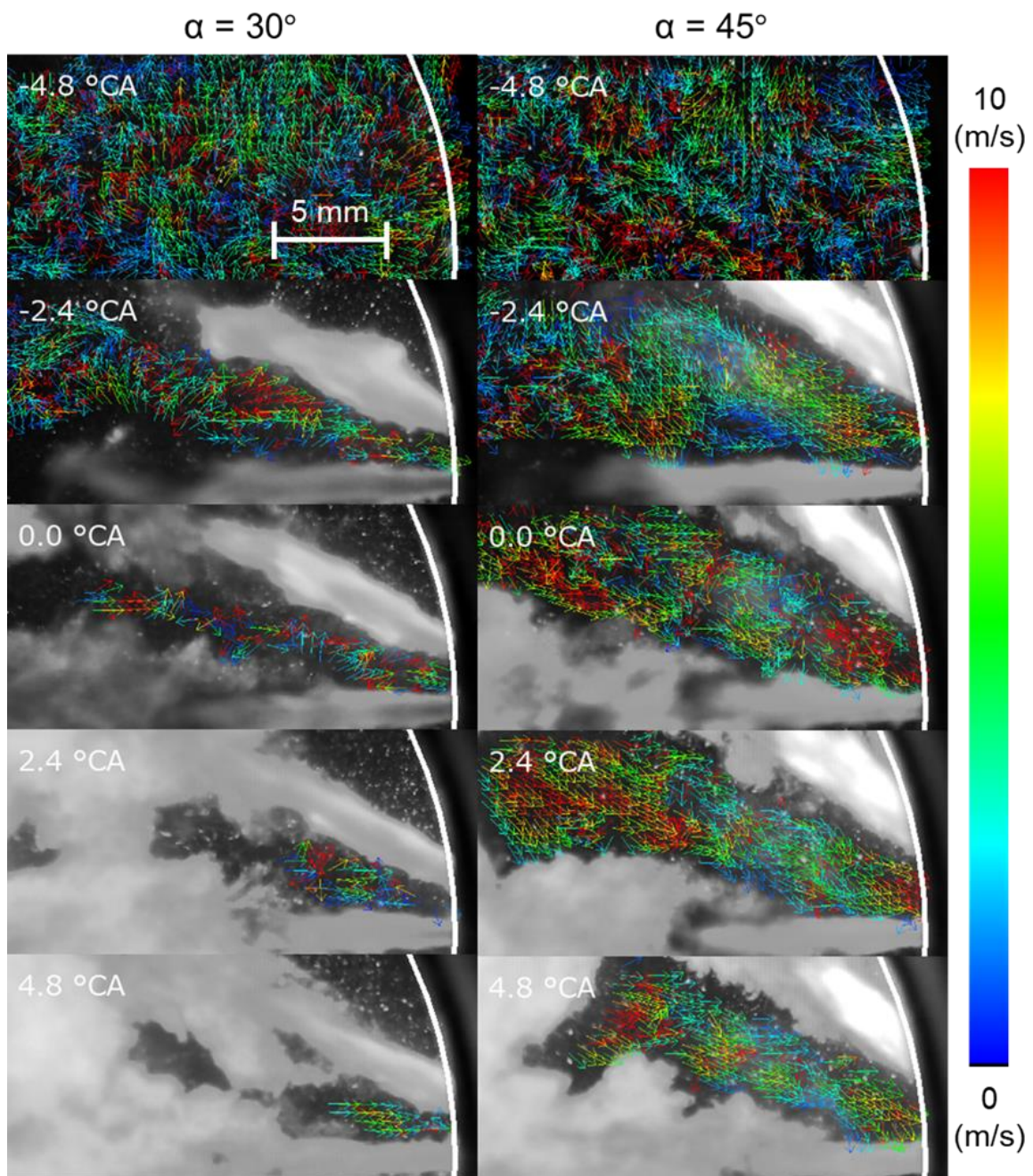


Figure 3.34 Vector map comparing combustion from -4.8 to 4.8°CA on $\alpha = 30^\circ, 45^\circ$

Figure 3.35 shows the result of the backward flow velocity according to the jet-jet angle under combustion condition. Comparing with the result of the backward flow velocity in the non-combustion condition, the variation in the backward flow velocity in the combustion condition was relatively large according to the jet-jet angle. It can be assumed that the ignition timing in the combustion situation has an effect as well as the effect of the limited area between the sprays. In addition, after 1.5°CA, which corresponds to the diffusion combustion period, when $\alpha = 30^\circ$, the backward flow velocity decreased sharply compared to $\alpha = 45^\circ$. This is because the smaller the jet-jet angle, the shorter the lift-off length, so the area that interferes with the PIV analysis area expands as the air with the momentum of the spray expands due to combustion.

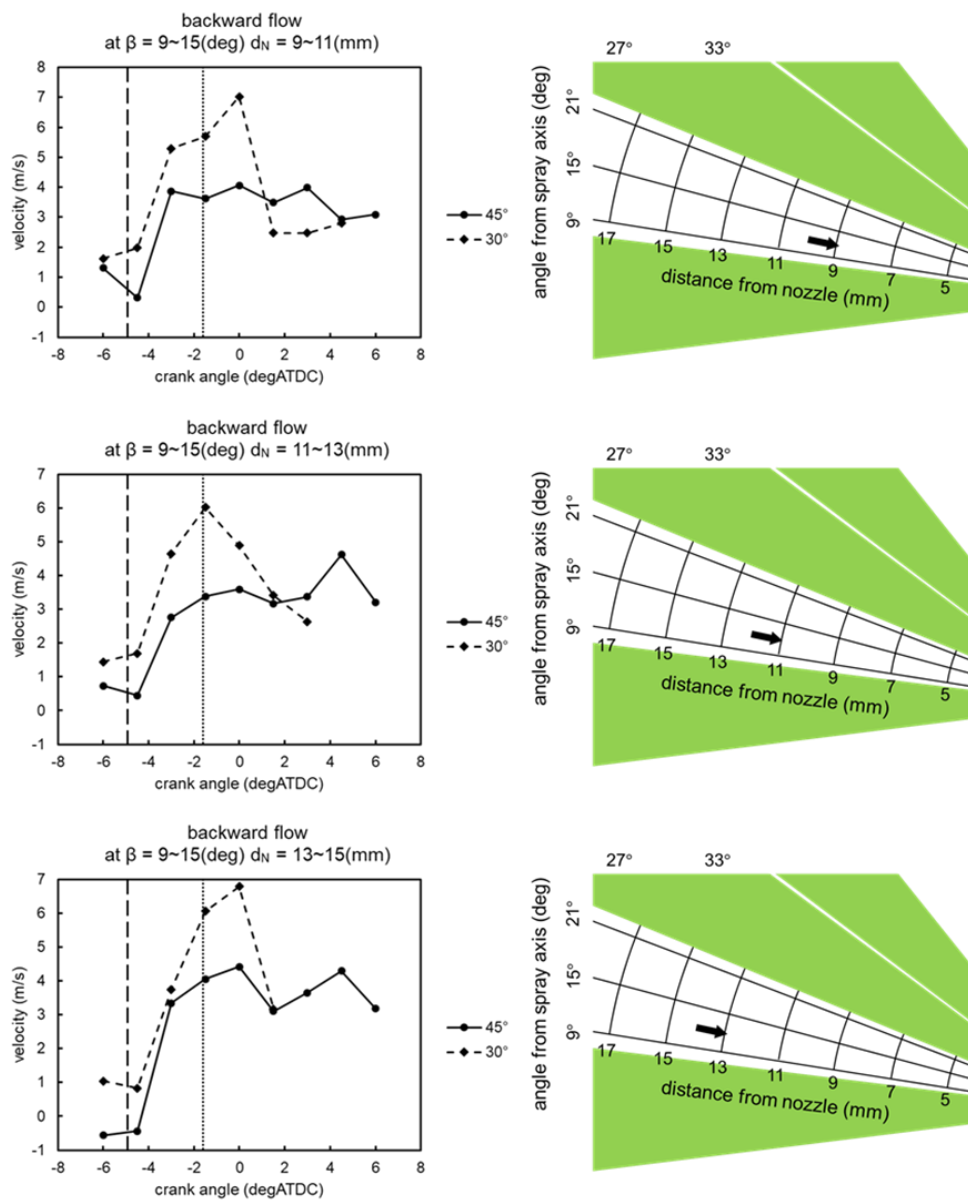


Figure 3.35 Average backward velocity in combustion over time in each calculation cell which the same β position and each d_N position on $\alpha = 30^\circ, 45^\circ$

Figure 3.36 shows the results of entrainment velocity results according to jet-jet angle under combustion condition. As a result, similar to the results in the non-combustion condition, the entrainment velocity did not change in the combustion condition drastically. Based on this, the jet-jet angle was smaller, the more pre-mixture formed downstream of the spray. So, when it expands after ignition, the phenomenon of pushing the air between the sprays into the injector tip becomes stronger. However, it was confirmed that the entrainment velocity did not change significantly even under the combustion condition when compared to the non-combustion condition. Therefore, it can be determined that under combustion condition, especially at the start of ignition, the jet-jet angle was smaller, the backward flow velocity going faster.

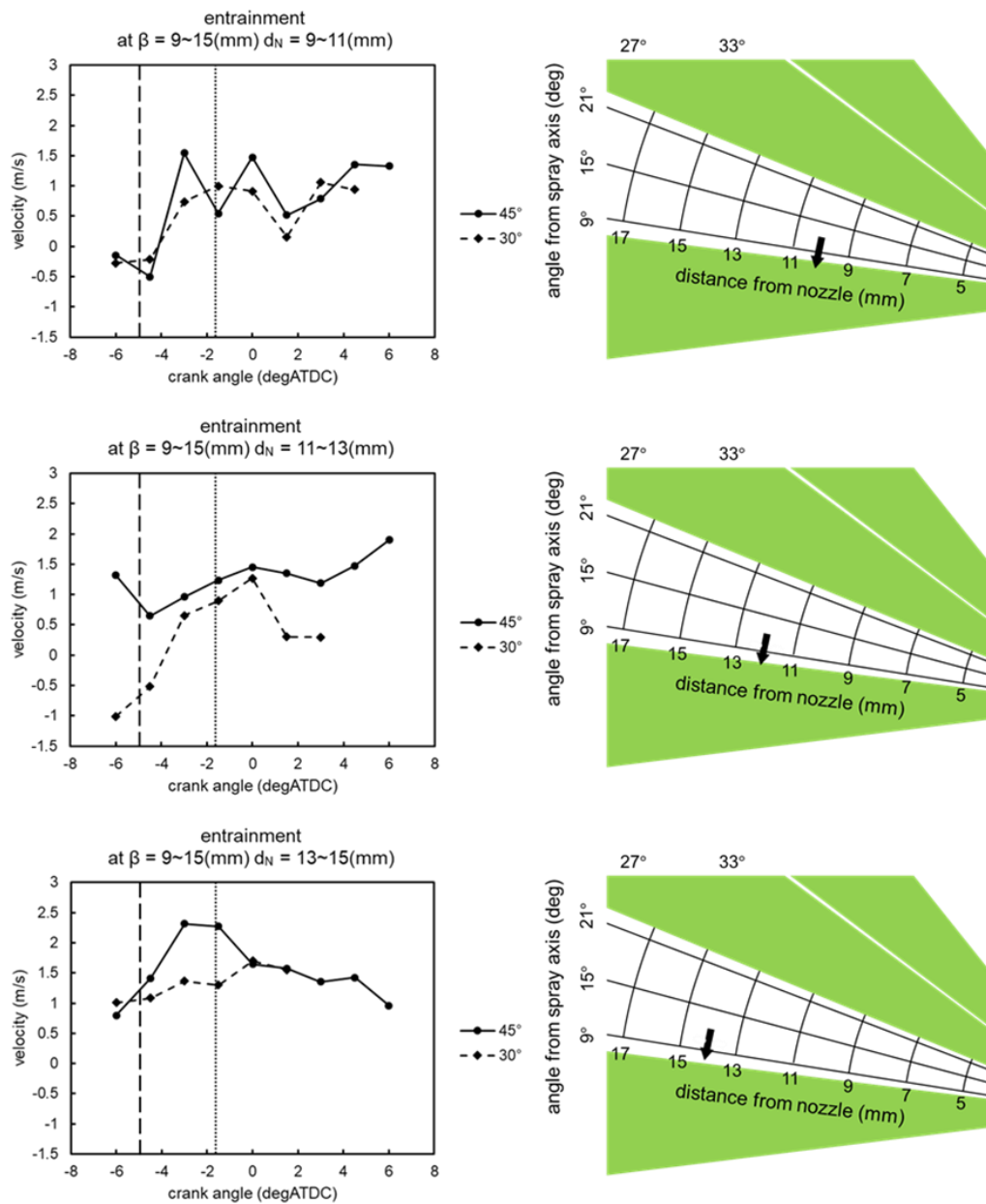


Figure 3.36 Average entrainment velocity in combustion over time in each calculation cell which the same β position and each d_N position on $\alpha = 30^\circ, 45^\circ$

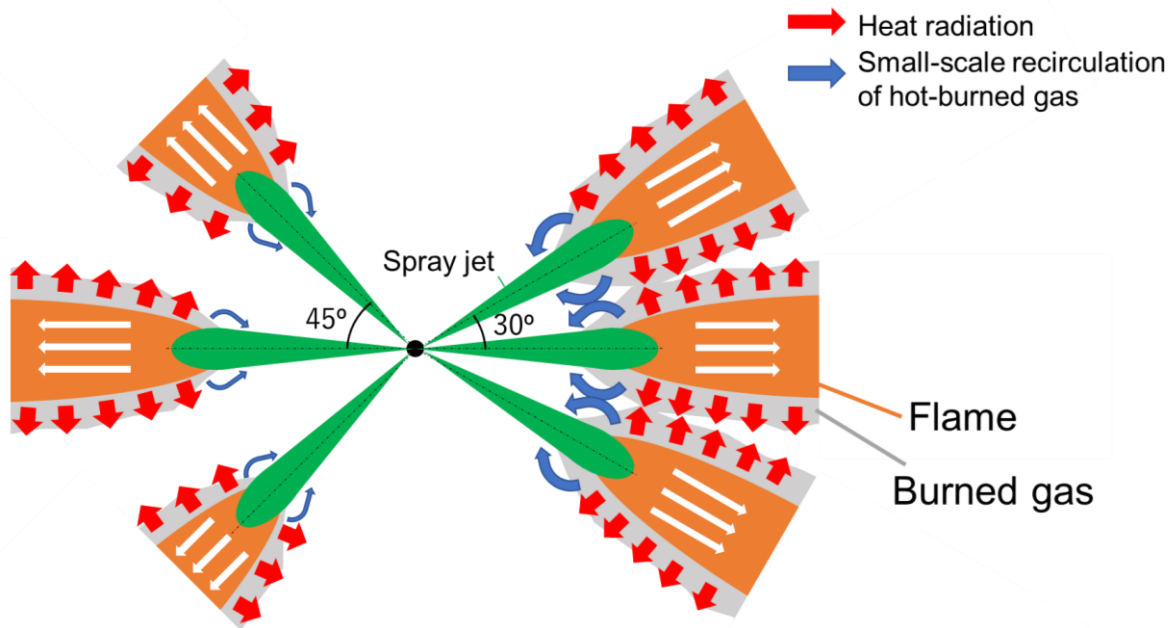


Figure 3.37 Structure of diesel spray and flame characteristic, and effect of a small-scale recirculation of hot-burned gas in different jet-jet angle

Through this study, how the liquid length and lift-off length appear and factors that can affect them can be summarized as shown in Figure 3.37 by the jet-jet angle that varies depending on the number of injector nozzle hole. The smaller the jet-jet angle, the stronger the backflow from the upstream of the diesel spray flame, which can be seen as the cause of the shortened liquid length and lift-off length. This strong effect of backflow was more evident in atmospheric conditions such as oxygen concentration than in injection conditions such as injection pressure or nozzle orifice diameter. Through this, if the jet-jet angle becomes smaller than a certain level, a strong backflow occurs regardless of the surrounding atmospheric conditions. Due to this, it is newly found that the diesel spray flame near the upstream can have a sufficient effect on the liquid part to create the effect of shortening the lift-off length.

3.4 Summary

Aiming to reveal the diesel combustion phenomena with a narrow jet-jet angle and to elucidate the relationship between lift-off length and liquid length under realistic diesel engine conditions, experiments were conducted using an optical accessible RCEM equipped with a custom-made asymmetric six-hole nozzle having jet-jet angles of 30° and 45°. High-speed direct photo imaging with a Mie scattering method and high-speed OH* chemiluminescence imaging were applied to capture the evolution of the spray flame, including lift-off length and liquid length. The effect of injection pressure, nozzle hole diameter, and oxygen concentration were investigated. The following conclusions were reached:

1. The liquid length before ignition is similar irrespective of the jet-jet angle. After ignition, in the case of the larger jet-jet angle, the liquid and lift-off length slowly decrease. However, the liquid and lift-off length of the narrower jet-jet angle rapidly and simultaneously decrease.
2. When lowering the injection pressure or decreasing the nozzle diameter, in the case of the narrower jet-jet angle, the lift-off length decreases first, then the liquid length decreases. When the oxygen concentration is lower, the liquid length does not change according to the jet-jet angle. However, the narrower jet-jet angle significantly decreases the lift-off length. The observed tendencies of the liquid and lift-off length are able to be interpreted by the entrainment of hot-burned gas owing to small-scale recirculation.
3. The smaller jet-jet angle, the faster the backward flow velocity, and this phenomenon was larger in the combustion condition. As the ignition of the pre-mixer formed in the downstream of the diesel spray starts, the air in combustion chamber expands and the flow is momentarily directed toward the injector tip. At this time, if the same amount of air is pushed between the sprays, the smaller the gap between the sprays, the faster the pushing speed. Therefore, it can be determined that the backward flow velocity changes significantly compared to the entrainment velocity.

From this research, it has been newly discovered that, when the jet-jet angle of the injector becomes smaller than a certain level, a strong backflow occurs between the spray jets, and the diesel spray flame near the upstream has a sufficient effect on the liquid part regardless of the ambient atmospheric conditions, thereby shortening the lift-off length. Therefore, it is possible to maximize the thermal efficiency while reducing the formation of a large amount of soot by designing the distance between the number of holes in the injector and the diesel spray accordingly, and designing the flow inside the combustion chamber not to occur centered on the injector.

Representative nomenclature

θ : Crank angle

$dQ/d\theta$: Heat release rate

p : In-cylinder pressure

α : Jet-jet angle

p_{inj} : Injection pressure

r_{O_2} : Oxygen concentration

d_N : Nozzle orifice diameter

dN : Distance from the nozzle

β : angle from the main diesel spray axis

References

- [1]. Kimura, S., Aoki, O., Ogawa, H., Muranaka, S. et al., "New Combustion Concept for Ultra-Clean and High-Efficiency Small DI Diesel Engines," SAE Technical Paper 1999-01-3681, 1999, doi:10.4271/1999-01-3681.
- [2]. Reitz, R. D., Ogawa, H., Payri, R. et al., "IJER editorial: The future of the internal combustion engine" *Int. J. Engine Research* 21(1):3-10, 2020, doi:10.1177/1468087419877990.
- [3]. Tanin, K., Wickman, D., Montgomery, D., Das, S. et al., "The Influence of Boost Pressure on Emissions and Fuel Consumption of a Heavy-Duty Single-Cylinder D.I. Diesel Engine," SAE Technical Paper 1999-01-0840, 1999, doi:10.4271/1999-01-0840.
- [4]. Funayama, Y., Nakajima, H. and Shimokawa, K., "A Study on the Effects of a Higher Compression Ratio in the Combustion Chamber on Diesel Engine Performance," SAE Technical Paper 2016-01-0722, 2016, doi:10.4271/2016-01-0722.
- [5]. Kim, B., Yoon, W., Ryu, S. and Ha, J., "Effect of the Injector Nozzle Hole Diameter and Number on the Spray Characteristics and the Combustion Performance in Medium-Speed Diesel Marine Engines," SAE Technical Paper 2005-01-3853, 2005, doi:10.4271/2005-01-3853.
- [6]. Pierpont, D. and Reitz, R., "Effects of Injection Pressure and Nozzle Geometry on D.I. Diesel Emissions and Performance," SAE Technical Paper 950604, 1995, doi:10.4271/950604.
- [7]. Sibendu, S., Anita I. R., Douglas E. L., Suresh A., "Effect of nozzle orifice geometry on spray, combustion, and emission characteristics under diesel engine conditions", *Fuel* 90(3):1267-1276, 2011, doi:10.1016/j.fuel.2010.10.048.
- [8]. Matsson, A., Jacobsson, L. and Andersson, S., "The Effect of Elliptical Nozzle Holes on Combustion and Emission Formation in a Heavy-Duty Diesel Engine," SAE Technical Paper 2000-01-1251, 2000, doi:10.4271/2000-01-1251.
- [9]. Numata A., Kumagai T., Nagae Y. and Osafune S., "Increase of Thermal Efficiency and Reduction of NO_x Emissions in DI Diesel Engines", *Mitsubishi Heavy Industries, Ltd. Technical Review* 38(3):136-140, 2001.
- [10]. Bergstrand, P. and Denbratt, I., "Diesel Combustion with Reduced Nozzle Orifice Diameter," SAE Technical Paper 2001-01-2010, 2001, doi:10.4271/2000-01-2010.
- [11]. Horibe, N., Komizo, T., Mamizuka, Y., Sumimoto, T., Kawanabe, H., Ishiyama, T., "Analysis of Mixture Formation Process in a Diesel Engine with Post Injection," SAE Technical Paper 2015-01-1836, 2015, doi:10.4271/2015-01-1836.
- [12]. Clément, C., Ulf A., Öivind, A., Rolf, E., Bengt Johansson, "Influence of jet-jet interactions on the lift-off length in an optical heavy-duty DI diesel engine", *Fuel* 112:311-318, 2013, doi:10.1016/j.fuel.2013.05.021.
- [13]. Higgins, B. and Siebers, D., "Measurement of the Flame Lift-Off Location on DI Diesel Sprays Using OH Chemiluminescence," SAE Technical Paper 2001-01-0918, 2001, doi:10.4271/2001-01-0918.

- [14]. Toda, N., Yamashita, H., Mashida, M., "PTV analysis of the entrained air into the diesel spray at high-pressure injection", Proc. SPIE 9232, *International Conference on Optical Particle Characterization* 92320C, 2014, doi: 10.1117/12.2063632.
- [15]. Fuyuto, T., Hattori, Y., Yamashita, H., and Mashida, M., "Backward Flow of Hot Burned Gas Surrounding High-Pressure Diesel Spray Flame from Multi-hole Nozzle," *SAE Int. J. Engines* 9(1):71-83, 2016, doi:10.4271/2015-01-1837.
- [16]. Fuyoto, T., Hattori, Y., Yamashita, H., Toda, N., Mashida, M., "Set-off length reduction by backward flow of hot burned gas surrounding high-pressure diesel spray flame from multi-hole nozzle", *Int. J. Engine Research* 18(3):173-194, 2016, doi:10.1177/1468087416640429.
- [17]. Bazyn, T., and Koci, C., "The Effect of Jet Spacing on the Combustion Characteristics of Diesel Sprays," Proceedings of THIESEL 2014 C.2.4, 2014.
- [18]. 藤本元, 田辺秀明, 國吉光, 佐藤豪, ディーゼル噴霧の性状に関する研究, 日本機械学会論文集 (B編) 47 卷 418 号
- [19]. Siebers, D. and Higgins, B., "Flame Lift-Off on Direct-Injection Diesel Sprays Under Quiescent Conditions," SAE Technical Paper 2001-01-0530, 2001, doi:10.4271/2001-01-0530.
- [20]. Siebers, D., "Liquid-Phase Fuel Penetration in Diesel Sprays," SAE Technical Paper 980809, 1998, doi:10.4271/980809.
- [21]. Yamauchi, J., Dong, P., Nishida, K., and Ogata, Y., "Effects of Hole Diameter and Injection Pressure on Fuel Spray and Its Evaporation Characteristics of Multi-Hole Nozzle for Diesel Engine," SAE Technical Paper 2017-01-2305, 2017, doi:10.4271/2017-01-2305.

Chapter 4. Analysis of the Relationship between Near-wall Velocity Distribution and Wall Heat Flux by a Diesel Spray Flame Impingement

4.1 Introduction

Nowadays, there are strong regulations on exhaust gas emitted from internal combustion engine worldwide. In order to satisfy a strong regulation on a diesel engine, it is necessary to increase the thermal efficiency of a diesel engine. To increase the thermal efficiency of a diesel engine, it is necessary to reduce the exhaust loss and the cooling loss. To reduce the exhaust loss, the increasing the compression ratio the shortening the combustion duration is necessary. In order to increase the compression ratio, the size of the combustion chamber is reduced. In order to reduce the combustion duration, it is necessary to inject a large amount of the fuel in a short time by increasing the fuel injection pressure or by increasing the number of nozzle holes in the injector. In order to reduce the cooling loss in the combustion process, it is necessary to reduce the contact area of the injected fuel after it impinges to the combustion chamber wall and to reduce the velocity at the combustion chamber wall. However, increasing the injection pressure or increasing the number of nozzle holes in the injector, which has been introduced as a method to reduce the combustion duration, trade-off with the method to reduce cooling loss. Therefore, to understand this trade-off relationship, it is necessary to know the relationship between the diesel spray flow near the wall and the heat flux at the wall.

For this purpose, a various study has been conducted on the relationship between a flow characteristic near the wall and the heat transfer at the wall. Katsura et al. [1] studied the flow characteristics that appear after the diesel spray impinges to the flat wall. The closer the distance between the injector tip and the wall of the combustion chamber, the greater the density of droplets after the diesel spray impinges to the wall. In addition, as the injection pressure and the ambient density increased, the droplet density decreased. Li et al. [2] analyzed the heat flux at a various point on the wall when the diesel spray flame impinges to the combustion chamber wall. As the spray tip reached the wall, the local heat flux at that location began to rise. Also, as the injection pressure increased, the peak value of the local heat flux and the rate of rise increased. Zama et al. [3] analyzed the velocity distribution near the wall after the diesel spray impinges to the wall. The average peak velocity of the spray flow region near the wall decreased as the ambient gas density increased and the injection pressure decreased. It was also found that the average peak velocity was correlated with the spray center velocity. Rizal et al. [4] conducted a study on how the heat flux appears according to the injection pressure and the impingement distance. High injection pressure activates high convection from the spray motion, resulting in improved heat transfer when diesel spray impinges to the wall. However, most of the studies were conducted in constant volume vessel. So, it is necessary to consider

the actual engine situation which the volume and pressure change in time variation.

In this study, the velocity distribution of the diesel spray near the wall of the combustion chamber and the heat flux at the wall of the combustion chamber were investigated to clarify the relationship between the flow near the wall and the heat flux through the wall in actual engine situation. For this purpose, a real engine situation was implemented using a rapid compression and expansion machine (RCEM). The velocity distribution of the diesel spray appearing near the wall was measured through the particle image velocimetry (PIV) method, and the heat flux was calculated by measuring the real-time wall temperature by installing a multi-point temperature sensor at the location of the combustion chamber wall where the diesel spray impingement.

4.2 Experimental setup

4.2.1 Experimental Apparatus

An experiment was conducted using a RCEM as Figure 4.1, which has a quasi-two-dimensional cavity-shaped combustion chamber, in our previous study [5]. The specification of the RCEM is shown in Table 4.1. The bore and stroke are 85 mm and 96.9 mm, respectively, and the compression ratio is 14.6. A diesel-like solvent was injected from a single-hole injector with a nozzle diameter of 0.133 mm, because the diesel fuel had formed too bright luminous flame and the luminous flame had covered the scattering light for the PIV.

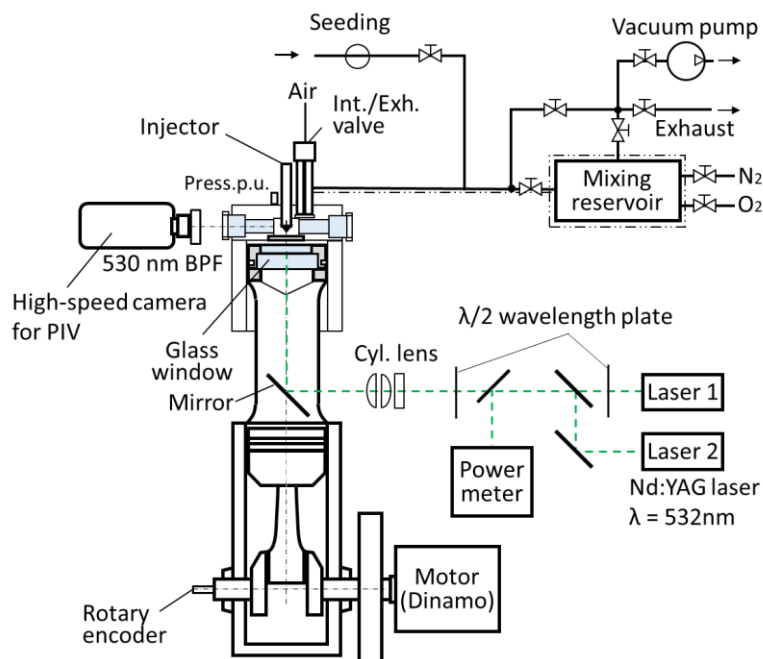


Figure 4.1 Schematic diagram of the RCEM

Table 4.1 Specification of the RCEM

Bore × Stroke	85 mm × 96 mm
Displacement	$0.550 \times 10^{-3} \text{ m}^3$
Compression ratio	14.6
Injection system	Common rail system

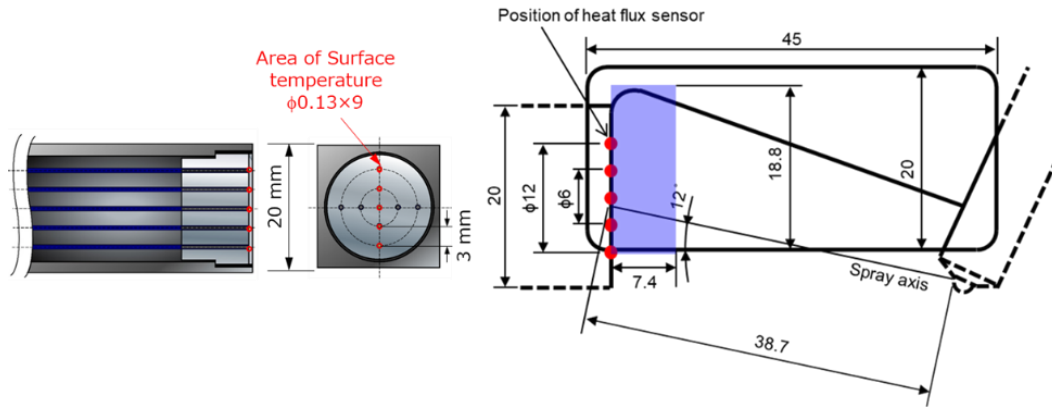


Figure 4.2 Multi-point temperature sensor and a schematic diagram of the combustion chamber

The multi-point temperature sensor was installed in the combustion chamber wall where the diesel spray flame impinges. Figure 4.2 shows the shape of the combustion chamber, the imaging area for the PIV, and the multi-point temperature sensor. The multi-point temperature sensor was composed of aluminum alloy (AC8A) - constantan thermocouple, the body material was used AC8A same as a general diesel engine piston material and 1 μm thickness aluminum alloy thin film was formed on the surface of the body. The nine surface junctions of this sensor were arranged in cross-shape at 3 mm intervals (junction size $\phi 130 \mu\text{m}$) and one point of inside temperature with a depth of 4.5 mm can be measured at the same time. The measurement point No.3 which the center position of the multi-point temperature sensor was matching with the diesel spray axis. It was confirmed that the response speed of this sensor had 10 kHz or higher. To analyze the heat flux at each surface junction, the heat conduction equation in a two-dimensional cylindrical coordinate (4.1) and the heat flux calculation equation (4.2) using the measured surface and internal temperature as boundary conditions were used.

$$\frac{\partial T}{\partial t} = \frac{\lambda}{\rho c} \left\{ \frac{1}{r} \frac{\partial}{\partial r} \left(r \frac{\partial T}{\partial r} \right) + \frac{\partial^2 T}{\partial z^2} \right\} \quad \text{Heat conduction equation in 2-D cylinder coordinates} \quad (4.1)$$

$$q_i = \lambda \frac{\partial T}{\partial z} - \lambda \frac{1}{r} \frac{\partial}{\partial r} \left(r \frac{\partial T}{\partial r} \right) + \rho c \frac{\partial T}{\partial t} \quad \text{Heat flux calculation} \quad (4.2)$$

Experiments were conducted under following conditions as Table 4.2. The cranking speed was 900 rpm, the in-cylinder pressure and temperature at the injection timing of -6.5°ATDC were 8 MPa and 800 K, the intake oxygen concentration was 15% and 0% for combustion and non-combustion situation, the injection amount was 10.2 mg, and the injection pressures was 120, 90, and 60 MPa.

Table 4.2 Experiment conditions

Cranking speed	900 rpm
Nozzle-hole diameter	0.133 mm
Injection quantity	10.2 mg (13.7 mm ³)
Start of injection (SOI)	-5.9° ATDC
In-cylinder pressure @ SOI	8 MPa
In-cylinder temperature @ SOI	800 K
Injection pressure	120, 90, 60 MPa
Fuel	Solvent (Cetane number: 57), n-C ₁₁ H ₂₄ , n-C ₁₂ H ₂₆ , and iso-C ₁₂ H ₂₆
Composition of the intake gas	O ₂ : 15 mol%, N ₂ : 85 mol% (Combustion) N ₂ : 100 mol% (Non-combustion)

4.2.2 Imaging condition

The distribution of diesel spray velocity near the wall was measured by PIV method. The imaging conditions are shown in Table 4.3. For PIV, a 2nd harmonic generation Nd:YAG laser with a wavelength of 532 nm was used, and the interval between the lasers could be set as short as 4 μs through a two laser devices. A high-speed camera was used for imaging, and a bandpass filter of 530 ± 10 nm was used to take an image of the scattered laser for PIV. The spatial resolution of the image was 33 $\mu\text{m}/\text{pixel}$. As a tracer for the PIV, a SiO₂ porous particle (Godd-ball) with an average diameter of 10 μm was used. When PIV analysis, the Multi-pass interrogation method algorithm was used. The interrogation window and the overlap for PIV analysis were 16×16 pixels and 50%, respectively, which was suitable for the velocity range in the high-temperature region. On the wall of the combustion chamber, the closest measured position through the PIV was 0.4 mm from the wall.

Table 4.3 Imaging condition of PIV and OH* chemiluminescence

PIV	Exposure time	13.571 μ s
	Bandpass filter	530 \pm 10 nm
	Spatial resolution	33 μ m/pixel
	Frequency	20 kHz
	Interval 1st,2nd	6 μ s
	Laser wavelength	532 nm
	PIV tracer	Godd ball (SiO ₂): 10 μ m
	Analyzing algorithm	Multi-pass interrogation
	Interrogation window	16 \times 16 pixels
	Overlap	50 %

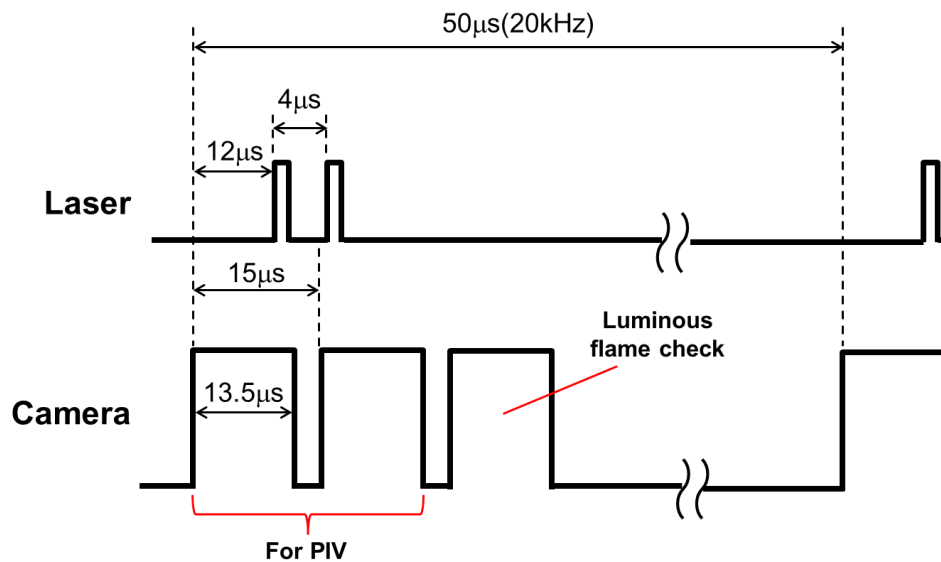


Figure 4.3. Signal sequence for the PIV

Figure 4.3 shows the signal sequence of the laser and high-speed camera for the PIV. The shutter of a high-speed camera opens three times per cycle. When the first and second shutter is opened, the laser was incident at an interval of 4 μ s and image was taken for the PIV. When the third shutter was opened, the laser was not incident, in order to observe the luminous flame generated when experiment the combustion conditions and to discriminate the non-measurable area.

4.3 Results and discussion

4.3.1 Analysis of the velocity distribution and heat flux on the combustion chamber wall in non-combustion situation

First, to clarify the relationship between velocity distribution and heat flux near on the combustion chamber wall, the non-combustion situation was experimented. Figure 4.4 (a) shows the in-cylinder pressure, and the temperature and the heat flux on the combustion chamber wall in non-combustion situation when the injection pressure was 90 MPa. The No.3 position of the temperature sensor was matching with a center of the diesel spray and distance interval of each position was 3 mm. Figure 4.4 (b) shows the velocity distribution result by PIV in each moment of yellow line in Figure 4.4 (a). When the crank angle was -1.87°CA , this moment shows when the diesel spray impinges to the wall. After that moment, diesel spray has a quasi-steady state.

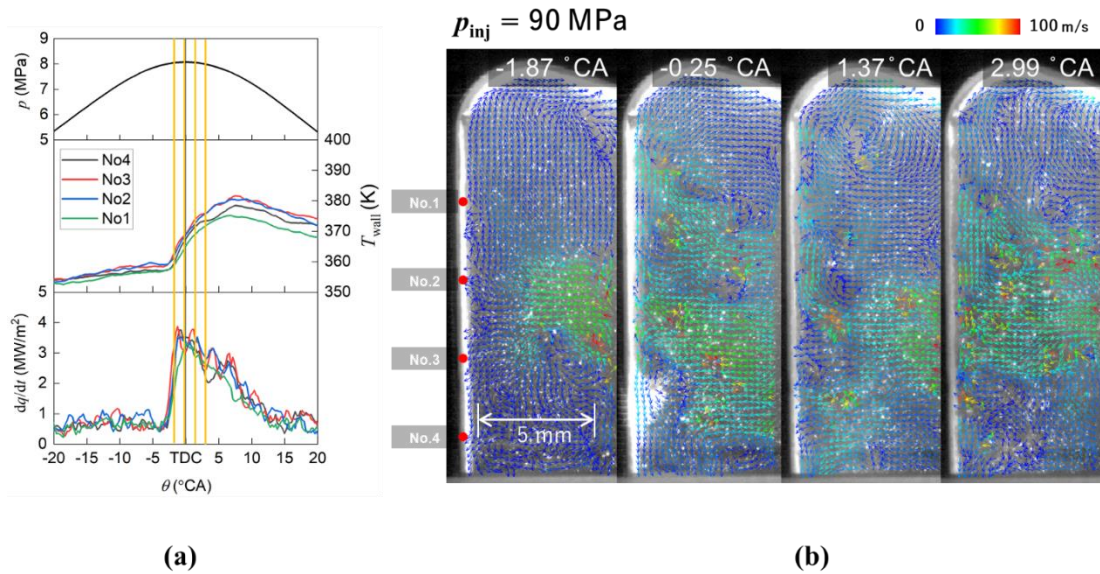


Figure 4.4 In-cylinder pressure, and temperature and heat flux on the combustion chamber wall at each position in non-combustion situation on $p_{\text{inj}} = 90$ MPa (a) and the PIV result (b) in each moment

From the result in Figure 4.4 (a), it can be seen that the temperature in No.3 position on the wall, which the center of the diesel spray, was increasing first, after that the temperature of the other position was increasing. The heat flux result shows a same trend with the temperature result. Comparing this result with the PIV result, it can be seen that the diesel spray impinging to the wall affect to the temperature trend on the combustion chamber wall. In PIV result, a moment when the diesel spray impinging to the wall, the temperature of the combustion chamber wall increases, and the heat flux

increased rapidly. Since the central part of the diesel spray impinges to the wall first, the temperature of the wall of the combustion chamber at the same location also rises first. After that, the temperature of the wall of the combustion chamber at No.2 and No.4 positions close to the center of the diesel spray was shown to rise. This showed that the temperature of the wall of the combustion chamber increased as the diesel spray impinged to the wall, as shown in the previous study. In order to analyze the flow characteristic, which it can affect the heat transfer to the wall, the velocity distribution near the wall was measured by the PIV. And, the velocity factor was divided into 2 directions, the perpendicular direction to the wall and the direction parallel to the wall.

Figure 4.5 shows the velocity change over time at each position in different direction which the perpendicular to the wall and the parallel to the wall, respectively. When the velocity direction near the wall was parallel to the wall, the moment when the heat flux increases in No.1, No.2, and No.4 similar with the moment when the velocity increases. In addition, a fluctuation of the heat flux and a fluctuation of the velocity were similarly shown. However, the velocity result at the No.3 position, which is the diesel spray axis position, were randomly appeared. Because, after the diesel spray impinges to the wall, the ambient air flow characteristics are affected by the tumble flow according to the movement of the piston in an actual engine, unlike the condition of the constant volume vessel. After all, since the flow of the diesel spray is affected by the tumble flow inside the combustion chamber, it is difficult to maintain a steady flow characteristic in the central portion in an actual engine situation. Therefore, it is not easy to explain the high heat flux at the center of the diesel spray with the velocity distribution parallel to the wall. To this end, a comparison of the velocity factor in the perpendicular direction to the wall and the heat flux results in the wall was also conducted. When looking at the velocity factor results in the perpendicular direction, the velocity at the center of the diesel spray was the highest, suggesting that this result was correlated with the result of high heat flux at the center. In addition, the interesting result shows in the No.4 graph. When looking at the heat flux result of No.4, a fluctuation of heat flux appeared like a valley shape. The fluctuation of velocity factor also, which the perpendicular direction to the combustion chamber wall, showed a valley shape similar with the heat flux shape. Based on these results, it is possible to explain the relationship between the velocity distribution and the heat transfer near the wall by considering the velocity in the perpendicular direction as well as the velocity in the parallel direction to the wall.

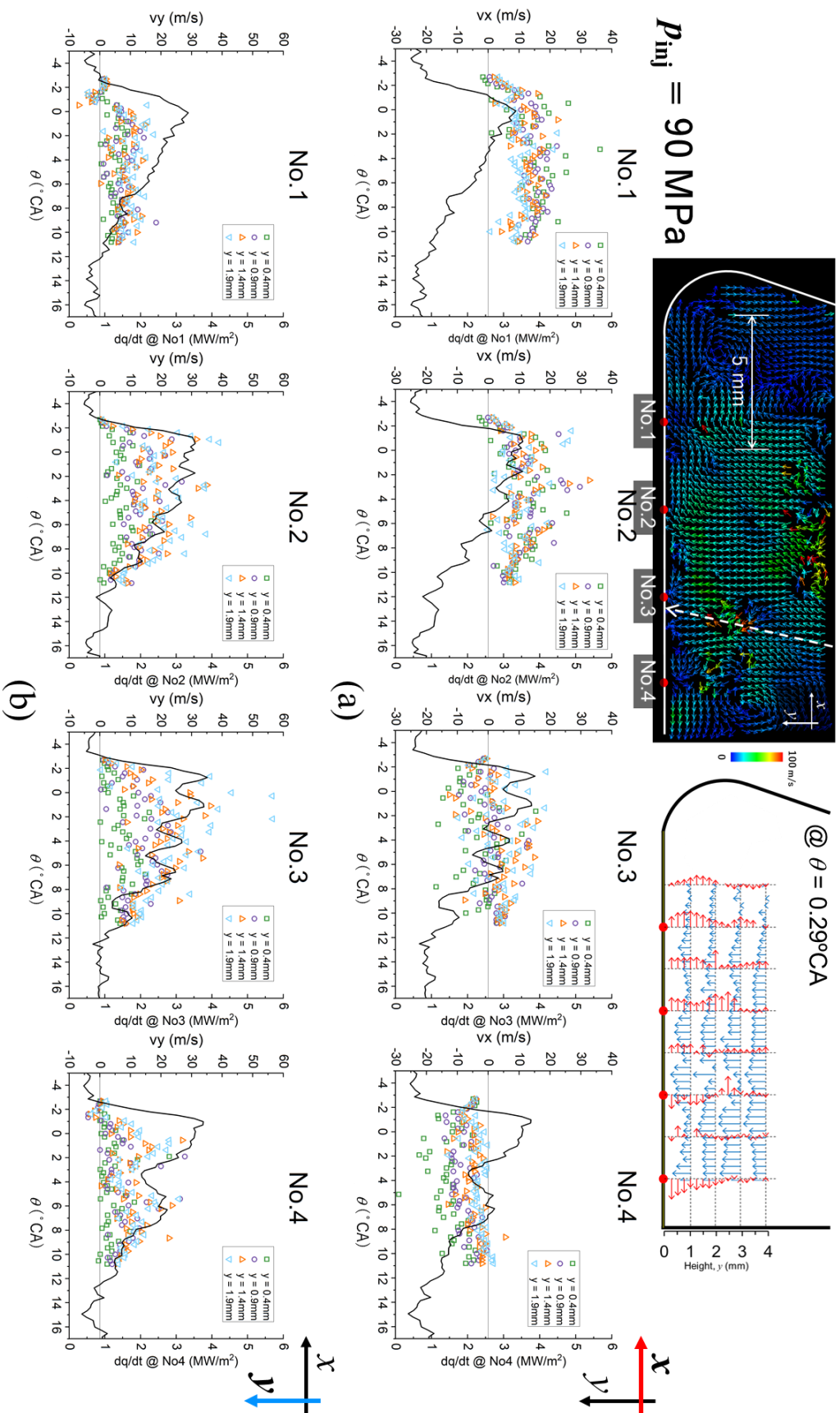


Figure 4.5 Velocity change over time at each position in different direction which parallel to the wall (a) and the perpendicular to the wall (b) in non-combustion situation on $p_{inj} = 90 \text{ MPa}$

As mentioned earlier, it is difficult to explain the relationship between the heat flux and the velocity distribution only in the parallel direction of flow near the wall in an actual engine situation. Therefore, in order to clarify the relationship between the heat flux and the flow characteristics of the combustion chamber wall in an actual engine situation, it is necessary to consider not only the parallel direction of the flow, but also the perpendicular direction of the flow. In this study, based on the fact that the heat flux increases as the perpendicular direction velocity increases, it is assumed that a high transport coefficient occurs due to the shear flow with a high vortex viscosity coefficient near the wall. In addition, it was considered that the high transport coefficient formed near the wall causes a high heat transfer to the combustion chamber wall. In order to explain the relationship between the heat flux and the transport coefficient on the combustion chamber wall, the distribution of the absolute value of the velocity gradient tensor, $|S|$, in a two-dimensional velocity field was obtained and compared with the heat flux on the combustion chamber wall. A high transport coefficient is indicated by a high vortex viscosity coefficient. The vortex viscosity coefficient can be calculated by the following Equation (4.3), where the C_S is a constant and the Δ is the grid size. Therefore, the vortex viscosity coefficient can be estimated with the velocity gradient tensor.

$$\nu_e = (C_S \Delta)^2 |\bar{S}| \quad (4.3)$$

And, to calculate the absolute value of the velocity gradient tensor, it was obtained through the following calculation Equation (4.4).

$$S_{ij} = \frac{1}{2} \left(\frac{\partial u_i}{\partial x_j} + \frac{\partial u_j}{\partial x_i} \right), \quad |S| = (S_{ij} \cdot S_{ij})^{1/2} \quad (4.4)$$

From this calculation, the distribution of the velocity gradient tensor was analyzed and compare with the heat flux on the combustion chamber wall. Figure 4.6 shows the velocity gradient tensor distribution and the heat flux in each position of the combustion chamber wall when the injection pressure was 90 MPa in non-combustion situation. The image above in Figure 4.6 shows the velocity gradient tensor at each crank angle. The magnitude of the velocity gradient tensor can be known through the color of the image. The graph below in Figure 4.6 shows the heat flux at each sensor position. It can be seen that the position where the heat flux appears high in the heat flux graph is the same as the position where the velocity gradient tensor near the wall is high in the image above. From this result, it was found that the heat flux was high in the region where the velocity gradient tensor distribution near the wall was high. This result supports the assumption that the high transport coefficient of the flow affects the heat transfer phenomenon of the combustion chamber wall. This means that the heat flux of the combustion chamber wall is high in the region where the shear flow

characteristic is strong. After that, this study analyzed how this phenomenon appears when the injection pressure is changed.

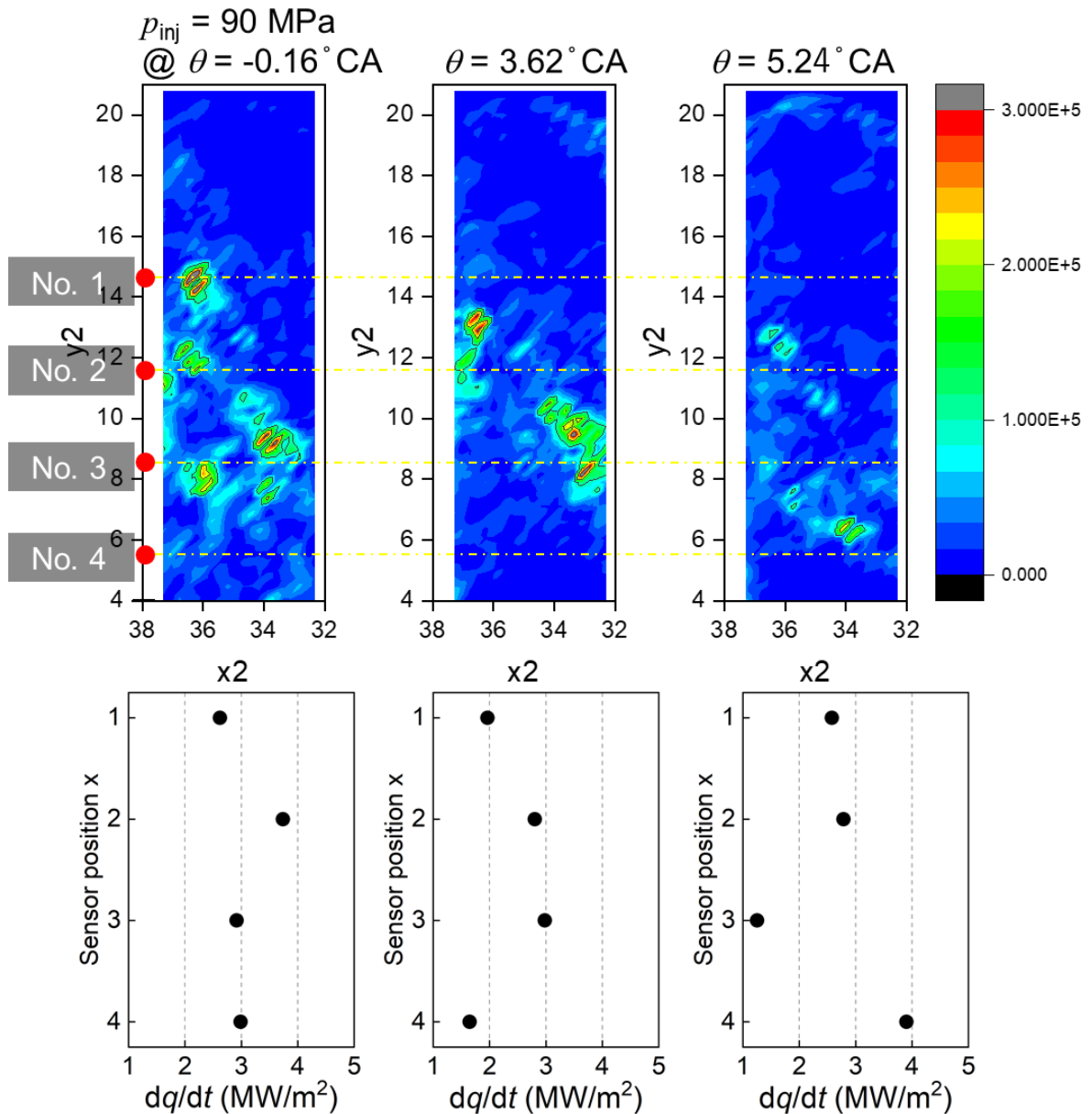


Figure 4.6 Result of the velocity gradient tensor distribution and the heat flux in each position of the combustion chamber wall on $p_{inj} = 90$ MPa over time in non-combustion situation

Figure 4.7 shows the velocity gradient tensor distribution and the heat flux in each position of the combustion chamber wall when the injection pressure was 120, 90, 60 MPa, respectively, in non-combustion situation. As shown in previous studies, it was shown that the higher the injection pressure, the faster the diesel spray velocity and the higher the turbulence. As a result, as the injection pressure

increased, the velocity gradient tensor distribution also appeared high. In addition, the phenomenon of high heat flux when the injection pressure was high could be explained by the high velocity gradient tensor of the corresponding region. Based on this, it was found that the shear flow characteristic changed according to the injection pressure, and thus the heat flux of the combustion chamber wall was also affected.

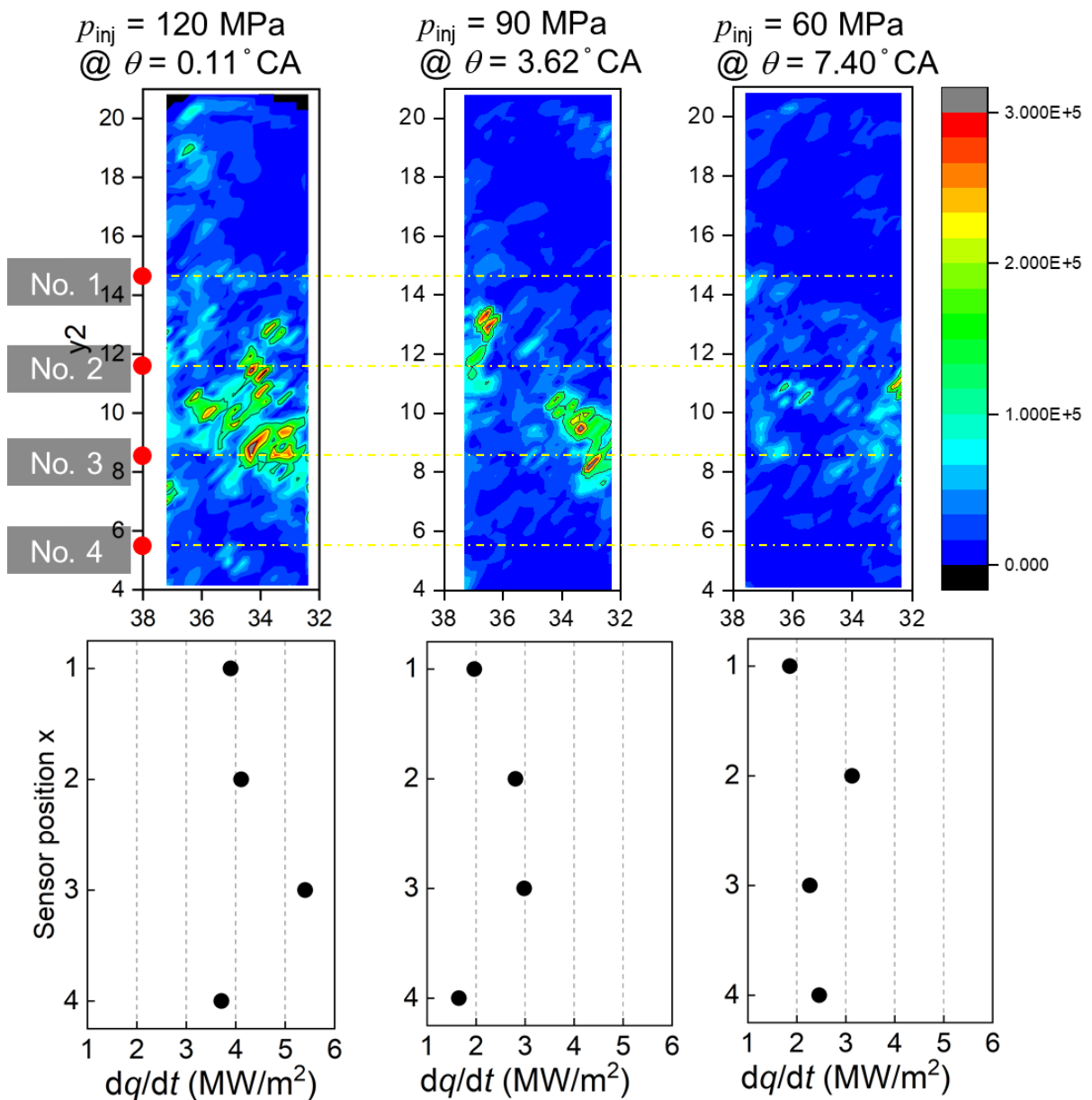


Figure 4.7 Result of the velocity gradient tensor distribution and the heat flux in each position of the combustion chamber wall on $p_{inj} = 120, 90, 60$ MPa in non-combustion situation

4.3.2 Analysis of the velocity distribution and heat flux on the combustion chamber wall in combustion situation

Based on the results in the non-combustion situation, the relationship between the heat flux at the combustion chamber wall and the flow characteristics near the wall was analyzed. A same experiment was conducted in a combustion situation. Figure 4.8 shows the in-cylinder pressure, heat release rate, temperature and heat flux on the combustion chamber wall, and the PIV result in different injection pressure.

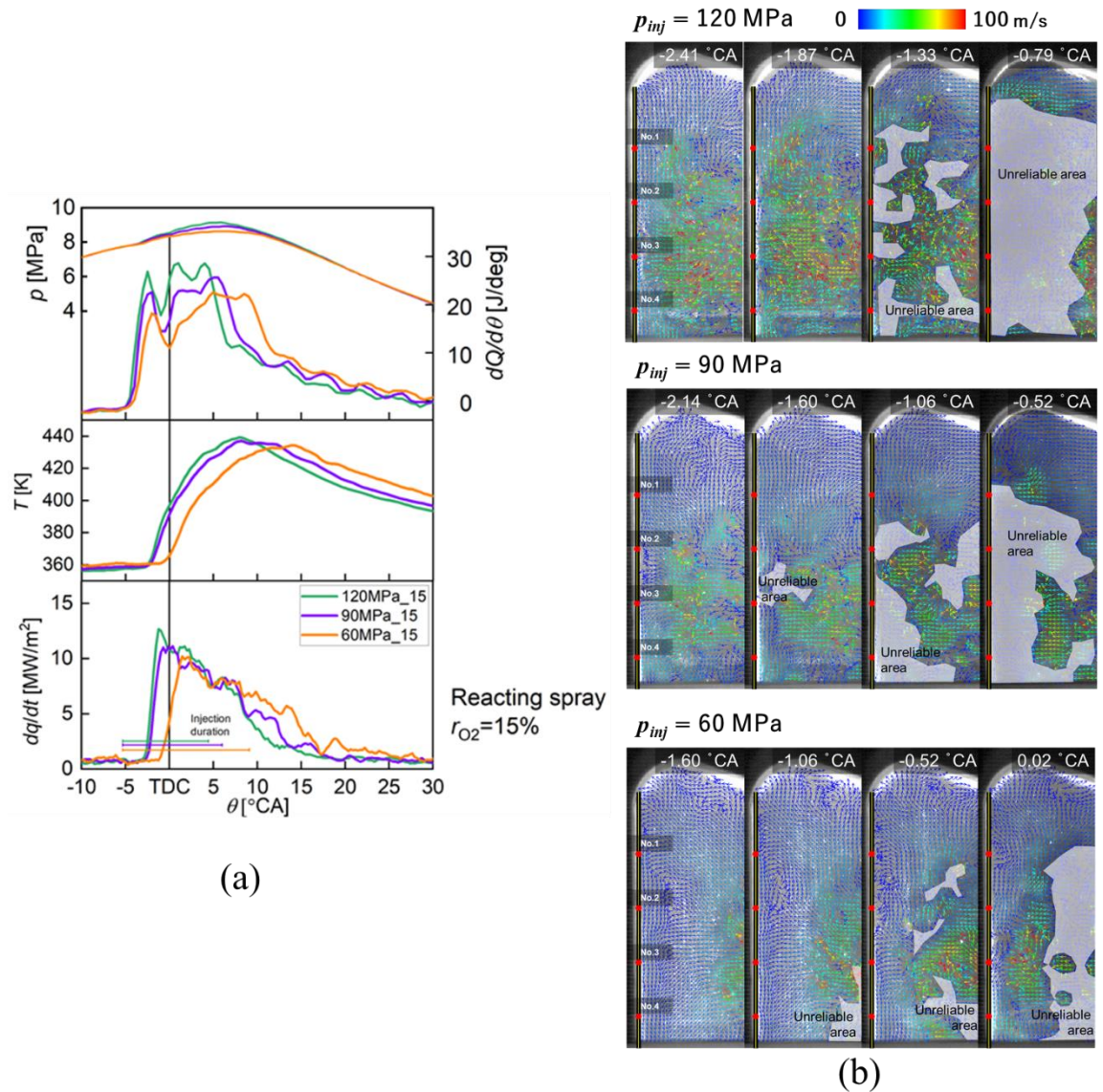


Figure 4.8 Result of the in-cylinder pressure, heat release rate, temperature and heat flux on the combustion chamber wall (a), and PIV result (b) in different injection pressure ($p_{inj} = 120, 90, 60$ MPa)

As in the previous non-combustion situation, when the injection pressure was high, the diesel spray velocity was also high. Accordingly, it can be seen that the moment when the temperature and heat flux of the combustion chamber wall rise was advanced in high injection pressure condition. Also, in the PIV result, when looking at the moment when the diesel spray impinges to the combustion chamber wall in high injection pressure condition, the increasing of velocity distribution near on the wall appears earlier. However, a luminous flame appears in the combustion situation. So, when the luminous flame appeared, the PIV tracer was covered and the unreliable area where a measuring the velocity is impossible region was appeared. Therefore, the velocity distribution up to the moment the diesel spray impinges to the combustion chamber wall can be measured, but it is difficult to measure after the quasi-steady state because of the luminous flame formed. For this reason, the velocity factor and heat flux near the combustion chamber wall up to the moment when velocity measurement is possible were compared and analyzed.

Figure 4.9 shows the velocity change over time at each position in different direction which perpendicular to the wall and the parallel to the wall in combustion situation when the injection pressure was 90 MPa. As in the case of non-combustion, the velocity in the parallel to the wall appears randomly at the No.3 position corresponding to the center of the diesel spray. And, the velocity distribution in the perpendicular direction also showed the highest in the center part of the diesel spray in the non-combustion situation as well, and showed a downward trend toward the periphery. As a result, it was not possible to accurately measure the velocity after the appearance of the luminous flame in the combustion situation, but it was found that the velocity measurement results up to the moment the diesel spray impinged to the wall were similar to the non-combustion situation. Based on these results, it can be assumed that the shear flow characteristics near the wall affect the wall heat flux in the combustion situation as in the non-combustion situation. However, since the diesel spray flame, which does not exist in the non-combustion situation, can have an effect on the flow characteristics, it is necessary to analyze and compare the velocity distribution and the heat flux near the wall during combustion.

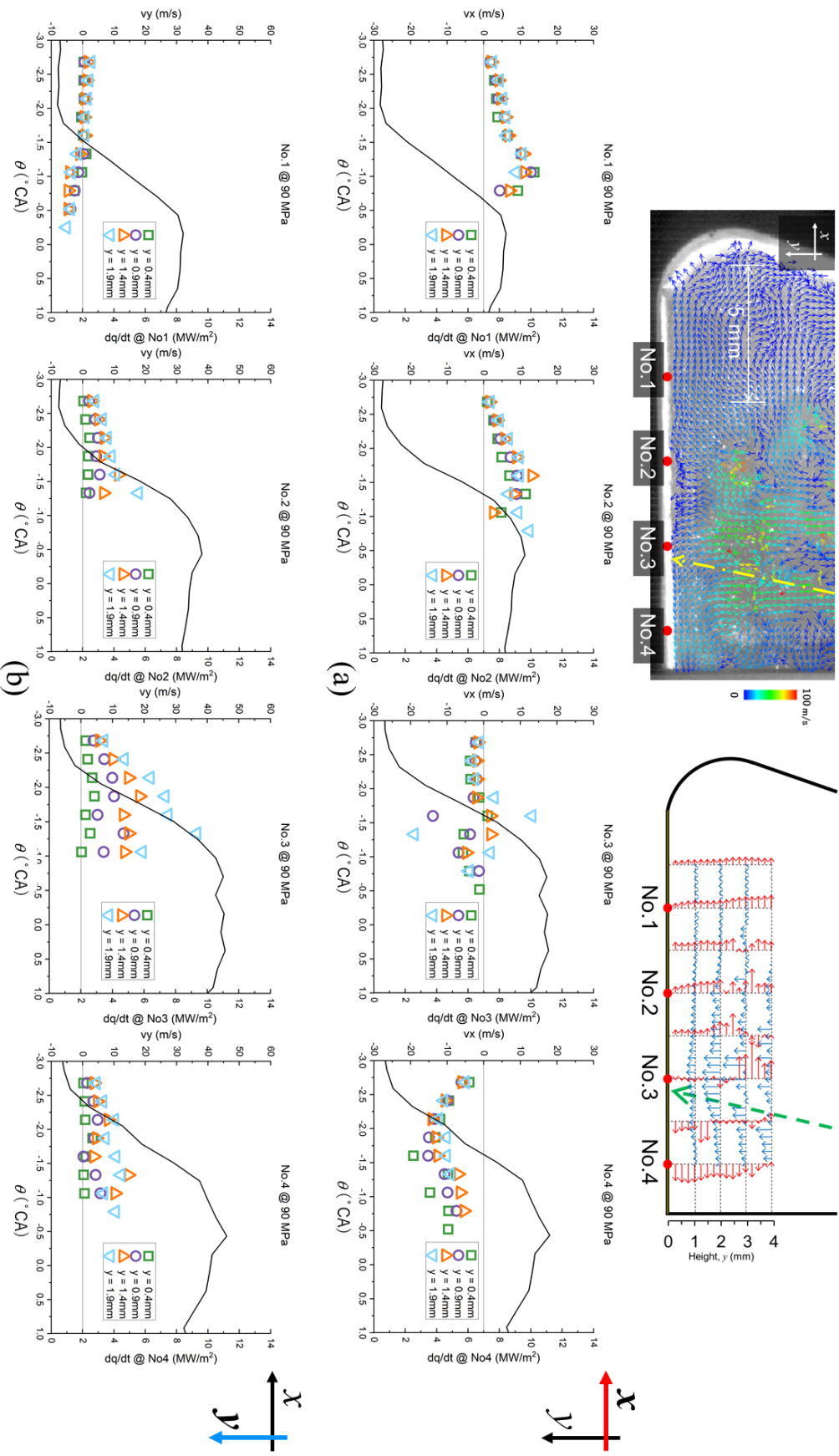


Figure 4.9 Velocity change over time at each position in different direction which parallel to the wall (a) and the perpendicular to the wall (b) in combustion situation on $p_{inj} = 90$ MPa

4.4 Summary

This study focused on the flow velocity and heat flux near the wall depending on the wall position when the diesel spray impinging to the wall of the combustion chamber under different injection conditions. For this purpose, RCEM was used to simulate a realistic engine situation. And, measuring the velocity distribution in the diesel spray near the wall by PIV result and simultaneously measuring the wall heat flux using a multi-point temperature sensor. Based on the measured velocity distribution results, the velocity gradient tensor was calculated and the effect that the shear flow characteristic could have on the wall heat transfer was analyzed. From these results, the following conclusions were reached.

1. The higher the injection pressure, the faster the diesel spray and the moment it impinges to the wall advances. In addition, the higher the injection pressure, the higher the peak value of the heat flux.
2. In the process of decreasing the heat flux, fluctuations were observed, which appeared in line with the timing of fluctuations in the velocity magnitude. From this, it was found that the heat flux at the wall of the combustion chamber is affected by the flow characteristic near the wall.
3. When the velocity gradient tensor and the wall heat flux were compared, it was found that the high heat flux part appeared in high velocity gradient tensor region. This suggests that characteristics of the shear flow near the wall can affect the heat flux.

In the previous study, they tried to analyze the heat transfer characteristics of the wall by focusing on the flow parallel to the wall. In this study, the heat transfer characteristics that can be exhibited by the diesel spray flame on the wall of the combustion chamber were revealed by considering the flow characteristics in the vertical direction as well as the flow characteristics in the parallel direction to the wall. Through this, it was newly found that the flow in the vertical direction sufficiently affects the heat transfer characteristics at the wall, and overall, the shear flow characteristics near the wall have an important influence on the wall heat transfer characteristics. Therefore, it is important to make the diesel spray flame less shear flow characteristic near the wall in order to prevent the loss of cooling due to heat escaping to the wall of the combustion chamber.

References

- [1]. Katsura, N., Saito, M., Senda, J., and Fujimoto, H., "Characteristics of a Diesel Spray Impinging on a Flat Wall," SAE Technical Paper 890264, 1989, <https://doi.org/10.4271/890264>.
- [2]. Li, S., Kamimoto, T., Kobori, S., and Enomoto, Y., "Heat Transfer from Impinging Diesel Flames to the Combustion Chamber Wall," SAE Technical Paper 970896, 1997, <https://doi.org/10.4271/970896>.
- [3]. Zama, Y., Odawara, Y., Furuhashi, T., "Experimental Investigation on Velocity inside a Diesel Spray after Impingement on a Wall", *Fuel* 203, 2017, 757–763, <https://doi.org/10.1016/j.fuel.2017.04.099>
- [4]. Mahmud, R., Kurisu, T., Nishida, K., Ogata, Y., Kanzaki, J., Akgol, O., "Effects of Injection Pressure and Impingement distance on Flat-Wall Impinging Spray Flame and its Heat Flux under Diesel Engine-like Condition" *Advances in Mechanical Engineering*, 2019, Vol. 11(7) 1–15, <https://doi.org/10.1177/1687814019862910>
- [5]. Jo, H., Kawai, Y., Horibe, N., Hayashi, J. et al., "A Study on Diesel Spray Flame by Time-Resolved PIV with Chemiluminescence of OH*," *SAE International Journal of Advances and Current Practices in Mobility*, 4(2):592-601, 2022, <https://doi.org/10.4271/2021-01-1167>.

Chapter 5. Optimizing Urea-Water-Solution Injection Strategy for High Conversion Ratio in After-treatment System

5.1 Introduction

As environmental regulations on internal combustion engines are strengthened worldwide, technologies to reduce emissions are needed for the future of internal combustion engines. The main exhaust gases of diesel engines are PM and nitrogen oxides. In order to reduce them, individual studies are being conducted on methods to reduce them from the combustion stage to the emission stage as a whole. Among the methods of after-treatment of emissions in the exhaust system, there is a method of oxidizing carbon monoxide and hydrocarbons through diesel oxidation catalyst (DOC) and collecting particle matter (PM) through diesel particle filter (DPF). DOC and DPF mostly comprise a Pt catalyst and a substrate of cordierite or SiC, although there are some differences in catalyst composition or substrate characteristics depending on the manufacturer of the automobile or the after-treatment device. The catalyst serves to oxidize THC and CO emissions, and regenerate the trapped PM in DPF. Most of the NO_x emitted from diesel engines is largely NO, but it is converted to NO₂ through DOC and DPF [1, 2]. NO₂ would affect the regeneration process of PM in DPF and NO_x reduction performance of SCR [3, 4]. To reduce NO_x efficiently, it is necessary to control the NO₂ conversion in DOC and DPF. The most representative technologies for reducing NO_x are lean NO_x trap (LNT) and selective reduction catalyst (SCR). The NH₃-SCR system is the most widely used in diesel engine, due to its high efficiency and wide operating temperature range [5]. The hydrocarbons are the alternatives to overcome the disadvantages of the NH₃-SCR reaction [6, 7]; by the adding the hydrocarbon the post-treatment of exhaust gas in the NH₃-SCR catalyst has a high concentration of oxygen [8]. That chemical properties will assist the ammonia to decrease NO_x from diesel engine and increase generation of steam (H₂O) and CO. In this study, the observation of SCR catalysts with vanadium and zeolite material was needed for showed the NH₃/NO_x ratio, NO₂/NO_x ratio, hydrocarbon concentration and NO_x conversion efficiency and HSO (Hydrolysis + SCR + Oxidation catalyst). The experimental studies on the conversion efficiency used to analyze the normal and abnormal NO_x, depending on the gas hourly space velocity (GHSV) and the monolith volume for the oxidation catalysts and VHSO (oxidation + HSO catalysts) SCR systems [9-11]. The SCR system is effective solution for reducing NO_x in a steady-state engine; however still has problem to reduce NO_x emission and produce NH₃ slip in the real operating state [12-16]. Based on this condition, the improvement technologies for increase the Urea-SCR system performance was explained in this study; the controlling amount of urea in the SCR system prevent the NO_x reduction performance, reduce NH₃ slip, and increase the NH₃ adsorption and desorption process [17]. When the amount of UWS into the SCR system increases, the vapor pressure will decrease; the urea droplet temperature suddenly decreases, this reaction produces low evaporation process in the system [18]. The

hydrolysis phenomenon with the various physical models can validate the NH_3 slip quantity in the system based on the evaporation quality [19]. The NO and NO_2 ratio, the SCR temperature, and engine speed condition can affect to the NH_3 slip quantity and NO_x reduction rate [20]. The ratio of NO and NO_2 in the NO_x concentration when entering the system have a direct effect on the SCR system performance; based on that condition, the commercial aftertreatment system adding the DOC and DPF in front of the SCR system [21]. Since the SCR system has highly affected by temperature condition, Pinggen Chen et al. [22] shows the studies to improve the NO_x reduction rate by the analyzing the ratio of NO and NO_2 in the low temperature. The SCR temperature is main factor to reduce NO_x and produce fast chemical-SCR reaction in the system [23].

In this study, the various engine operating conditions will show the performance of DOC, DPF, and SCR system by the reduction of harmful emission such as PM and NO_x from diesel engine. The DOC and DPF are being developed as a natural regeneration DPF suitable for the retrofit market. The DOC and DPF catalyst used in this study were intermediate developments, consisting of Pt and a promoter with a BPT of 285°C . The SCR catalyst is the main material to removes nitrogen oxides from diesel engines using gaseous NH_3 . The UWS injection strategy is used to maximize the NO_x reduction rate and minimize the amount of NH_3 slip. The observation of NH_3 adsorption and desorption mechanism is the important factor to control NH_3 slip and optimizing the NO_x reduction efficiency. The NH_3 adsorption and desorption were analyzed according to engine and catalyst conditions. Based on these results, cause of low NO_x reduction efficiency is analyzed, and the test results are intended for use as basic data for the control logic development of the after-treatment system.

5.2 Experimental setup

5.2.1 Experimental apparatus

In this study, Ssang-yong's in-line 5-cylinder 2696 cc diesel engine was used. Table 5.1 shows the detailed description of the engine's specifications. The valve type of the engine is double overhead camshaft (DOHC). The bore and stroke of each cylinder are 86.2 and 92.4 mm, respectively, and the compression ratio is 17.5. The maximum power of the engine is 191 PS at 4000 rpm, and the maximum torque is 410 N·m when the engine speed is 3000 rpm. The fuel injection system is a common rail, and the environmental regulation that the engine meets is Euro 2. The experiment was carried out under load when the engine speed was 1500, 2000, 2500, and 3000 rpm and the exhaust gas temperature was 250, 300, 350, and 400°C respectively. The reason for setting these conditions is to realize the range of daily driving conditions of diesel engines.

Table 5.1 Test engine specification and target experiment condition

Type	In-line 5
Displacement (cc)	2696
Valve type	Double OverHead Camshaft (DOHC)
Bore × Stroke (mm)	86.2 × 92.4
Compression ratio	17.5
Maximum power (PS)	191/ 4000 rpm
Maximum Torque (N·m)	410/ 3000 rpm
Idle speed (rpm)	780
Injection system	Common-rail injection system
Emission regulation	Euro 2
Model year	2006
Target engine speed (rpm)	1500, 2000, 2500, 3000 rpm
Target exhaust gas temperature (°C)	250, 300, 350, 400°C

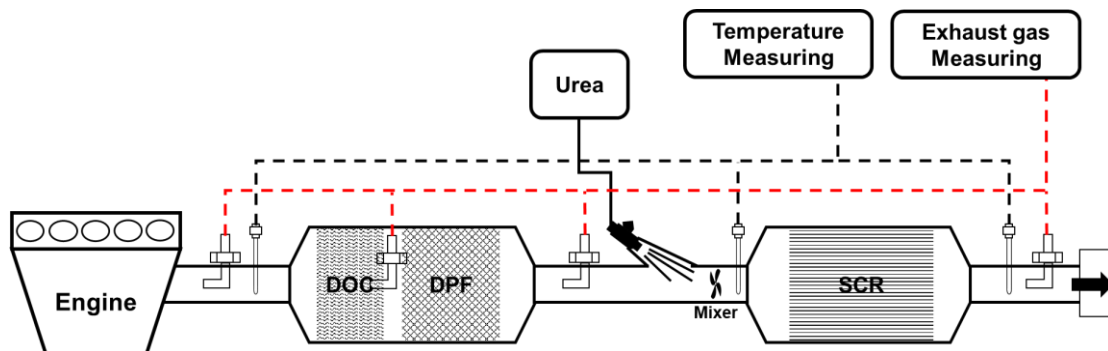


Figure 5.1 Schematic of engine experiment system

An overview of the overall experimental setup is shown in Figure 5.1. The experimental equipment has an engine, and the DOC, DPF, and SCR are installed in the after-treatment system in this order. Specifications for each catalytic unit are given in the Table 5.2. The substrate of DOC and DPF is cordierite and coated with Platinum. The balance point temperature (BPT) of DOC and DPF is 285°C, and the cell density of each catalyst is 400 cpsi and 300 cpsi. The diameter is the same at 5.66 inches, and the length is 4 inches with a DOC and 10 inches with a DPF. In this study, The DOC and DPF were contained in the same case. The substrate of SCR is cordierite, coated with Vanadium base. The cell density of the SCR is 400 cpsi, and the diameter and length are 6.77 inches and 10 inches, respectively. In this study, AOC was not installed because it was necessary to analyze the amount of NH₃ slip according to the urea water injection strategy. The tubes were installed before and after each DOC and DPF and before and after SCR to measure exhaust gas, and a thermocouple was used to measure the temperature. Each tube is connected

to HORIBA's MEXA 1400 QL-NX, an exhaust gas analyzer, and NO, NO₂, N₂O, and NH₃ were measured in real time through this equipment. When measuring exhaust gas, the sampling line was heated to 150°C to prevent PM fouling and NH₃ deposition.

The urea water was sprayed between DOC/DPF and SCR. A mixer is installed at the inlet of the SCR so that the sprayed urea water is uniformly distributed in the SCR. The injection pressure of urea water was maintained at 5 bar and repeated at a rate of 3.3 Hz.

Table 5.2 Specifications of DOC, DPF and SCR

Category	DOC	DPF	SCR
Substrate	Cordierite		
Catalyst	Pt + Promoter / TiO ₂		V-W / TiO ₂
BPT	285°C		-
Cell density	400 cpsi	300 cpsi	400 cpsi
Diameter	5.66 inch	5.66 inch	6.77 inch
Length	4 inch	10 inch	10 inch

5.2.2 Experimental procedure and analysis

The chemical reaction process of general urea-SCR is as follows. The urea water is first decomposed into NH₃ in two steps. As in reaction (5.1), first, HNCO and NH₃ are produced by thermolysis of urea water, and NH₃ and CO₂ are produced by isocyanic acid hydrolysis of HNCO in reaction (5.2). NH₃ produced in this way reacts with nitrogen oxides inside SCR, and the representative reactions are called Standard SCR (5.3), Fast SCR (5.4), and NO₂ SCR (5.5).



Based on this reaction process, the theoretical amount of urea required to reduce NO_x emitted was calculated assuming that the ratio of NH₃ to NO_x was 1:1. The ratio of NO and NH₃ in the standard SCR reaction and the ratio of NO_x and NH₃ in the Fast SCR reaction is 1:1. However, in the NO₂-SCR reaction,

the reaction between NO_2 and NH_3 was not 1:1. In general, in NO_x emitted from diesel engines, the proportion of NO is higher than that of NO_2 , and most of the NO_2 is reduced in the fast SCR reaction. If NO is oxidized through DOC and DPF, the ratio of NO_2 should be higher than that of NO , but this was not seen in the experimental results. And, it did not significantly affect the process of observing the adsorption and slip of NH_3 in the SCR, which is the focus of this study. Therefore, assuming that the reduction ratio of NH_3 and NO_x is 1:1, the injection amount of urea water was calculated as in Equation (5.6).

$$\dot{M} = (N_{in} \times \dot{m} / M_{exh}) / (d_{urea} / M_{urea} \times 2 \times 10^6) \quad (5.6)$$

As shown in Table 5.1, the experiment was conducted under 16 different engine operating conditions, respectively, when the engine speed was 1500, 2000, 2500, 3000 rpm, and the exhaust gas temperature was 250, 300, 350, and 400°C. After operating the engine and waiting until the fluctuation of emission gas is reduced, urea-water-solution is injected to measure the change in NO_x and NH_3 according to the change of time when the engine and catalyst conditions are different. The amount of urea-water-solution that NH_3 can react with NO_x and create 100 ppm of NH_3 slip was injected. The reason for injecting the excess amount of urea is to check the total amount of NH_3 adsorbed to the SCR by intentionally making NH_3 slip and to check the trend. So, in order to establish a urea-water-solution injection strategy, we investigated how the amount of NH_3 adsorbed in the SCR appears according to engine conditions and catalyst conditions.

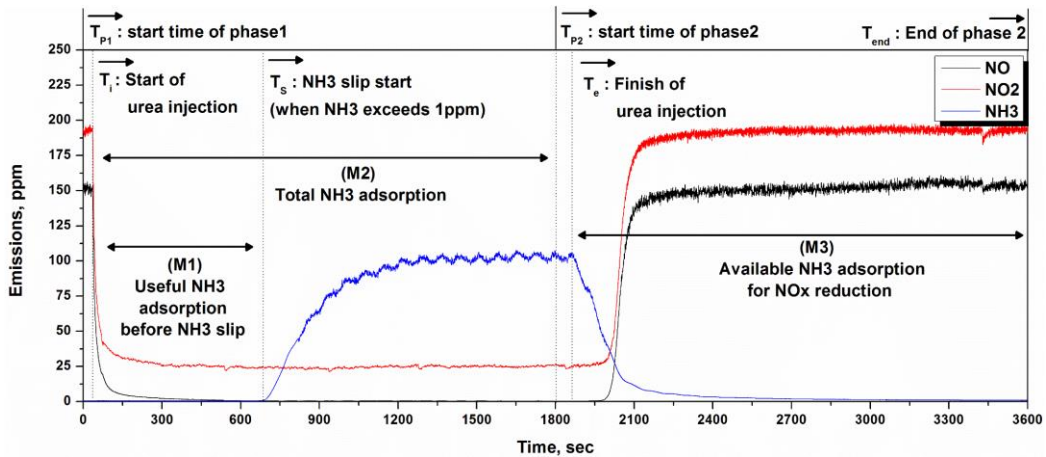


Figure 5.2 NH_3 adsorption and desorption experiment method

Figure 5.2 shows the results of measuring the exhaust gas when the engine speed is 1500 rpm and the exhaust gas temperature is 250°C by the above-mentioned method. In Phase M2, after injecting the urea number with an excess amount of reduction, NO_x tends to decrease and NH_3 slip tends to increase. Phase M3 shows a tendency of NH_3 slip decreasing and a tendency of NO_x increasing again after stopping the urea water injection. Although the NO_x reduction efficiency differs depending on the space velocity and temperature of the exhaust gas depending on the engine conditions, NH_3 slip occurs after a certain period

of time has passed since the NO_x reduction was performed in common. The amount of NH₃ adsorbed in the SCR until NH₃ slip appears through the measured amount of NO_x and NH₃ change (M1), the amount of NH₃ adsorbed after the NH₃ slip (M2), and the amount of adsorption based on the reduced amount of NO_x (M3) were calculated, respectively.

In order to investigate the range that can be controlled so that the NH₃ slip does not appear, the range for measuring the amount of NH₃ adsorbed in the SCR until the NH₃ slip appears is M1. The amount of NH₃ adsorbed per hour before the occurrence of NH₃ slip is considered to be equal to the amount of NH₃ slip during the period in which NH₃ slip appears stably. Therefore, the value obtained by accumulating the amount of NH₃ slip stabilized until the appearance of NH₃ slip for the M1 period can be regarded as the amount of NH₃ adsorbed on the SCR. Further, assuming that the reaction ratio of NH₃ and NO_x is 1:1, NO_x appears in NH₃ slip so that it cannot be reduced. Therefore, it is necessary to consider the NO_x emissions at the time when the NH₃ slip stabilizes and the NO_x emissions during the transient period together. Based on this, the amount of adsorption until NH₃ slip appears can be calculated by the following formula.

$$M_1 = \int_{t=T_i}^{t=T_s} \{A_{mean} - A_t + (N_{mean} - N_t)\} \times \dot{V}_{exh} \times \rho_{NH_3} \quad (5.7)$$

The standard at the moment when NH₃ slip started to appear was set at the moment when NH₃ exceeded 1 ppm. After the appearance of NH₃ slip, a stabilization time of about 1500 to 1800 seconds passed. Adsorption of NH₃ in the SCR continues even when the NH₃ slip occurs, but it can be seen that the amount of NH₃ that can be adsorbed in the SCR is full when the NH₃ slip stabilizes. This is because when NH₃ can no longer be adsorbed on the SCR, the further charged NH₃ is discharged as it is. Therefore, the total amount of NH₃ adsorbed in the SCR can be calculated by the following equation, and the calculation range is set to the time when the NH₃ slip stabilizes.

$$M_2 = \int_{t=T_i}^{t=T_{P2}} \{A_{mean} - A_t + (N_{mean} - N_t)\} \times \dot{V}_{exh} \times \rho_{NH_3} \quad (5.8)$$

As mentioned above, the change in NO_x emissions after the completion of urea water injection was measured in Phase M2. When the urea water injection is completed, NO_x emissions gradually increase even though ammonia is no longer input. It can be assumed that the conventionally adsorbed NH₃ reacted with NO_x if there was no further NH₃ charged into the SCR. Therefore, by integrating the amount of NO_x emitted during this period, it is possible to estimate the amount of NH₃ that was conventionally adsorbed on the SCR. However, since this method calculates the amount of NH₃ adsorbed based on the NO_x reduction reaction, if the existing NH₃ does not react to the reduction of NO_x, it may differ from the result of the amount of NH₃ adsorbed by the M2 calculation method. Therefore, in the case of M3, the following equation can be used to estimate the percentage of how much NH₃ adsorbed in the SCR can be used to reduce NO_x emissions.

$$M_3 = \int_{t=T_e}^{t=T_{end}} \{(N_{2_{mean}} - N_{2_t}) \cdot \rho_{NO_2} / M_{NO_2}\} \cdot \dot{V}_{exh} / 1000 \quad (5.9)$$

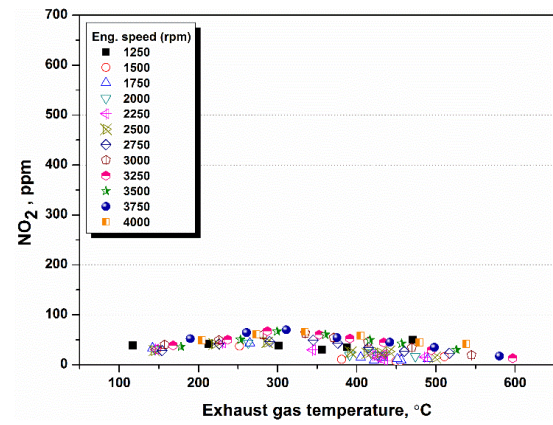
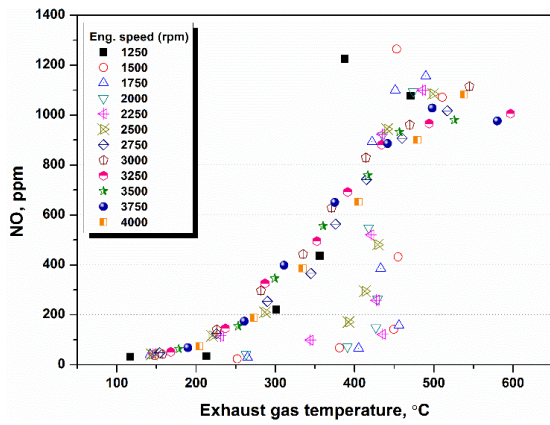
5.3 Results and discussions

5.3.1 NH_3 Adsorption in SCR in different engine condition

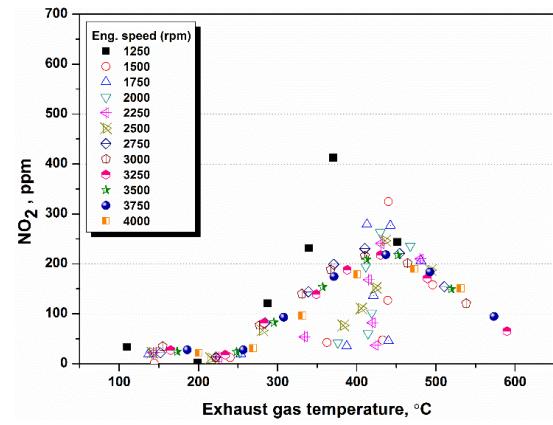
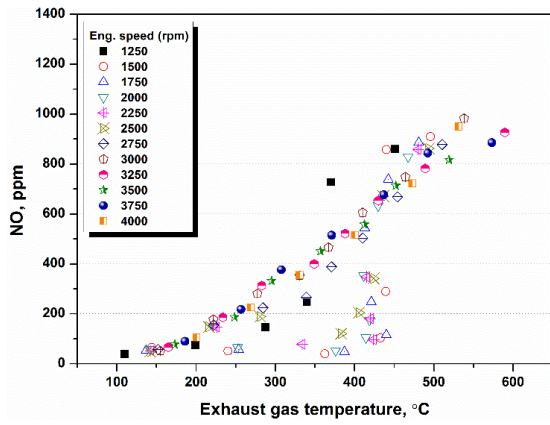
Figure 5.3 shows NO and NO₂ measured immediately after engine combustion and after DOC and DPF. As is generally known, in this experiment, most of the NO_x generated during diesel combustion took the form of NO, and the NO increased in proportion to the combustion temperature. When the exhaust gas temperature was about 400°C, the reason why the NO was measured to be low is due to the activation of the EGR. The EGR was activated when the engine speed and load are medium, and EGR activity was stopped when the exhaust gas temperature is above 450°C to achieve a high engine output. As described above, since the diesel engine used in the experiment satisfies EURO 2, the EGR operating area is relatively narrow compared to the latest engine. After that, looking at the amount of NO and NO₂ through the DOC and DPF, the amount of NO₂ gradually increased due to oxidation of NO as DOC and DPF were activated.

Figure 5.4 shows the results of changes in the amount of NO and NO₂ through the oxidation of NO in the DOC and DPF. When the exhaust gas temperature was below 250 and 200°C, respectively, NO was hardly oxidized due to the inactivation of DOC and DPF, but as the catalyst started to be activated, NO began to be oxidized to NO₂. When the exhaust gas temperature was 450°C, the oxidation rate of NO was highest in DOC, and the oxidation rate of NO was highest at 350°C in DPF. Through this, the main temperature range of this study was 250°C to 400°C which the temperature SCR was activated to the oxidation of NO is maximum.

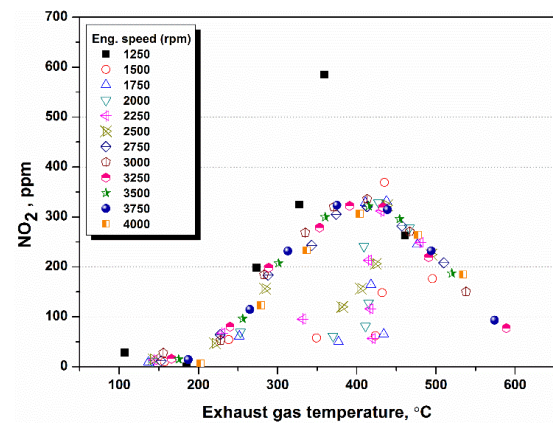
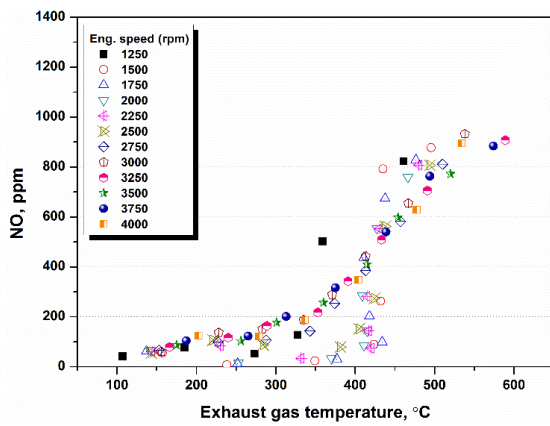
First, the relationship between the reduction efficiency of SCR according to the ratio of NO and NO₂ in NO_x was investigated through the experimental results. Figure 5.5 is a graph showing the SCR reduction efficiency according to the NO and NO₂ ratio. Each color represents the engine rotation speed and the x-axis represents the exhaust gas temperature. The solid square results show the NO_x reduction ratio of SCR, and the empty square shows the ratio of NO and NO₂ inside the exhaust gas entering the SCR. The right y-axis shows the ratio of NO and NO₂, and the left y-axis shows the NO_x reduction rate. The closer the ratio of NO to NO₂ is to 1:1, the closer to 1, and the larger the ratio of NO, the larger the value. The NO_x reduction ratio is closer to 1.0 the closer the NO_x reduction is to 100%. The solid square results show the NO_x reduction ratio of SCR, and the empty square shows the ratio of NO and NO₂ inside the exhaust gas entering the SCR.



(a) Engine out



(b) After DOC



(c) After DPF

Figure 5.3 NO and NO₂ emission characteristics after engine, DOC and DPF

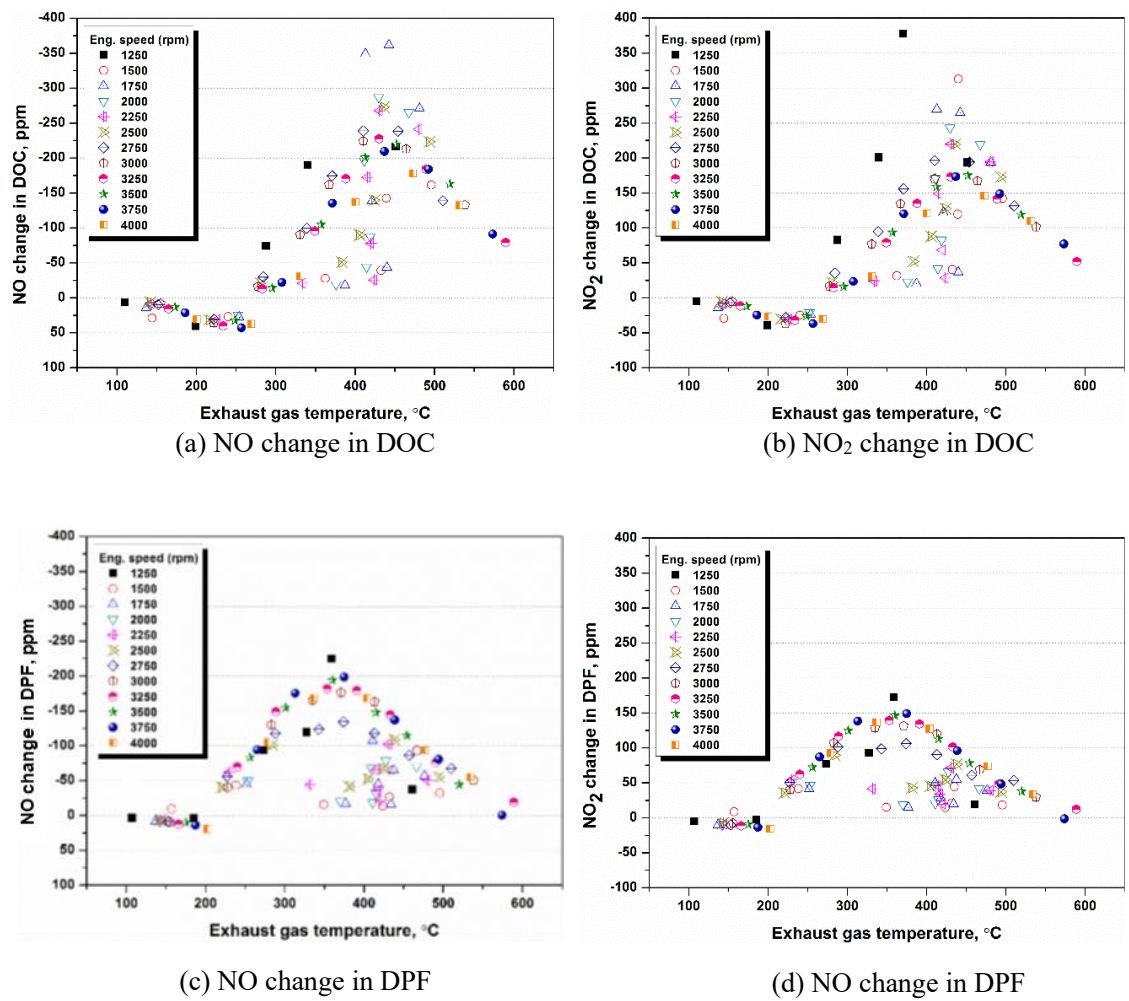


Figure 5.4 NO and NO₂ change in DOC and DPF

As the results, the ratio of NO and NO₂ in the exhaust gas that has passed through the DOC differs depending on the exhaust gas temperature and the engine speed. When the engine cranking speeds were 1500 and 2000 rpm, it was found that NO₂ accounted for a larger proportion than NO in the range of the exhaust gas temperature in the range of 300 to 350 °C, which lowered the NO_x reduction ratio inside the SCR. When the engine speed was 2500 and 3000 rpm, the exhaust gas temperature was slightly 250 °C or less, but at this time the NO ratio was 300 °C or more, which is significantly higher than NO₂, and the NO to NO₂ ratio was almost 1:1. The NO_x reduction ratio inside the SCR was also the lowest when the exhaust gas temperature was about 250 °C, but the ratio of NO and NO₂ was 1:1 and the reduction efficiency was considerably high. As a result, the exhaust gas was partially oxidized to NO₂ via the shear activation DOC and DPF, and NO and NO₂ in a 1:1 ratio entered the SCR. At this time, the highest SCR efficiency was achieved, and excessive conversion to NO₂ reduced the reduction efficiency. Based on the above NO_x reduction ratio, the amount of NH₃ that slip was predicted from the number of injected urea, and the NH₃ adsorbed on the SCR was calculated.

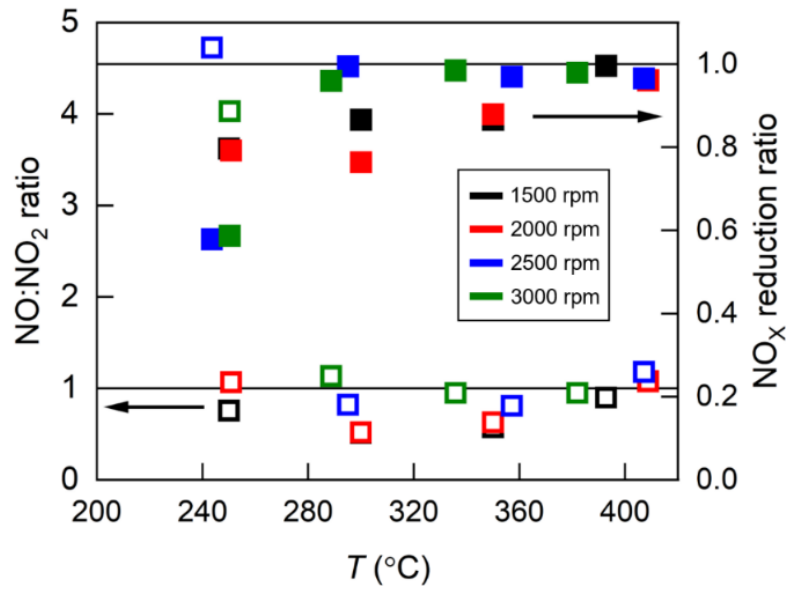


Figure 5.5 Ratio of the NO and NO₂ according to the experiment conditions

Figure 5.6 to 5.8 shows the amount of SCR adsorbed on the SCR in different ways via equation (5.7-5.9). The amount of adsorption at each operating point was displayed, and the average value was displayed on the trend line. As in other previous studies, as the exhaust gas temperature increased, the amount of NH₃ adsorbed on the SCR decreased. Looking at Figure 5.6, which shows the amount of NH₃ adsorbed on the SCR until NH₃ slip occurs, the amount of NH₃ adsorbed is about 1.25 to 0.25 g in the exhaust gas temperature range of 250 to 400°C.

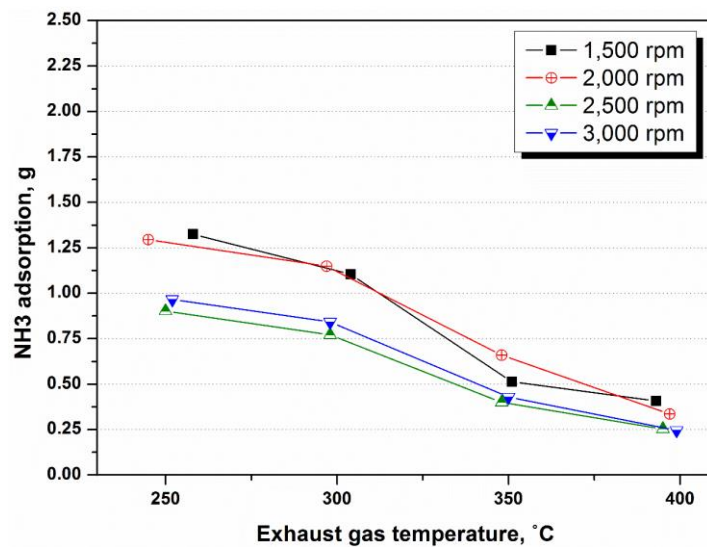


Figure 5.6 NH₃ storage amount calculated in Phase M1 according to experimental conditions

The following Figure 5.7 and 5.8 show the total amount of NH₃ adsorbed on the SCR after the appearance of the NH₃ slip and the total amount of NH₃ adsorbed on the SCR after stopping the urea water injection. From the above results, it can be seen that the total amount of NH₃ adsorbed on the SCR is 1.8 to 0.4 g. Here, the NH₃ adsorption amount substantially utilized for NO_x reduction is the result of reversely calculating the NO_x amount reduced while desorbing NH₃ adsorbed on the SCR. Therefore, the result of M3 can be estimated as the amount of NH₃ adsorbed that can be utilized for actual NO_x reduction. In fact, it was found that the NH₃ adsorption amount calculated by the M2 method was slightly higher than the NH₃ adsorption amount calculated by the M3 method. It can be presumed that this is because NH₃ is adsorbed on the region where the catalyst is not applied and the low temperature portion, particularly on the outer wall of the SCR.

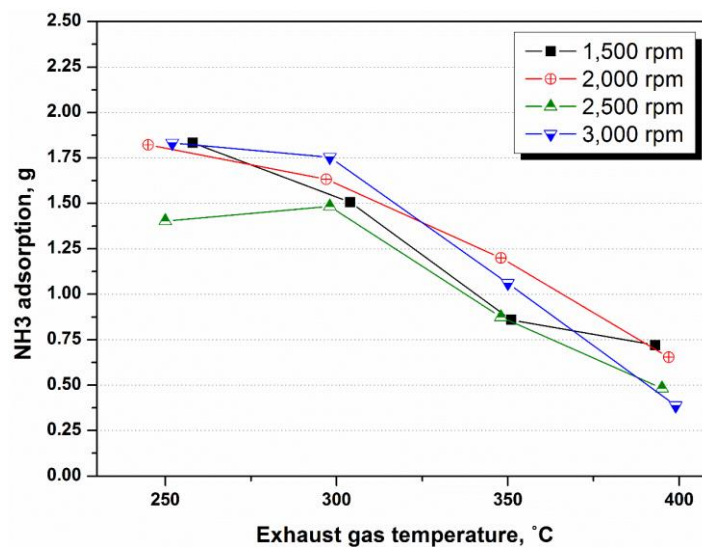


Figure 5.7 NH₃ storage amount calculated in Phase M2 according to experimental conditions

Based on this, the NH₃ adsorption amount actually used for NO_x reduction was regarded as the M3 result value, and the useless NH₃ adsorption amount was calculated by subtracting the M3 result value from the M2 result value. The amount of useless NH₃ adsorption was in the range of 0.1 to 0.2 g over the entire temperature range. Figure 5.9 shows a graph of the proportion of NH₃ adsorption and total adsorption that are not necessary for NO_x reduction. In general, the NH₃ slip reduced the amount of NH₃ adsorbed inside the SCR in the operating region where the exhaust gas temperature was high. In addition, the amount of unnecessary NH₃ adsorption also increased in the operating region where the exhaust gas temperature was higher. As a result, the amount of NH₃ adsorbed unnecessary under the experimental operating conditions was not large from 0.1 to 0.2 g. However, the proportion of total NH₃ adsorbed increased to 60% at the highest temperature. As a result, as the exhaust gas temperature increased, the amount of NH₃ adsorption decreased and the buffer section was reduced, making it difficult to control NH₃ slip.

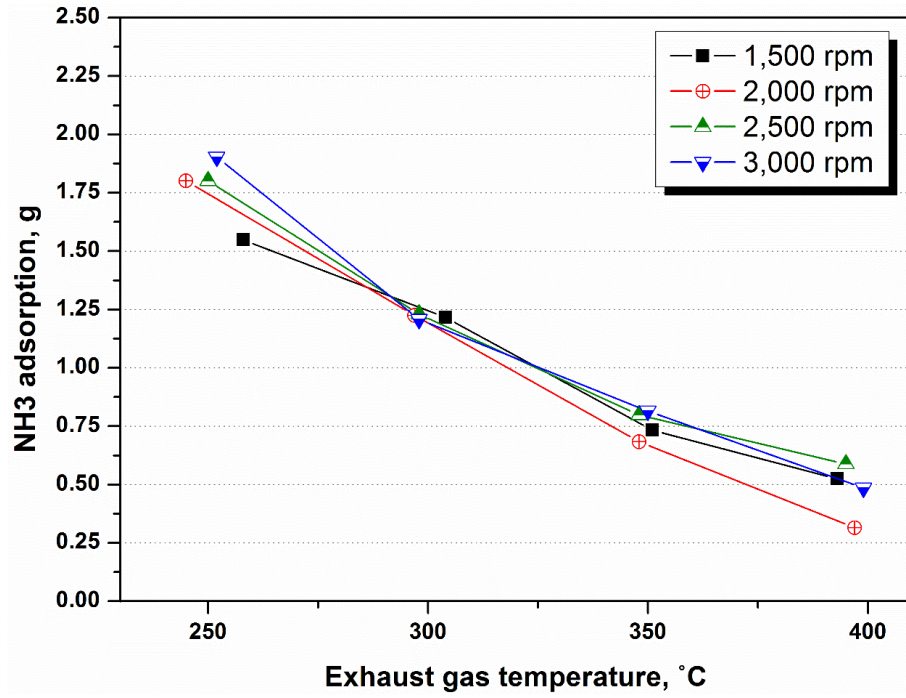


Figure 5.8 NH₃ storage amount calculated in Phase M3 according to experimental conditions

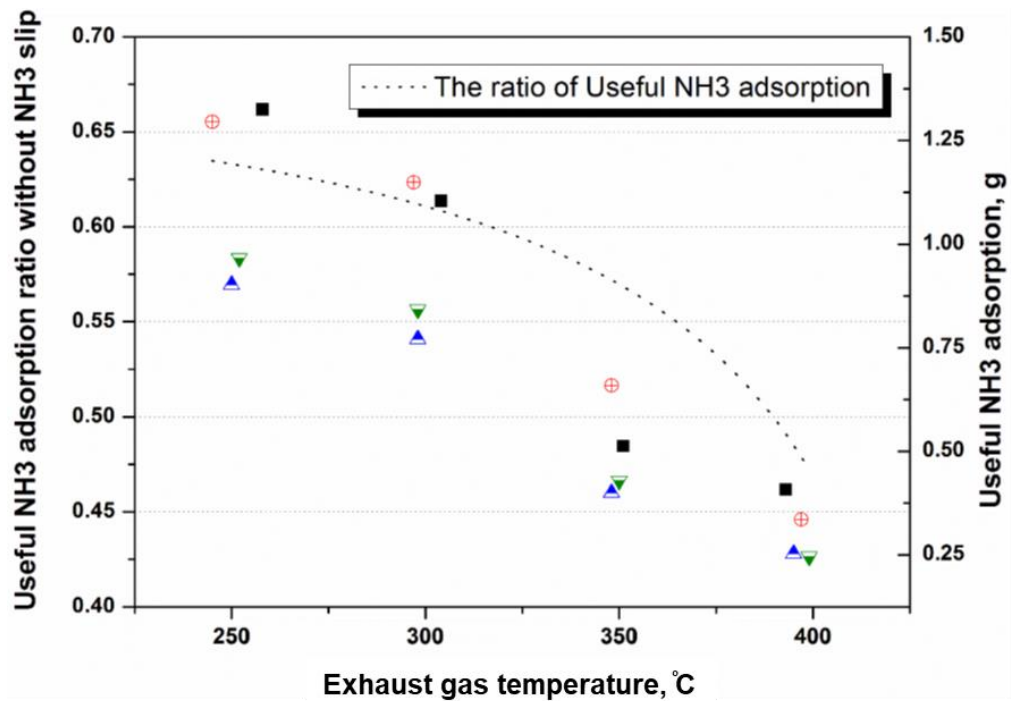


Figure 5.9 Useful NH₃ adsorption amount and ratio used for actual NO_x reduction according to exhaust gas temperature

5.3.2 NH₃ Adsorption and desorption rate in SCR in different engine condition

The amount of NH₃ adsorbed in the SCR varies depending on the engine operating conditions. Therefore, if not only the adsorption amount but also the adsorption rate and the desorption rate are not taken into consideration, a fine urea water injection strategy for controlling the NH₃ slip can be established. Figure 5.10 below shows how the NH₃ adsorption and desorption rates were calculated.

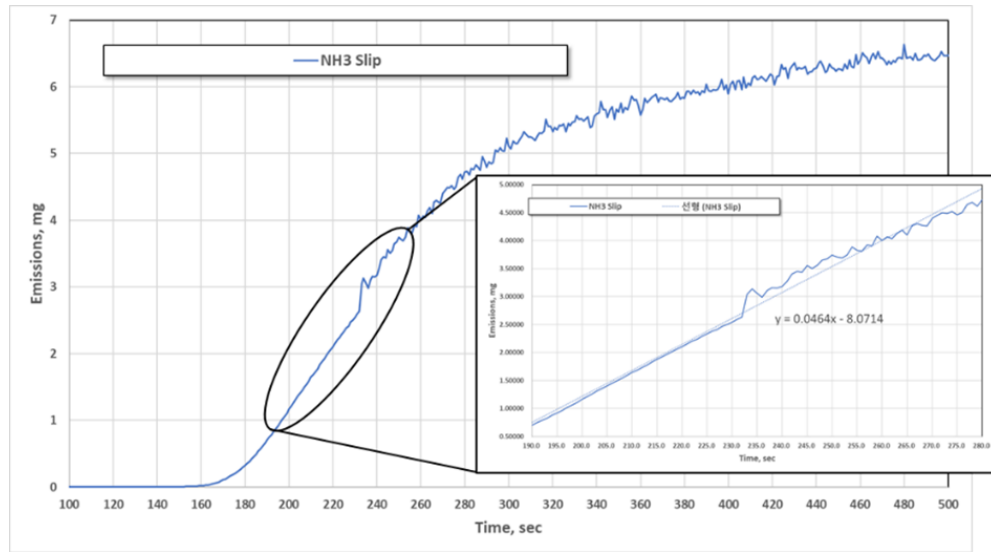


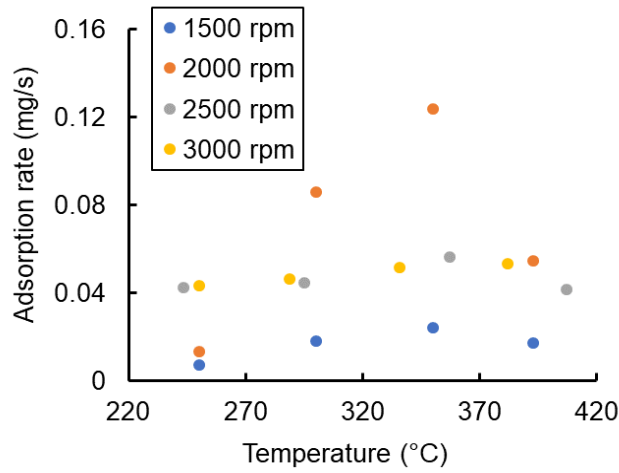
Figure 5.10 Calculation of the NH₃ adsorption rate and desorption rate
(@ 3000 rpm and $T_{\text{exh}} = 300^{\circ}\text{C}$)

The adsorption rate of NH₃ was calculated by the slope in which the NH₃ slip increases from the moment when the NH₃ slip begins to appear after the urea number is injected. The desorption rate of NH₃ was calculated by the slope at which the NH₃ slip decreased after the urea water injection was stopped. Therefore, the adsorption rate and desorption rate of NH₃ were calculated by the following equations inside the SCR.

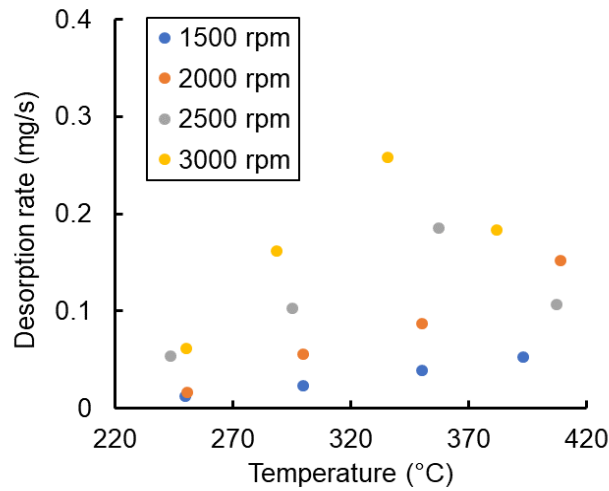
$$\dot{m}_{\text{ammonia,adsorb}} = \partial m_{\text{NH}_3,\text{adsorb}} / \partial t \quad (5.10)$$

$$\dot{m}_{\text{ammonia,desorp}} = \partial m_{\text{NH}_3,\text{desorp}} / \partial t \quad (5.11)$$

Figure 5.11 shows the calculation results of the NH₃ adsorption rate and desorption rate inside the SCR under experimental operating conditions.



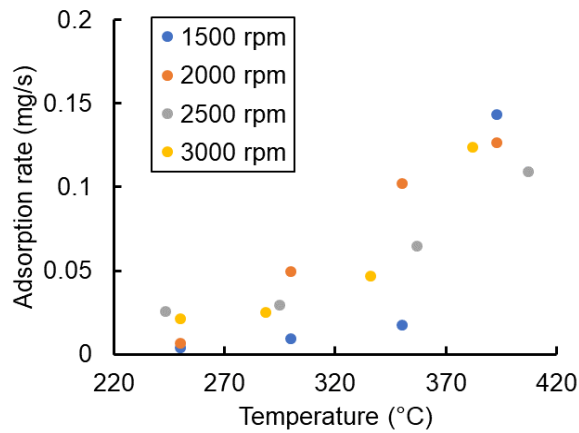
(a)



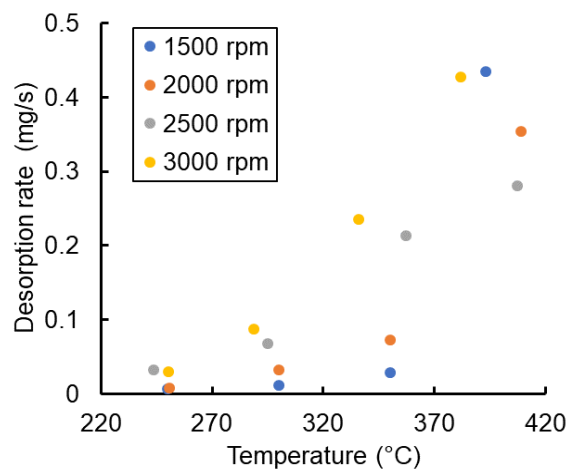
(b)

Figure 5.11 Adsorption (a) and desorption (b) rate of NH_3 in SCR at various conditions

In Figure 5.11, the upper graph shows the NH_3 adsorption rate in the SCR depending on the operating conditions, and the below graph shows the NH_3 desorption rate in the SCR. Looking at the adsorption rate, the adsorption rate appeared relatively fast in the range of engine cranking speed of 2000 rpm and temperature of 300 to 350°C. The proportion of NO_2 in NO_x discharged in this range is high, the NO_x reduction efficiency is relatively low, and a large amount of NH_3 slip occurs, so the adsorption rate of SCR seems to appear rapidly. Therefore, this result alone does not clearly show the relationship between the NH_3 adsorption rate and the desorption rate depending on the operating conditions. The total amount of NH_3 adsorbed in the SCR changes depending on the operating conditions, and the NH_3 slip also changes. Therefore, the results of calculating and comparing the adsorption rate and desorption rate of NH_3 in consideration of the NH_3 storage amount are shown in Figure 5.12.



(a)



(b)

Figure 5.12 Relative values of adsorption (a) and desorption(b) rate of NH_3 in SCR at various conditions

Looking at the results in Figure 5.12, the engine cranking speed does not significantly affect the adsorption and desorption rates of NH_3 in the SCR. However, it turned out to be greatly affected by the exhaust gas temperature. This supports that the total occlusion of NH_3 decreases as the temperature of the exhaust gas rises, so that the rate at which NH_3 is adsorbed inside the SCR and the desorption rate increase. In addition, as the temperature of the exhaust gas rises, it affects the internal temperature distribution of the entire SCR, and it can be expected that the degree of catalytic activation will also be affected. For this reason, in later studies, it is necessary to analyze the NH_3 adsorption rate and desorption rate depending on the temperature distribution inside the SCR and the degree of activation. Based on these results, if a urea water injection strategy is established through experiments on the relationship between the temperature distribution inside the SCR and the operating conditions of the engine, NH_3 slip can be reduced while maximizing the NO_x reduction efficiency.

5.4 Summary

The NH₃ desorption mechanism in SCR is one of the key factors in minimizing NH₃ slip while maximizing NO_x reduction efficiency. In particular, the control strategy is more complicated and difficult in the real-time operation method in which the temperature of the exhaust gas changes in real time. In this study, we considered how to maximize NO_x reduction efficiency and prevent NH₃ slip by analyzing the NH₃ adsorption and desorption mechanism inside the SCR under various engine operating conditions.

The amount of NH₃ adsorbed inside the SCR under the engine operating conditions of this experiment was 0.4 to 1.8 g. The amount of NH₃ adsorbed inside the SCR decreased as the exhaust gas temperature increased. Among the NH₃ adsorbed inside the SCR, the amount of NH₃ that was not utilized to reduce NO_x was about 0.1 to 0.2 g. This ranged from 65 to 94% of the solubility, and similarly, the higher the exhaust gas temperature, the lower the availability. Further, the range of the amount of NH₃ adsorbed until just before the appearance of NH₃ slip is 0.25 to 1.25 g, and the availability calculated based on this is 47 to 63%.

In real-time operation conditions, it is necessary to analyze the adsorption rate and desorption rate in addition to the total adsorption amount of SCR. As a result, the adsorption rate and desorption rate of NH₃ in SCR were not significantly affected by the engine rotation speed. However, it was shown that the adsorption rate and the desorption rate increase as the exhaust gas temperature rises. This is expected to increase the adsorption rate and desorption rate as the total amount of NH₃ adsorbed in the SCR decreases. In addition, although not analyzed in this study, it is necessary to analyze the adsorption mechanism by comparing the temperature distribution inside the SCR with the exhaust gas temperature and the degree of activation. As a result, the decrease in the amount of NH₃ adsorbed inside the SCR at a high exhaust gas temperature suggests that NH₃ slip control is difficult in a transient situation where the exhaust gas is high under actual operating conditions. However, if the urea water injection strategy is established by grasping the temperature of the exhaust gas and the temperature change inside the SCR according to the engine operating conditions, the urea water consumption efficiency can be improved while reducing the NH₃ slip.

References

- [1]. Liang, Y., Ding, X., Dai, J., Zhao, M., Zhong, L., Wang, J., Chen, Y., "Active oxygen-promoted NO catalytic on monolithic Pt-based diesel oxidation catalyst modified with Ce", *Catalysis Today*, Volume 327, 2019, Pages 64-72, ISSN 0920-5861, <https://doi.org/10.1016/j.cattod.2018.06.008>.
- [2]. Salman, A., Enger, B., Auvray, X., Lødeng, R., Menon, M., Waller, D., Rønning, M., "Catalytic oxidation of NO to NO₂ for nitric acid production over a Pt/Al₂O₃ catalyst", *Applied Catalysis A*:

- General, Volume 564, 2018, Pages 142-146, ISSN 0926-860X, <https://doi.org/10.1016/j.apcata.2018.07.019>.
- [3]. Tighe, C., Twigg, M., Hayhurst, A., Dennis, J., “The kinetics of oxidation of Diesel soots by NO₂”, *Combustion and Flame*, Volume 159, Issue 1, 2012, Pages 77-90, ISSN 0010-2180, <https://doi.org/10.1016/j.combustflame.2011.06.009>.
- [4]. Jiao, P., Li, Z., Shen, B., Zhang, W., Kong, X., Jiang, R., “Research of DPF regeneration with NO_x-PM coupled chemical reaction”, *Applied Thermal Engineering*, Volume 110, 2017, Pages 737-745, ISSN 1359-4311, <https://doi.org/10.1016/j.applthermaleng.2016.08.184>.
- [5]. Radojevic, M.m “Reduction of nitrogen oxides in flue gases.”, *Environmental Pollution*, Volume 102, 1998, 685–689.
- [6]. Iwamoto, M., Yahiro, H., Tanda, K. “Catalytic decomposition of nitrogen-monoxide over copper ionexchanged zeolites.” *Studies in Surface Science and Catalysis*, Volume 44, 1989, Pages 219-226, [https://doi.org/10.1016/S0167-2991\(09\)61296-9](https://doi.org/10.1016/S0167-2991(09)61296-9)
- [7]. Shirahama, N., Mochida, I., Korai, Y., Choi, K., Enjoji, T., Shimohara, T., Yasutake, A., “Reaction of NO with urea supported on activated carbons”, *Applied Catalysis B: Environmental*, Volume 57, Issue 4, 26 May 2005, Pages 237-245, <https://doi.org/10.1016/j.apcatb.2004.04.004>
- [8]. Traa, Y., Burger, B., Weitkamp, J., “Zeolite-based materials for the selective catalytic reduction of NO_x with hydrocarbons.”, *Microporous and Mesoporous Materials*, Volume 30, Issue 1, August 1999, Pages 3-41, [https://doi.org/10.1016/S1387-1811\(99\)00030-X](https://doi.org/10.1016/S1387-1811(99)00030-X)
- [9]. Dumesic, J., Topsøe, N., Topsøe, H., Chen, Y., Slabiak, T., “Kinetics of Selective Catalytic Reduction of Nitric Oxide by Ammonia over Vanadia/Titania”, *Journal of Catalysis*, Volume 163, Issue 2, October 1996, Pages 409-417, <https://doi.org/10.1006/jcat.1996.0342>
- [10]. Madia, G., “Measures to enhance the NO_x conversion in urea-SCR systems for automotive applications”, Diss. ETH No 14595
- [11]. Gieshoff, J., Schäfer-Sindlinger, A., Spurk, P., van den Tillaart, J., Garr, G., “Improved SCR Systems for Heavy Duty Applications,” *SAE Technical Paper 2000-01-0189*, 2000, <https://doi.org/10.4271/2000-01-0189>.
- [12]. Liu, Y., Liu, Z., Mnichowicz, B., Harinath, A., Li, H., Bahrami, B., “Chemical deactivation of commercial vanadium SCR catalysts in diesel emission control application”, *Chemical Engineering Journal*, Volume 287, 1 March 2016, Pages 680-690, <https://doi.org/10.1016/j.cej.2015.11.043>
- [13]. Colombo, M., Nova, I., Tronconi, E., “A comparative study of the NH₃-SCR reactions over a Cu-zeolite and a Fe-zeolite catalyst”, *Catalysis Today*, Volume 151, Issues 3–4, 19 June 2010, Pages 223-230, <https://doi.org/10.1016/j.cattod.2010.01.010>

- [14]. Lu L., Wang L., "Model-based optimization of parameters for a diesel engine SCR system" International Journal of Automotive Technology, Volume 14, 2013, pages13–18, <https://doi.org/10.1007/s12239-013-0002-6>
- [15]. Fu, M., Ge, Y., Wang, X., Tan, J., Yu, L., Liang, B., "NO_x emissions from Euro IV busses with SCR systems associated with urban, suburban and freeway driving patterns", Science of The Total Environment, Volumes 452–453, 1 May 2013, Pages 222-226, <https://doi.org/10.1016/j.scitotenv.2013.02.076>
- [16]. Willems, F., Cloudt, R., van den Eijnden, E., van Genderen, M., Verbeek, R., de Jager, B., Boomsma, W., den Heuvel, I., "Is Closed-Loop SCR Control Required to Meet Future Emission Targets?," SAE Technical Paper 2007-01-1574, 2007, <https://doi.org/10.4271/2007-01-1574>.
- [17]. Bonfils, A., Creff, Y., Lepreux, O., Petit, N., "Closed-loop control of a SCR system using a NO_x sensor cross-sensitive to NH₃" IFAC Proceedings Volumes, Volume 45, Issue 15, 2012, Pages 738-743, <https://doi.org/10.3182/20120710-4-SG-2026.00088>
- [18]. Song, Q. and Zhu, G., "Model-based closed-loop control of urea SCR exhaust aftertreatment system for diesel engine", SAE Technical Paper 2002-01-0287, 2002, <https://doi.org/10.4271/2002-01-0287>.
- [19]. Ham, Y., Park, S., "A Study of NH₃ Adsorption/Desorption Characteristics and Model Based Control in the Urea-SCR System", Transactions of the KSAE, Volume 24 Issue 3, 2016, Pages.302-309, <https://doi.org/10.7467/ksae.2016.24.3.302>
- [20]. Schär, C., Onder, C., Geering, H., "Modeling and control of an SCR system", IFAC Proceedings Volumes, Volume 37, Issue 22, April 2004, Pages 355-360 , [https://doi.org/10.1016/S1474-6670\(17\)30369-5](https://doi.org/10.1016/S1474-6670(17)30369-5)
- [21]. Wang, T., Baek, S., Jung M., Yeo, G., "A Study of NH₃ Adsorption/Desorption Characteristics in the Monolithic NH₃-SCR Reactor," Transactions of the KSAE, Volume 14 Issue 3, 2006, Pages.302-309
- [22]. Chen, P., Wang, J., "Nonlinear and adaptive control of NO/NO₂ ratio for improving SCR system performance", Journal of the Franklin Institute, Volume 350, Issue 8, October 2013, Pages 1992-2012, <https://doi.org/10.1016/j.jfranklin.2013.05.020>
- [23]. Mok, Y., Yoon, E., Dors, M., Mizeraczyk, J., "Optimum NO₂/NO_x ratio for efficient Selective Catalytic Reduction", acta physica slovacica, Volume 55, 2005, No.5, pages 467-478.

Chapter 6. Conclusion

6.1 Conclusion

The main purpose of this study has two main objectives. The first is to improve the thermal efficiency of the diesel engine, and the second is to reduce the emission of harmful exhaust gas generated from the diesel engine.

First, it is necessary to reduce the combustion time in order to improve the DCV as a way to increase the thermal efficiency of the diesel engine. To this end, it is necessary to increase the turbulence in the diesel spray flame to improve the premixing of fuel and air. In this study, velocity distribution was analyzed using PIV to investigate the structure and characteristics of diesel spray flames. And, the high temperature region of the diesel spray flame was measured by the OH* chemiluminescence method, and the relationship between the velocity distribution and the high temperature region was analyzed. The results of velocity distribution in diesel spray flame and high temperature region analysis through simultaneous measurement of PIV and OH* chemiluminescence are as follows.

- (1) In the PIV analysis, we can see that the flow of the diesel spray and the surrounding air entrained to the diesel spray flame in the RCEM. Thus, it was found that the PIV result of the RCEM can measure the velocity distribution of diesel spray in a realistic engine situation.
- (2) To investigate the mixing process inside the high-temperature region of the diesel spray flame, a method of calculating the velocity fluctuation intensity was used. When comparing the velocity fluctuation intensity and the intensity of the OH* chemiluminescence, which shows the high-temperature region, it was found that the maximum of the turbulence intensity appears slightly inside of the high-temperature region.
- (3) As the injection pressure increased, the velocity of the diesel spray increased. However, the high-temperature region was not strongly affected by the injection pressure.
- (4) Even if the injection pressure was changed, the maximum velocity fluctuation intensity fell slightly inside of the high-temperature region. As the injection pressure decreased, the maximum value of the velocity fluctuation intensity decreased. It was found that the injection pressure affects the turbulence intensity of the diesel spray flame.

- (5) From this, it was newly found that, after a strong mixture of fuel and air is formed in a region with high turbulence intensity, the region where the stoichiometric is formed is slightly pushed outward due to the diffusion phenomenon as combustion starts.

Next, in order to reduce the harmful exhaust gas emitted from the diesel engine, the overall combustion and exhaust process should be considered. The main harmful exhaust substances emitted from diesel engines are soot and NO_x. In this study, in order to clarify the formation of soot under combustion conditions, we tried to investigate the soot formation according to the jet-jet angle appearing in the multi-hole injector. For this purpose, lift-off length and liquid length were measured, and the flow between jets was analyzed through PIV method.

- (1) The liquid length before ignition was similar irrespective of the jet-jet angle. After ignition, in the case of the larger jet-jet angle, the liquid and lift-off length slowly decrease. However, the liquid and lift-off length of the narrower jet-jet angle rapidly and simultaneously decrease.
- (2) When lowering the injection pressure or decreasing the nozzle diameter, in the case of the narrower jet-jet angle, the lift-off length decreases first, then the liquid length decreases. When the oxygen concentration is lower, the liquid length does not change according to the jet-jet angle. However, the narrower jet-jet angle significantly decreases the lift-off length. The tendencies of the liquid and lift-off length are able to be interpreted by the entrainment of hot-burned gas owing to small-scale recirculation.
- (3) The smaller jet-jet angle, the faster the backward flow velocity, and this phenomenon was larger in the combustion condition. As the ignition of the pre-mixer formed in the downstream of the diesel spray starts, the air in combustion chamber expands and the flow is momentarily directed toward the injector tip. At this time, if the same amount of air is pushed between the sprays, the smaller the gap between the sprays, the faster the pushing speed. Therefore, it can be determined that the backward flow velocity changes significantly compared to the entrainment velocity.
- (4) From this result, it has been newly discovered that, when the jet-jet angle of the injector becomes smaller than a certain level, a strong backflow occurs between the spray jets, and the diesel spray flame near the upstream has a sufficient effect on the liquid part regardless of the ambient atmospheric conditions, thereby shortening the lift-off length. Therefore, it is possible to maximize the thermal efficiency while reducing the formation of a large amount of soot by designing the distance between the number of holes in the injector and the diesel spray accordingly, and designing the flow inside the combustion chamber not to occur centered on the injector.

And also, in order to improve thermal efficiency, exhaust loss and cooling loss should be reduced. However, these methods how to reduce the losses are in a trade-off relationship. Therefore, to achieve both simultaneously, it is necessary to understand the relationship between heat transfer characteristic and flow characteristic near the wall. So, it is necessary to clarify the relationship between the heat flux to the wall and velocity distribution of the diesel spray flame in actual engine situation. For this purpose, the velocity distribution in the diesel spray near the wall was measured by PIV and simultaneously measuring the wall heat flux using a multi-point temperature sensor. So, the results of this research as follows.

- (1) The higher the injection pressure, the faster the diesel spray and the moment it impinges to the wall advances. In addition, the higher the injection pressure, the higher the peak value of the heat flux.
- (2) In the process of decreasing the heat flux, fluctuations were observed, which appeared in line with the timing of fluctuations in the velocity magnitude. From this, it was found that the heat flux at the wall of the combustion chamber is affected by the flow characteristic near the wall.
- (3) When the velocity gradient tensor and the wall heat flux were compared, it was found that the high heat flux part appeared in high velocity gradient tensor region. This suggests that characteristics of the shear flow near the wall can affect the heat flux.
- (4) Through this, it was newly found that the flow in the vertical direction sufficiently affects the heat transfer characteristics at the wall, and overall, the shear flow characteristics near the wall have an important influence on the wall heat transfer characteristics. Therefore, it is important to make the diesel spray flame less shear flow characteristic near the wall in order to prevent the loss of cooling due to heat escaping to the wall of the combustion chamber.

As explained above, in order to reduce harmful exhaust substances generated from diesel engines, it is necessary to treat harmful exhaust substances not only in the combustion process but also in the exhaust process. Urea-SCR is used to reduce NO_x , but if urea input is excessive, the NO_x reduction performance may deteriorate and excessive NH_3 slip may appear. In this study, in order to establish an optimal urea water injection strategy in urea-SCR, NH_3 adsorption and desorption characteristics inside SCR were investigated according to various engine conditions and SCR conditions. The experimental results for this are shown below.

- (1) The amount of NH_3 adsorbed inside the SCR decreased as the exhaust gas temperature increased. In addition, as the exhaust gas temperature increased, the ratio of NH_3 adsorbed in the SCR to the reduction used for NO_x reduction decreased.
- (2) In SCR, the adsorption and desorption rates of NH_3 were not significantly affected by the engine speed, but it was found that the adsorption and desorption rates increased as the exhaust gas temperature increased. This is expected to increase the adsorption rate and desorption rate as the total amount of NH_3 adsorbed to the SCR decreases.
- (3) From this result, it is necessary to analyze the adsorption mechanism by comparing the temperature distribution inside the SCR with the exhaust gas temperature and the degree of activation. So, the urea water injection strategy is established by grasping the temperature of the exhaust gas and the temperature change inside the SCR according to the engine operating conditions, the urea water consumption efficiency can be improved while reducing the NH_3 slip.

6.2 Recommendations for future researches

In summary, several methods are presented for the thermal efficiency of diesel engines and reduction of harmful emissions. Looking at the structure and velocity distribution results of diesel spray flame, the region with high velocity fluctuation intensity and the high temperature region did not match. As the injection pressure increased, the fuel injection duration was shortened, which had the effect of reducing the combustion duration. However, the relationship between the high temperature region and the strong turbulence region did not change. Therefore, it is necessary to study the diesel spray flame structure and velocity distribution according to the conditions of the injector and the ambient conditions of the combustion chamber. In addition, if we can make a modelling for the diesel spray and flame formation according to jet-jet angle, it will be helpful in conducting the research in various types and conditions of multi-hole injectors in the future. For the above-mentioned purposes, the following studies are recommended in the future.

1. Previously, the relationship between the high-temperature region and the turbulent flow region was investigated through the structure and velocity distribution of the diesel spray flame by the injection pressure. To further understand this, we also need to investigate the influence of the diameter of the injector nozzle, the ambient pressure in the combustion chamber, and the oxygen concentration. In addition, it is necessary to investigate the mixing of the fuel and air according to the injection conditions and combustion chamber conditions through the relationship between

velocity distribution and local equivalent ratio in diesel spray flames. However, as shown in the experimental results, it was not easy to measure a more specific velocity distribution in the mixing-controlled combustion duration due to the soot cloud. If the measurement problem can be solved, it will be possible to measure the velocity of the diesel spray flame inside the high temperature region more clearly.

2. In order to improve the thermal efficiency of diesel engines, it is necessary not only to reduce DCV but also to reduce the cooling losses. For this, it needs to understand the mechanism between the flow of diesel spray near the wall and the heat transfer at the wall of the combustion chamber. The PIV method from this study can be used to analyze the diesel spray flow at the walls of the combustion chamber. And, measuring the heat transfer at the walls of the combustion chamber will help to investigate the correlation between the two. In addition, it will be possible to analyze the heat transfer characteristics of the combustion chamber wall according to the change in the flow characteristics of the diesel spray according to the injection conditions.
3. In a multi-hole injector, the flow and temperature between the jet-jet spray influence the properties of each diesel spray flame. In this experiment, the characteristics that can affect adjacent sprays in the upstream part of the flame, such as lift-off length and liquid-length, were mainly analyzed. In an actual engine situation, not only the upstream part of the flame but also the soot formation in the downstream part of the flame due to the interference with the adjacent spray flame after impinging to the combustion chamber wall is also an important factor. Therefore, it is necessary to study the soot formation characteristics in the flame downstream according to the injection conditions and the jet-jet angle.

List of Publications

Chapter 2

Jo, H., Kawai, Y., Horibe, N., Hayashi, Kawanabe, H., Ishiyama, T., "A Study on Diesel Spray Flame by Time-Resolved PIV with Chemiluminescence of OH*", SAE Int. J. Adv. & Curr. Prac. in Mobility 4(2):592-601, 2022, <https://doi.org/10.4271/2021-01-1167>.

Chapter 3

Jo, H., Ishikawa, T., Horibe, N., Hayashi, Kawanabe, H., Ishiyama, T., "Effect of Jet-Jet Angle on Combustion Process of Diesel Spray in an RCEM," SAE Int. J. Adv. & Curr. Prac. in Mobility 3(1):276-286, 2021, <https://doi.org/10.4271/2020-01-2058>.

Chapter 4

Jo, H., Kawai, Y., Horibe, N., Kawanabe, H., Ishiyama, T., Daijiro, I., Mihara, Y., "Analysis of the Relationship between Near-wall Velocity Distribution and Wall Heat Flux by a Diesel Spray Flame Impingement", The 10th International Conference on Modeling and Diagnostics for Advanced Engine Systems (COMODIA 2022), July 5-8, 2022, Sapporo, Japan

Chapter 5

Ko, A., Woo, Y., Jang, J., Jung, Y., Pyo, Y., **Jo, H.**, Lim, O., Lee, Y., "Availability of NH₃ adsorption in vanadium-based SCR for reducing NO_x emission and NH₃ slip", Journal of Industrial and Engineering Chemistry, Volume 78, 2019, Pages 433-439, ISSN 1226-086X, <https://doi.org/10.1016/j.jiec.2019.05.024>.

Ko, A., Woo, Y., Jang, J., Jung, Y., Pyo, Y., **Jo, H.**, Lim, O., Lee, Y., "Complementary effects between NO oxidation of DPF and NO₂ decomposition of SCR in light-duty diesel engine", Journal of Industrial and Engineering Chemistry, Volume 80, 2019, Pages 160-170, ISSN 1226-086X, <https://doi.org/10.1016/j.jiec.2019.07.045>.

Acknowledgement

First of all, I thank God for watching over me always.

I am deeply grateful to my supervisor, Prof. Kawanabe Hiroshi, for my Doctoral course studies at Kyoto University. It was an honor for me to enter the department of Energy Sciences in Kyoto University from October 2019 to conduct interesting research on internal combustion engine. Through the guidance of the professor, I was able to learn what I was lacking in my research and how to develop. Through the professor's passion and dedication to research, I was able to develop further and it was a great help in completing this thesis. Thank you very much.

In addition, I would like to express my deepest gratitude to Prof. Hayashi Jun. Your great insight into your research knowledge helped me a lot of studying my research and writing my thesis. After I finish my doctoral course, I will live my life as an important part of my research career.

Prof. Naoto Horibe is a professor who commented on all the experiments and analysis during my Doctoral course program, and told me what I lack, what I need, and what I can improve on. I learned a lot as a researcher, and realized how to become a good researcher. I would like to express my sincere gratitude to you for allowing me to finish my Doctoral course program thanks to you.

I would also like to thank Mr. Ishikawa Taichi, Mr. Kawai Yuta, Mr. Yasui Yusuke, Mr. Nishijima Jun and other Combustion and Power Engineering Lab students for their help in my Doctoral course research.

I am also deeply grateful to assistant researcher Mr. Hurokawa Tadayoshi for helping me configure the experimental setup and run the experiment with me. Thank you for letting me know a lot even though I'm not good at Japanese. Also, I would like to express my deepest gratitude to officer Mrs. Takamura Wakao and Mrs. Okuyama Miki for their support of my Doctoral course.

Finally, I would like to express my deepest gratitude to my family for worrying about studying abroad during COVID-19 and always praying for me. Even in a mentally difficult situation, the cheer and support from my family was a great strength to me and the driving force that allowed me to move forward. Also, I would like to thank the Rotary Yoneyama Scholarship Association for providing financial support and providing various experiences as I study in Japan.

Jo Hyun